ABSTRACT

Title of dissertation: ADVANCES IN SEQUENTIAL DATA ASSIMILATION AND NUMERICAL WEATHER FORECASTING: AN ENSEMBLE TRANSFORM KALMAN-BUCY FILTER, A STUDY ON CLUSTERING IN DETERMINISTIC ENSEMBLE SQUARE ROOT FILTERS, AND A TEST OF A NEW TIME STEPPING SCHEME IN AN ATMOSPHERIC MODEL

Javier Amezcua, Doctor of Philosophy, 2012

Dissertation directed by: Professor Eugenia Kalnay
&
Professor Kayo Ide

Department of Atmospheric and Oceanic Science

This dissertation deals with aspects of sequential data assimilation (in particular ensemble Kalman filtering) and numerical weather forecasting.

In the first part, the recently formulated Ensemble Kalman-Bucy (EnKBF) filter is revisited. It is shown that the previously used numerical integration scheme fails when the magnitude of the background error covariance grows beyond that of the observational error covariance in the forecast window. Therefore, we present a suitable integration scheme that handles the stiffening of the differential equations involved and doesn't represent further computational expense. Moreover, a transform-based alternative to the EnKBF is developed: under this scheme, the operations are performed in the ensemble

space instead of in the state space. Advantages of this formulation are explained. For the first time, the EnKBF is implemented in an atmospheric model.

The second part of this work deals with ensemble clustering, a phenomenon that arises when performing data assimilation using of deterministic ensemble square root filters in highly nonlinear forecast models. Namely, an *M*-member ensemble detaches into an outlier and a cluster of *M-1* members. Previous works may suggest that this issue represents a failure of EnSRFs; this work dispels that notion. It is shown that ensemble clustering can be reverted also due to nonlinear processes, in particular the alternation between nonlinear expansion and compression of the ensemble for different regions of the attractor. Some EnSRFs that use random rotations have been developed to overcome this issue; these formulations are analyzed and their advantages and disadvantages with respect to common EnSRFs are discussed.

The third and last part contains the implementation of the Robert-Asselin-Williams (RAW) filter in an atmospheric model. The RAW filter is an improvement to the widely popular Robert-Asselin filter that successfully suppresses spurious computational waves while avoiding any distortion in the mean value of the function. Using statistical significance tests both at the local and field level, it is shown that the climatology of the SPEEDY model is not modified by the changed time stepping scheme; hence, no retuning of the parameterizations is required. It is found the accuracy of the medium-term forecasts is increased by using the RAW filter.

ADVANCES IN SEQUENTIAL DATA ASSIMILIATION AND NUMERICAL WEATHER FORECASTING: AN ENSEMBLE TRANSFORM KALMAN-BUCY FILTER, A STUDY ON CLUSTERING IN DETERMINISTIC ENSEMBLE SQUARE ROOT FILTERS, AND A TEST OF A NEW TIME STEPPING SCHEME IN AN ATMOSPHERIC MODEL

By

Javier Amezcua

Dissertation submitted to the Faculty of the Graduate School of the
University of Maryland, College Park in partial fulfillment
of the requirements for the degree of
Doctor of Philosophy.
2012

Advisory Committee:

Professor Eugenia Kalnay
Professor Kayo Ide
Professor Takemasa Miyoshi
Professor Sebastian Reich
Professor Brian Hunt

Copyright by

Javier Amezcua

© 2012

ACKNOWLEDGMENTS

Many people have supported and encouraged me throughout these years; I am indebted to them. I start the list by thanking my family for their love, patience and encouragement towards me, as well as for their constant example of hard work and dedication. Also, I thank those few people in the world whom I call 'friends' for their companionship (sometimes remote) and fondness.

I am grateful to my academic advisors Dr. Eugenia Kalnay and Dr. Kayo Ide. I thank Eugenia for her ideas, mentoring and optimism. I also thank her for introducing me to so many wonderful people that have become my collaborators. I sincerely thank her for her constant words of appreciation and enthusiasm, and for financially supporting my research and my travels. I am deeply indebted to Kayo for transmitting me some of her knowledge in those rewarding conversations we held in her office, and I am thankful for her patience and mentoring. I also thank the members of the Chaos-Weather research group for providing a stimulating environment. I thank Dr. Sebastian Reich for allowing me to work with his most genial ideas about the ensemble Kalman-Bucy filter. Dr. Craig Bishop is acknowledged for his ideas on the non-symmetric ETKF. I am grateful to Dr. Paul Williams for letting me 'play' with his RAW filter. I kindly acknowledge all the members of my dissertation committee for reading my work and making suggestions to improve it.

Finally, I am grateful to the AOSC department and in particular Dr. Robert Hudson for allowing me to entertain myself with my other passion: teaching. The experience I gained

assisting in undergraduate courses and teaching a middle school summer program was rewarding and invaluable.

In a life without inherent meaning, I have found beauty in knowing, learning and understanding.

Javier Amezcua Espinosa

College Park, May 2012

TABLE OF CONTENTS

LIST OF TABLES vi

LIST OF FIGURES vii

1. Introduction and objectives 1

1.1. Introduction 1

1.2. Objectives 8

2. Background 10

2.1. Concepts of sequential data assimilation 10

2.1.1. Kalman Filter 10

2.1.2. Kalman-Bucy filter 12

2.1.3. Ensemble Kalman Filters 15

2.1.4. Local Ensemble Transform Kalman Filter and a non-symmetric solution 17

2.1.5. Ensemble Kalman-Bucy Filters 20

2.2. Dynamical models used in this work 23

2.2.1. The Lorenz 1963 model 23

2.2.2. The 40-variable Lorenz 1996 model 24

2.2.3. A medium complexity AGCM: SPEEDY 26

3. Analysis on the Ensemble Kalman-Bucy Filter 29

3.1 Numerical integration in the EnKBF 31

3.2. Transform-based alternatives for the EnKBF 40

3.3. Localization in the ETKBFs 45

3.4. Experiments 50

3.4.1. Experiments with the 3-variable Lorenz 1963 model 50

3.4.2. Experiments with the 40-variable Lorenz 1996 model 58

3.4.3. Experiments with the SPEEDY model 65

4. Ensemble clustering in ensemble square root filters 73

4.1 Generating mean-preserving non-symmetric solutions of ETKF 76

4.2. Metric for ensemble clustering and experimental setup 81

4.3. Ensemble clustering in a simple nonlinear model..... 82

4.3 Localization aspects of the MPNS-LETKF 90

4.4. Experiments 93

4.3.1 Experiments with the Lorenz 1963 model 93

4.3.2. Experiments with SPEEDY 99

5. The effects of the RAW filter on the climatology and forecast skill of the SPEEDY model .. 105

5.1. The Robert-Asselin-Williams (RAW) filter 106

5.2. Effects of the RAW filter on the climatology of the SPEEDY model 112

5.2.1. Local significance 113

5.2.2. Field significance 116

5.3. Effects of the RAW filter on the skill of short term and medium term forecasts 122

6. Summary and conclusions 129

Appendix A. Derivation of the Kalman-Bucy filter and the equivalence of the KBF and KF equations in pseudo-time 137

Appendix B. Abbreviations and symbols 145

References..... 147

LIST OF TABLES

Table 1. Lowest RMSE values in the Lorenz 1963 model with frequent and infrequent observations using three filters. The optimal inflation value is indicated in parenthesis..... 57

Table 2. Results of the experiments with the L96 model. Three assimilation methods (columns) and two ensemble sizes (rows) are used. In each case, a sample of 10^6 assimilation cycle was used to find the average analysis RMSE, average ensemble spread and average inflation parameter (averaged also over the 40 gridpoints). The numbers in parenthesis correspond to the standard deviations of the reported parameters. 63

Table 3. For each one of the variables, this table presents the number of grid points (out of 96x48) that resulted locally significant $\alpha_{local} = 0.05$ after applying the t-test. The variables that result field significant with a value of $\alpha_{field} = 0.05$ are presented bolded if they are field significant considering only finite sample size [and independence], and they are also presented in italics (besides the bolding) if they are field significant considering both finite sample size and spatial correlation. 118

Table 4. Minimum number of tests (out of 96x48) to be passed with a local significance $\alpha_{local} = 0.05$ to achieve a field significance $\alpha_{field} = 0.05$ 121

LIST OF FIGURES

Figure 1. Time evolution of the 500-hPa geopotential height in College Park, MD, forecasted with the SPEEDY model (section 2.2.3).Two forecasts are started from infinitesimally close initial conditions, after ~10 days they start to differ considerably and after 2 weeks any resemblance is lost, exemplifying the chaotic behavior of the atmosphere. 2

Figure 2. Schematic depicting a general data assimilation process. Information coming from forecasts (blue dashed line) is blended with that coming from observations (red dots) to get a better estimate of the truth, the analysis (purple squares). The analysis is used as the best initial condition for the next forecast. 3

Figure 3. Schematic representation pseudo-time in the EnKBF, it is spanned at each assimilation instant. 14

Figure 4. Lorenz 1963 model. The top panel depicts the time evolution of the three variables in the model. The bottom panel shows the shape of the attractor in phase space. 24

Figure 5. Lorenz 1996 model: time evolution of selected variables (left) and all the 40 variables using a Hovmoller diagram (right). 26

Figure 6. Observational density used for the experiments with the SPEEDY model. The spatial distribution of the observations resembles a realistic radiosonde network (Miyoshi, 2005). Two positions are circled, one over the Labrador Peninsula and other over the Southern Pacific Ocean; these locations will be used to display results in subsequent sections. 28

Figure 7. Schematic depicting the jump from background mean to analysis mean in sequential data assimilation. The bold dashed line depict the background/analysis mean, the red dots are observations, and the pink lines represent the jump from background mean to analysis mean when the assimilation is performed. 29

Figure 8. In order to create a smoother transition from background to analysis, the impact of the observation (red dot) can be extended into a finite time interval, represented by the base of the red triangles. The height of the triangle represents the relative importance given to the observation in this interval. This can be achieved in the EKBF by a mollification of the Dirac delta function. .. 30

Figure 9. Analytical solution of the Bucy covariance equation in pseudo-time for a scalar case with the variable observed directly. Different lines correspond to different values ratio of background variance over observational error variance (see the legend). Two colors distinguish lines at different sides of the threshold of $\beta = 1$. The ODE stiffens as this ratio becomes larger. 34

Figure 10. Empirical cumulative distribution function of $\beta = \left|\mathbf{Y}^{b^T}\mathbf{R}^{-1}\mathbf{Y}^b\right| \Big/ (M-1)$ for short (orange line) and long (purple line) assimilation windows using the Lorenz 1963 model. The

value of this ratio for infrequent observations is in general an order of magnitude larger than for frequent observations. 36

Figure 11. Analytical solution of the Kalman-Bucy equation for covariance in pseudo-time. For large values of β more resolution is needed at the beginning of the window (shaded region). 40

Figure 12. Schematic of R-localization (courtesy of Dr. Greybush). 46

Figure 13. Example of the evolution and assimilation of $x^{(2)}$ in the infrequent observations case with LETKF. The true run, the observations and the analysis ensemble are shown. 50

Figure 14. Analysis RMSE for LETKF and the two Bucy-based formulations in the case of frequent observations in the Lorenz 1963 model. The integration uses the EF method. 53

Figure 15. Analysis RMSE for LETKF and ETKBF and DETKBF with 5 steps in pseudo-time in the frequent observations case. The DSI integration method is used for the Bucy-type formulations. 54

Figure 16. Analysis RMSE for LETKF and BGR09 in the case of infrequent observations in the Lorenz 1963 model. The integration uses the EF method. 55

Figure 17. Analysis RMSE values (averaged over 10^6 assimilation cycles) for ETKF, ETKBF and DETKBF in L63 in the the infrequent observations case is shown. The Bucy-type formulations were integrated using the (DSI) method with 8 non-uniform steps. 56

Figure 18. Filter performance for B-localized BR10 (left), R-localized DETKBF (center) and LETKF (right) in the L96; for the Bucy-type formulations the DSI integration scheme with 4 uniform steps is used. The effects of multiplicative inflation and localization radius are shown; each tile represents an average over 10^5 analysis cyles. The top row show the analysis RMSE, the uncolored tiles denote RMSE values larger than the observational error, but all the RMSE values were finite and < 4.6. The bottom row shows the ratio of the average ensemble spread divided by the analysis RMSE; ideally this ratio should be close to 1. 60

Figure 19. Analysis RMSE for the first 150 assimilation cycles of an experiment using L96 and R-localized DETKBF. The effect of the two integration schemes (Euler Forward and Diagonal Semi-Implicit) is shown for different initial ensembles. As the initial ensemble is more inaccurate (from left to right), EF takes longer to initialize the filter while DSI does not present problems. 61

Figure 20. Local value of (multiplicative covariance inflation) for each one of the 40 gridpoints, averaged over 10^6 analysis cycles. Three filters and two ensemble sizes are presented. 64

Figure 21. Schematic of set up for single-observation experiments. After the spin-up period, all observations are assimilated for three days. These allows for the differences caused by the observational density in different regions of the world to appear. 66

Figure 22. Impact of a single-observation experiment. The observation is located in the well-observed Labrador Peninusula. The difference between analysis mean and background mean is the same using the three methods; the variable illustrated is zonal wind at 510 hPa. 67

Figure 23. Time evolution of the background and analysis mean (left panel) and ensemble spread (right panel) for LETKF, ETKBF and DETKBF. The depicted variable is zonal wind at 510hPa in a location over the Labrador peninsula. 68

Figure 24. Impact of two single-observation experiments. The observation is located in the poorly-observed Southern Pacific, hence in an area prone to stiffness. We show the ratio of the analysis spread to background spread for the meridional wind at 950 hPa. 69

Figure 25. Analysis RMSE values computed globally for each variable at different pressure levels for the three filters. 70

Figure 26. Analysis RMSE for zonal (left) and meridional (right) wind computed for different regions (rows) at different pressure levels (columns) for the three filters. 71

Figure 27. Analysis RMSE for temperature (left) and geopotential height (right) computed for different regions (rows) at different pressure levels (columns) for the three filters. 71

Figure 28. Analysis RMSE for relative humidity computed for different regions (rows) at different pressure levels (columns) for the three filters. 72

Figure 29. Examples of ensemble clustering in (a) the Ikeda model (Lawson and Hansen, 2004) and the L63 model (Anderson, 2010). 75

Figure 30. Data assimilation experiment with the model $x_{t+1} = x_t + 0.05\left(x_t + b\left|x_t\right|x_t\right)$, observations every 2 model steps, and $M = 10$. For panels (a)-(c) $b = 0.2$. LETKF (a) presents ensemble clustering soon after 5 time units while the MPNS-ETKF (b) doesn't. In (c) we quantify the clustering degree for both filters. 84

Figure 31. Data assimilation experiment with the model $x_{t+1} = x_t + 0.05\left(x_t + b\left|x_t\right|x_t\right)$. The clustering degree is measured for LETKF different ensemble sizes and values of *b*. 85

Figure 32. Update mechanisms for LETKF and MPNS-ETKF for the individual ensemble members, with the red dots indicating the observation value. LETKF preserves the structure from the background ensemble into the analysis ensemble. The MPNS-ETKF effectively scrambles the ensemble every time an assimilation occurs. The model is $x_{t+1} = x_t + 0.05\left(x_t + b\left|x_t\right|x_t\right)$, $b = 0.2$, observations every 5 model steps, and $M = 10$ 86

Figure 33. Clustering degree (left axis) and position of the truth within the ensemble (right axis) for LETKF and MPNS-ETKF for the individual ensemble members. 87

Figure 34. Data assimilation with the simple univariate model. When using LETKF (left) one can follow individual trajectories for the ensemble members. This ability is lost when using MPNS_ETKF (right) since the ensemble is 'rebooted' every time assimilation is performed. 87

Figure 35. Assimilation experiments with the model $x_{t+1} = x_t + 0.05\left(x_t + b\left|x_t\right|x_t\right)$. We allow the nonlinear coefficient b_t to vary as a piece-wise function of time (green line, right vertical axes).

The clustering degree is represented by the black line and left vertical axes. The time intervals in which b_t is fixed are different for each panels. Panel (e) shows the ensemble evolution for the time interval $t \in [600,850]$ of case (b); the reattachment of the outlier occurs in a natural way. 89

Figure 36. Schematic depicting the effect of R-localization in the LETKF. Each grid-point has its own matrix of weights; a smooth transition among these weights is indispensable to ensure stability.....91

Figure 37. Correlation between the analysis weights of gridpoint 12 with respect to the weights in neighboring gridpoints for the L96 model. For LETKF (black line, left vertical axis) the correlation values are high and they present a smooth transition. For MPNS-ETKF (gray line, right vertical axis), the transition is not smooth and the correlation values are low. MPNS-ETKF cannot be directly applied with R-localization. 92

Figure 38. Time evolution of the ensemble clustering degree for LETKF (black solid line) and MPNS-ETKF (green dashed line) from an assimilation experiment with the L63 model. Three ensemble sizes (columns) are used in a linear regime (top row) and a nonlinear regime (bottom row).....94

Figure 39. Experiments with L63, observations every 24 model steps and *M=3*. The evolution of the clustering degree is shown in the top. Snapshots of the phase space are presented for three time intervals with contrasting *CD* values, the one in the middle shows clustering occurring. 95

Figure 40. Bred vector growth rate in the Lorenz 1963 attractor. In the left panel, a picture of the attractor in phase space is shown. In the right three panels, the time evolution of each variable is shown colored by growth rate (reproduced from Evans *et al*, 2004).....96

Figure 41. Boxplots for *CD* (top row) and analysis RMSE (bottom row) for both LETKF and MPNS-ETKF in the linear (left column) and nonlinear (right columns) regimes. Results are shown for three different ensemble sizes.....98

Figure 42. Rank histograms for the verification of the truth with respect to the analysis ensemble in the Lorenz 1963 model. Two different ensemble sizes are used in the linear and nonlinear regimes.....99

Figure 43. Latitude weighted analysis RMSE (left) and analysis skewness (right) for all variables computed globally. The bars represent one standard deviation of the metric around its mean. ET denotes LETKF and NS denotes MPNS-ETKF.....100

Figure 44. Latitude weighted analysis RMSE (left) and analysis skewness (right) for zonal wind computed per region (rows) for 3 vertical levels (columns) in the SPEEDY model. The bars represent one standard deviation of the metric around its mean. ET denotes LETKF and NS denotes MPNS-ETKF. 101

Figure 45. Latitude weighted analysis RMSE (left) and analysis skewness (right) for meridional wind computed per region (rows) for 3 vertical levels (columns) in the SPEEDY model. The bars

represent one standard deviation of the metric around its mean. ET denotes LETKF and NS denotes MPNS-ETKF. 101

Figure 46. Latitude weighted analysis RMSE (left) and analysis skewness (right) for geopotential height computed per region (rows) for 3 vertical levels (columns) in the SPEEDY model. The bars represent one standard deviation of the metric around its mean. ET denotes LETKF and NS denotes MPNS-ETKF. 102

Figure 47. Latitude weighted analysis RMSE (left) and analysis skewness (right) for relative hummidity computed per region (rows) for 3 vertical levels (columns) in the SPEEDY model. The bars represent one standard deviation of the metric around its mean. ET denotes LETKF and NS denotes MPNS-ETKF. 103

Figure 48. Latitude weighted analysis RMSE (left) and analysis skewness (right) for temperature computed per region (rows) for 3 vertical levels (columns) in the SPEEDY model. The bars represent one standard deviation of the metric around its mean. ET denotes LETKF and NS denotes MPNS-ETKF. 103

Figure 49. Verification of the truth with respect to the analysis ensemble mean for temperature at 510 hPa in the NH. The black line comes from the use of LETKF and the green line from the use of MPNS-ETKF. 104

Figure 50. Schematic for the leapfrog integration method. Successive integrations are shown with an alternation of pink and blue colors. Only the first integration is an extrapolation, the rest are centered integrations. 106

Figure 51. Time evolution of the 510hPa-geopotential height over College Park, MD using the SPEEDY model. The integration is performed using the leapfrog scheme using no filter (black line), the RA filter (red line) and the RAW filter (blue line).The appearance of spurious computational waves in the unfiltered integration occurs quickly (bottom panel) and leads to the loss of smoothness in the solution after a little over a month (top panel). 109

Figure 52. The impacts of different values of the parameter α of the RAW filter on the numerical amplification of an unforced, undamped wave; taken from Williams (2009). The value of $\alpha = 1$ corresponds to the original RA filter. The value of $\alpha = 0.53$ is a preferred choice, since it keeps the amplification close to its exact value (unity) over a broad frequency range. .. 111

Figure 53. Results of applying the t-test for difference of means in the variables $z510$ for each month with a local significance $\alpha_{local} = 0.05$. Under each map we indicate the number of grid points that resulted locally significant out of the 96x48 grid. One asterisk denotes that the variable is field significant ($\alpha_{field} = 0.05$) considering finite sample size, and two asterisks denote that it is field significant considering both finite sample size and spatial correlation. Only the month of September is field significant. 115

Figure 54. Probability mass function (left) and cumulative probability function (right) for the binomial distribution representing the total number of local significance tests passed (assuming

independence). For a total of 96x48 tests of local significance $\alpha_{local} = 0.05$, at least 255 must be passed in order to achieve a field significance $\alpha_{field} = 0.05$ 117

Figure 55. Distribution of the total number of local significance tests passed. The binomial distribution (black line) corresponds to the assumption of field independence. The empirical distributions (color lines), which consider the spatial correlation, are shown for four variables. These distributions were constructed via Monte Carlo simulation with 1000 iterations. The vertical lines indicate the 95th percentile for each distribution. It is noticeable that these values are substantially higher than the value of 255 (associated with the binomial distribution) appropriate for the spatially correlated variables. 121

Figure 56. Schematic depicting the experiment to assess the impact of the RAW filter in the accuracy forecasts. Starting from an initial condition coming from the NCEP reanalysis, *h*-hour forecasts are generated which later are verified using the ACC metric. 123

Figure 57. Increase in anomaly correlation coefficient ($\overline{ACC_{RAW}} - \overline{ACC_{RA}}$) for six different forecast times. The values were computed globally, for three different pressure levels, and for each of the five variables. The most benefited variables are the meridional wind and the geopotential height. The bars denote one standard deviation of the difference. 125

Figure 58. Increase in anomaly correlation coefficient ($\overline{ACC_{RAW}} - \overline{ACC_{RA}}$) for six different forecast times for two variables (geopotential height and meridional wind) at three pressure levels and four different latitudinal bands. The bars denote one standard deviation of the difference. . 126

Figure 59. Anomaly Correlation Coefficient for forecasts of surface pressure in the tropics. Notice that 96-hour forecasts using the RAW filter have approximately the same skill as 72-hour forecasts using the RA filter. Also, 120 hour forecasts using the RAW filter have approximately the same skill as 96-hour forecasts using the RA filter. 127

1. Introduction and objectives

1.1. Introduction

The goal of numerical weather prediction (NWP) is to determine the future state of the atmosphere by having some knowledge of its current conditions and performing a forward integration of the differential equations that describe its behavior (e.g. 3D Navier-Stokes equations, thermodynamical equation, etc.). This is not, however, an easy task. The atmosphere is a very complicated system with many degrees of freedom and a myriad of nonlinear processes happening at different space and time scales. Moreover, the atmosphere belongs to a type of dynamical systems known as chaotic. One of the primal characteristics of these systems is that trajectories starting from initial conditions infinitesimally close will diverge exponentially in time until their difference saturates at some climatological level (for a good introduction to chaos see *e.g.* Ott, 2004). Figure 1 illustrates this divergence of trajectories in the evolution of the 500-hPa geopotential height over College Park, Maryland.

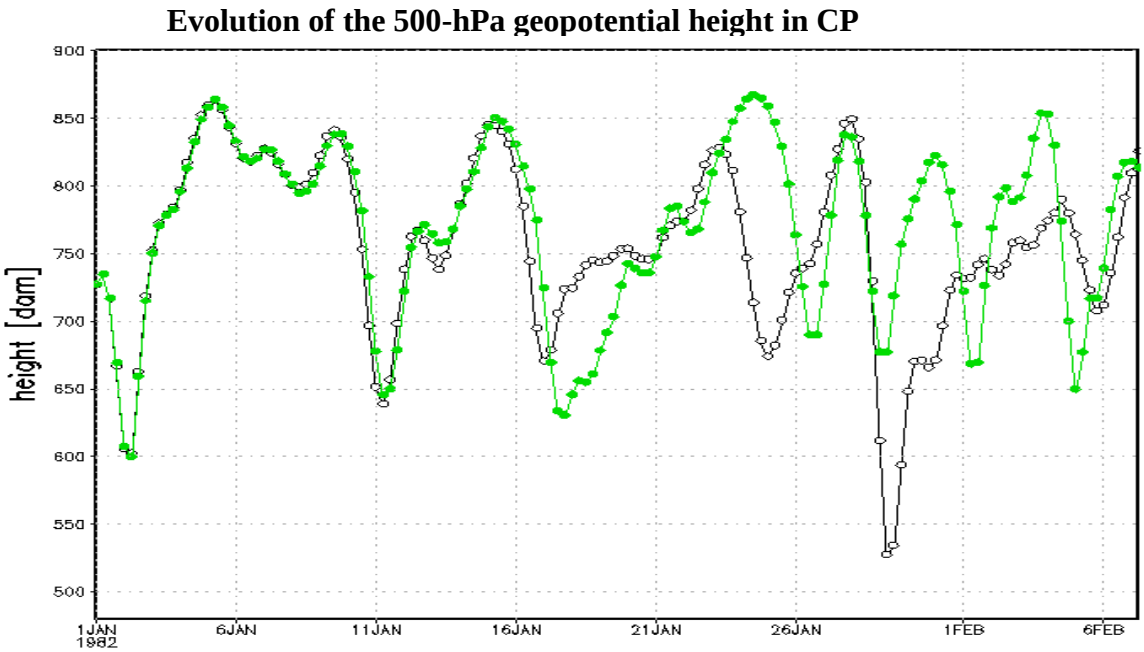

Figure 1. Time evolution of the 500-hPa geopotential height in College Park, MD, forecasted with the SPEEDY model (section 2.2.3).Two forecasts are started from infinitesimally close initial conditions, after ~10 days they start to differ considerably and after 2 weeks any resemblance is lost, exemplifying the chaotic behavior of the atmosphere.

It is then clear that an accurate knowledge of initial conditions is of paramount importance for NWP. Usually, two sources of information are available: (a) observations, which can be in-situ (e.g., weather balloons) or remote (e.g., Doppler radar or satellites), and (b) a previous forecast (i.e., information coming from models), which is labeled as "background". Both sources of information are prone to contain errors. The set of techniques used to blend together the information from models and observations in an optimal way, i.e., taking into consideration their respective uncertainities, is known as data assimilation (DA).

A detailed discussion of DA can be found in Daley (1991), Kalnay (2003) and Simon (2006); this introduction only provides some highlights. The DA process usually consists

of two parts: (a) the forecast, i.e. when the initial conditions are integrated forward in time using a forecast model, and (b) the assimilation, when the information coming from observations is blended in and 'corrects' the trajectory forecasted by the model. The resulting optimally-combined estimate is known as "analysis". A very simple schematic of the data assimilation process is presented in figure 2.

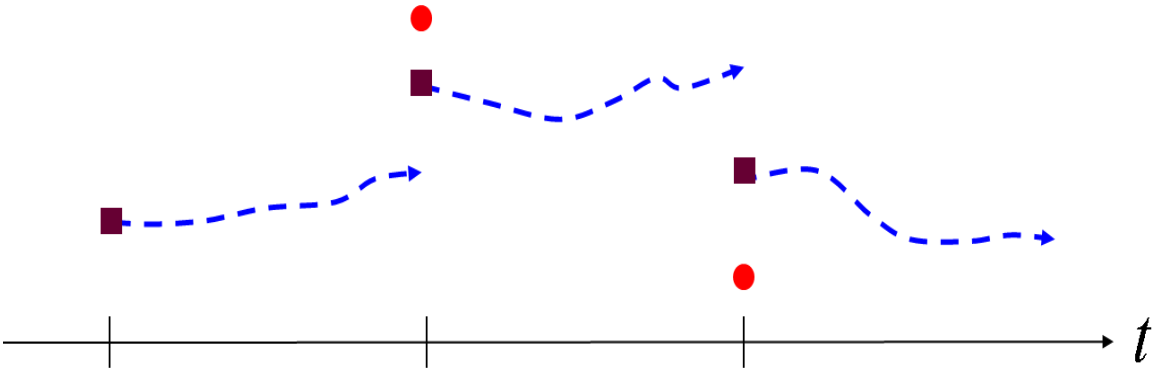

Figure 2. Schematic depicting a general data assimilation process. Information coming from forecasts (blue dashed line) is blended with that coming from observations (red dots) to get a better estimate of the truth, the analysis (purple squares). The analysis is used as the best initial condition for the next forecast.

The data assimilation problem can be posed as a maximum likelihood problem (variational DA) or as a minimum variance problem (sequential DA). In the case of Gaussian statistics for both the model error and the observational error, the two approaches can be shown to be equivalent. An additional goal of DA is to study the propagation of the initial uncertainty through the forecast window. Not all methods perform this task (e.g. optimal interpolation and 3D-var do not). In particular, the sequential DA methods based on the Kalman filter (KF) do. The present study deals with theoretical and implementations aspects of methods belonging to this category (see *e.g.* Evensen (2006) for a good introduction on these methods).

Once we have determined the 'best' initial conditions, the model equations must be integrated forward in time with some numerical scheme. This choice is not trivial. In general, there are several time-stepping schemes for the numerical integration of the differential equations representing the evolution of a dynamical system (e.g. table 1 in Durran 1991). The particular scheme chosen for any given integration will depend upon a compromise between the desired accuracy, stability, computational efficiency, ease of implementation, and run-time memory requirements. Whilst it is always hoped that simulations will be insensitive to time-stepping choices, the evidence suggests that this hope may be forlorn (e.g. Pfeffer et al. 1992; Williamson & Olson 2003; Zhao & Zhong 2009). Therefore, the following question naturally arises: Which of the many possible time-stepping schemes offers the most realistic simulations for the least computational expense?

This dissertation comprehends new developments in sequential DA and numerical weather forecasting. It is divided in three parts. The first two parts aims to strengthen the theory of some KF-based DA methods and allow for the development of useful applications. The first part revisits the recently proposed Ensemble Kalman-Bucy filter (EnKBF: Bergemman *et al*., 2009; Bergemman and Reich, 2010). In this formulation, the assimilation step of the DA problem is expressed by a set of ordinary differential equations (ODEs) instead of using linear algebra (as in the KF). The EnKBF has many potential advantages that can be exploited. Its quasi-continuous formulation allows "mollification" of the observational increments (Bergemann and Reich, 2010a), thus maintaining the balance of the analysis state at least as well as the widely used

Incremental Analysis Update (Bloom *et al.*, 1996). Furthermore, the continuous formulations are suitable for extensions that deal with non-Gaussian uni-modal and multi-modal ensemble distributions (Reich, 2011). Further inspection of these formulations, however, reveal that the ODEs involved in the EnKBF can become stiff under certain conditions. In this work we develop a numerical scheme that can handle this stiffness is developed. Furthermore, we propose an alternative in which the operations are performed in the ensemble space instead of in the model space, allowing the use of techniques that have been developed for transform-based formulations. Finally, it is important to mention that the EnKBF has only been tested with small models. This work is the first one to show that it can be used in atmospheric general circulation models (AGCMs), and hence it demonstrates that these formulations are good candidates to be used in real-life NWP applications. The results of this study led to a paper now under review in the Quarterly Journal of the Royal Meteorological Society (Amezcua *et al.*, 2012).

In the second part, we perform an analysis of a phenomenon related to deterministic ensemble square root filters (EnSRFs: Tippet et al, 2003) that arises when these formulations are used for data assimilation in the presence of strong nonlinearities. In ensemble clustering (EC), an *M*-member ensemble separates in an outlier and a cluster of *M-1* members. Results from previous works could lead to think that once this phenomenon sets in, it is irreversible. The intention of this work is to dispel this notion: we show that EC can be reverted naturally by the same nonlinearities of the system, and an explanation behind this behavior is provided. Some alternatives to traditional EnSRFs have been formulated to prevent EC; these alternatives include random rotations of the

analysis ensemble of perturbations. A simple and generic way to construct these formulations is provided. In particular, we show that using an orthonormal matrix that has a column of ones as eigenvector is sufficient to preserve the prescribed covariance and zero mean for the perturbations. A detailed comparison of the advantages and disadvantages of these methods with respect to traditional EnSRFs is presented. The results of this study led to a paper accepted in Tellus A (Amezcua *et al.*, 2012a).

The third part of this dissertation deals with a recently formulated improvement to the popular Robert-Asselin (RA) filter (Robert, 1966; Asselin, 1972). The RA filter successfully suppresses the spurious computational resulting from using a leap-frog integration scheme. Nonetheless, this filter can also damp physical waves and alter the mean value of the function being integrated. The Robert-Asselin-Williams (RAW) filter (Williams, 2009) is an improvement to ameliorate this problem. So far, the effects of the RAW filter have been tested only in a simple linear model representing inertial oscillations of the simple harmonic type (Williams, 2009). The objective of our study is to comprehensively evaluate the effects of the modification in the SPEEDY atmospheric general circulation model. It is our purpose to examine whether the use of the RAW filter changes either the climatology or the skill of weather forecasts, or both. Using statistical tests and considering significance both at local and field level (Livezey and Chen, 1983), it is shown that the climatology of the model is not changed by the new integration scheme. Therefore, the use of the new filter does not require a retuning of the model physics. On the other hand, using data from the NCEP-NCAR reanalysis (Kalnay *et al.*, 1996) we assess the impact of the new filter in deterministic forecasts. We find that the

new filter improve the forecasts for all variables (except relative humidity), especially in the medium range (4 to 6 days). The geopotential height in the tropics and the meridional wind in the midlatitudes are particularly benefited. The results of this study led to a paper now published in Monthly Weather Review (Amezcua *et al.*, 2011).

The second chapter of this dissertation presents a review of concepts of sequential data assimilation that are used in the remaining of the work. Also, a description of the three models used for experiments is provided. Chapters 3, 4 and 5 contain the main body of the dissertation, dealing with EnKBFs, EC and the RAW filter respectively. A brief chapter presenting a summary and future work concludes the work. Two appendices complement the dissertation: the first is related to the EnKBF chapter and the second provides a glossary of abbreviations and symbols used throughout this work.

1.2. Objectives

The objectives of this work are punctually listed for each one of the three parts separately.

Objectives related to the ensemble Kalman-Bucy filter:

- Show that the integration scheme used in the EnKBF stiffens for infrequent observations (corresponding to long assimilation windows) and provide an explanation of the mechanism that causes this stiffness.
- Develop an alternative integration scheme that is robust but not computationally expensive. Test this scheme in highly nonlinear systems.
- Develop a transform-based alternative for the EnKBF in which the operations are performed in state space and not in model space. Explain the benefits of this formulation and complement its formulation with a gridpoint R-localization scheme.
- Prove that the EnKBF can be used for data assimilation in atmospheric models.

Objectives related to ensemble clustering

- Develop a metric to quantify EC in a simple and tangible manner.
- Starting from a simple nonlinear model, show that EC is not an irreversible process. Thus, show that EnSRFs are not helplessly handicapped in the presence of strong nonlinearity.
- Show that clustering can set in and reverse in a natural way. Provide an explanation for this phenomenon.

- Analyze randomly rotated EnSRF and compare the advantages and disadvantages with respect to traditional EnSRFs.

- Explore the impact of EC in application with atmospheric models.

Objectives related to the RAW filter

- Considering statistical significance both at the local and field level, find whether the use of the RAW filter affects the climatology of the SPEEDY model.

- Evaluate if the use of the RAW filter leads to any improvements in forecasts of the SPEEDY model.

2. Background

This chapter is divided in two parts. In the first, the concepts and tools related to data assimilation are introduced and discussed. In the second part, we present the details of three models of increasing complexity; these models will allow us to test the ideas presented in the next sections.

2.1. Concepts of sequential data assimilation

2.1.1. Kalman Filter

The Kalman Filter (KF: Kalman, 1960) is a sequential data assimilation technique widely used in control theory and applications. The KF deals with discrete systems which can be expressed as linear difference equations of the form:

$$\mathbf{x}_t = \mathbf{A}_{t-1}\mathbf{x}_{t-1} + \mathbf{w}_t \qquad \mathbf{x} \in \Re^N \tag{1}$$

$$\mathbf{y}_t = \mathbf{H}_t\mathbf{x}_t + \mathbf{v}_t \qquad \mathbf{y} \in \Re^L \tag{2}$$

Equation (1) represents the linear evolution of the state variables $\mathbf{x} \in \Re^N$ from the instant $t-1$ to the instant t by the action of the state transition matrix $\mathbf{A} \in \Re^{N \times N}$. The stochastic term $\mathbf{w}_t \sim N(\mathbf{0}, \mathbf{Q})$ represents the (unbiased) model error, which may come from inadequacies in the model, subgrid processes that cannot be represented explicitly or other sources of error. In the rest of this discussion, we will consider a perfect model scenario, i.e. $\mathbf{w}_t = \mathbf{0}$. Equation (2) defines the observations $\mathbf{y} \in \Re^L$ as a linear

combination of state variables transformed by the (observation) matrix $\mathbf{H} \in \Re^{L \times N}$ plus a stochastic term $\mathbf{v}_t \sim N(\mathbf{0}, \mathbf{R})$ that represents the observational error, with $\mathbf{R} \in \Re^{L \times L}$ being the observational error covariance (usually assumed to be diagonal).

The KF solves this estimation problem as a two-step process. The first is the forecast from time $t-1$ to time t of both the estimator for the state variables $\hat{\mathbf{x}}$ and their error covariance matrix $\mathbf{P}$. This step is perfomed as:

$$\mathbf{P}_t^b = \mathbf{A}_{t-1} \mathbf{P}_{t-1}^b \mathbf{A}_{t-1} \tag{3}$$

$$\hat{\mathbf{x}}_t^b = \mathbf{A}_{t-1} \hat{\mathbf{x}}_{t-1}^b \tag{4}$$

Equation (3) represents the evolution of the estimator of the covariance of the state variables, denoted as the matrix $\mathbf{P} \in \Re^{N \times N}$, while equation (4) represents the evolution of the estimator of the state variables $\hat{\mathbf{x}}$. The superscript b stands for background (or forecast), a label used to denote that the information obtained from observations has not been assimilated yet. The superscript a stands for analysis, denoting that the information from observations has already been included.

The second is the assimilation of observations at time t done by least squares optimization, resulting in the following expressions (where we drop the time subindex t):

$$\mathbf{P}^a = \left(\mathbf{I} - \mathbf{K}\mathbf{H}^T\right)\mathbf{P}^b \tag{5}$$

$$\hat{\mathbf{x}}^a = \hat{\mathbf{x}}^b - \mathbf{K}\left(\mathbf{H}\hat{\mathbf{x}}^b - \mathbf{y}\right) \tag{6}$$

The matrix $\mathbf{K}$ is known as the Kalman gain, and is given by:

$$\mathbf{K} = \mathbf{P}^b \mathbf{H}^T \left(\mathbf{H}\mathbf{P}^b \mathbf{H}^T + \mathbf{R}\right)^{-1} = \mathbf{P}^a \mathbf{H}^T \mathbf{R}^{-1} \tag{7}$$

The KF can be considered as a least squares minimization procedure in which *both* the estimator of the state variable as well as its uncertainty are evolved in time.

2.1.2. Kalman-Bucy filter

The KF considers both the state variables and the observations to be discrete. A continuous-time equivalent is known as the Kalman-Bucy Filter (KBF: Kalman and Bucy, 1961). In this case, both the state variables and the observations are considered to be continuous functions of time. The ODEs from which the KBF departs are the following:

$$\frac{d}{dt}\mathbf{x}(t) = \mathbf{F}(t)\mathbf{x}(t) + \mathbf{w}(t) \tag{8}$$

$$\mathbf{y}(t) = \mathbf{H}(t)\mathbf{x}(t) + \mathbf{v}(t) \tag{9}$$

The elements in these equations are the same as the ones described for (1) & (2), with the only difference that $\mathbf{w}(t)$ and $\mathbf{v}(t)$ now represent continuous time white noise processes[1]. Again we consider a perfect model, i.e, $\mathbf{w}(t) = \mathbf{0}$. The matrix $\mathbf{F}(t)$ represents the linear dynamics of the system; the matrix $\mathbf{A}$ in (1) is given by the resolvent of (8). In the solution to this estimation problem there is no distinction between the forecast and the

[1] See e.g. Simon 2006 for a complete discussion on discrete vs. continuous white noise.

analysis steps; they are represented together in the solution of a system of ODEs (see appendix A for a detailed derivation):

$$\frac{d\mathbf{P}}{dt} = -\mathbf{P}\mathbf{H}^T\mathbf{R}^{-1}\mathbf{H}\mathbf{P} + \mathbf{F}\mathbf{P} + \mathbf{P}\mathbf{F}^T \tag{10}$$

$$\frac{d\hat{\mathbf{x}}}{dt} = \mathbf{F}\hat{\mathbf{x}} - \mathbf{P}\mathbf{H}^T\mathbf{R}^{-1}\left(\mathbf{H}\hat{\mathbf{x}} - \mathbf{y}\right) \tag{11}$$

Equation (10) describes the evolution and assimilation of the covariance; it is usually referred to as the Riccati equation[2] for the covariance. Equation (11) corresponds to the evolution and assimilation of the mean.

There is no major problem in considering the state variables to be continuous. In many cases we have continuous time systems expressed as differential equations which we discretize in order to allow their numerical solution. However, it is more difficult to consider observations as being continuous. Conceptually, they can be regarded as a transformation of the state variables into observation space, but they are not available at any arbitrary time. In fact, dynamical systems can rarely be observed even with the frequency of the time step used in the numerical solution of the model.

To assimilate observations at a discrete time, one can use the Kalman-Bucy formulation by adopting a *pseudo-time* s spanning over $0 \le s \le 1$ out of an instant t (Bergemann *et al.*, 2009). The KBF equations in pseudo-time are:

[2] A scalar Riccati equation is a non-linear ordinary differential equation, whose non-linearity comes from a quadratic term of the dependent variable $x(t)$. It's general form is: $\dot{x}(t) = a_o(t) + a_1(t)x(t) + a_2(t)(x(t))^2$. The matrix Ricatti equation is a generalization of the former and is of great interest in control theory.

$$\frac{d\mathbf{P}}{ds} = -\mathbf{P}\mathbf{H}^T\mathbf{R}^{-1}\mathbf{H}\mathbf{P} \tag{12}$$

$$\frac{d\hat{\mathbf{x}}}{ds} = -\mathbf{P}\mathbf{H}^T\mathbf{R}^{-1}\left(\mathbf{H}\hat{\mathbf{x}} - \mathbf{y}\right) \tag{13}$$

Given the initial conditions in pseudo-time $\mathbf{P}(0) = \mathbf{P}^b$, $\hat{\mathbf{x}}(0) = \hat{\mathbf{x}}^b$, integrating (6) and (7) one obtains $\mathbf{P}^a = \mathbf{P}(1)$, $\hat{\mathbf{x}}^a = \hat{\mathbf{x}}(1)$, i.e., starting from the background values at the beginning of the pseudo-time window, one obtains the analysis values at the end of the window. A schematic representation of the spanning of pseudo-time is shown in the next figure.

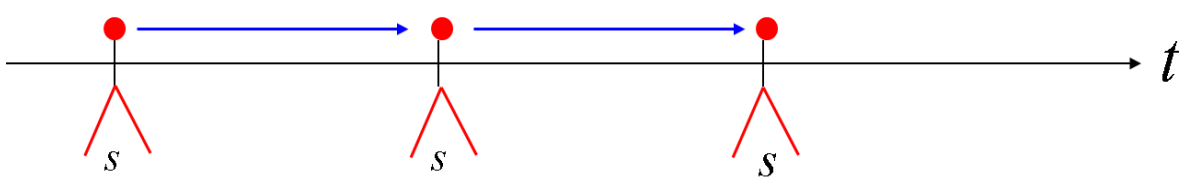

Figure 3. Schematic representation pseudo-time in the EnKBF, it is spanned at each assimilation instant.

It is possible to show that the solution of these two differential equations at $s = 1$ is equivalent to the system (5) & (6). By performing a factorization for the covariance matrix as $\mathbf{P} = \mathbf{L}\mathbf{Y}^{-1}$, one can show that the solution in pseudo-time $0 \le s \le 1$ for the covariance is (see details in appendix A):

$$\mathbf{P}(s) = \mathbf{P}^b\left(\mathbf{H}^T\mathbf{R}^{-1}\mathbf{H}\mathbf{P}^b s + \mathbf{I}\right)^{-1} \tag{14}$$

2.1.3. Ensemble Kalman Filters

Both the KF and the KBF deal with linear equations for the forecast step, but many dynamical systems of interest –in particular those found within the atmospheric sciences- are nonlinear. For these systems, (1) is replaced by:

$$\mathbf{x}_t = f\left(\mathbf{x}_{t-1}\right) \tag{15}$$

where f represents the nonlinear model operator. The Extended Kalman Filter (EKF) was developed to handle this case. This generalization of the KF is based upon the first order truncation of the Taylor expansion of the nonlinear model around some point of reference of the state variables, i.e. it uses a tangent model to advance the system. Detailed descriptions of the EKF and their application to atmospheric and oceanic sciences can be found in Ghil (1989) and Miller *et al.* (1994). While effective, the EKF is suited for small systems with a relatively small number of state variables, but quickly becomes computationally expensive as the number of state variables gets large. It is virtually impossible for this method to be applied to higher order models. This is the case of atmospheric models, where the number of state variables is typically $O\left(10^6\right) - O\left(10^9\right)$.

The Ensemble Kalman Filter (EnKF) is a Monte Carlo alternative to the EKF. In the EnKF, one takes an ensemble of M solutions of equation (15) -usually $M << N$- and evolves each member with the nonlinear model f. The matrix for the ensemble can be denoted as:

$$\overline{\overline{\mathbf{X}}} = \left[\mathbf{x}_1 \,|\, \mathbf{x}_2 \,|\cdots|\, \mathbf{x}_M\right] \qquad \overline{\overline{\mathbf{X}}} \in \Re^{N \times M} \tag{16}$$

where we use the subscript to represent the individual members of the ensemble. Let $\mathbf{1} \in \Re^M$ be a column vector of ones, then the sample mean of the ensemble is:

$$\bar{\mathbf{x}} = \frac{1}{M}\sum_{i=1}^{M}\mathbf{x}_i = \frac{1}{M}\bar{\bar{\mathbf{X}}}\mathbf{1} \tag{17}$$

An ensemble of perturbations can be defined by subtracting the sample mean column from each column of the ensemble. Let $\mathbf{U} = M^{-1}\,\mathbf{1}\mathbf{1}^T$, $\mathbf{U} \in \Re^{M\times M}$ is idempotent ($\mathbf{U}^n = \mathbf{U}$); then the ensemble of perturbations can be written as:

$$\mathbf{X} = \left[\mathbf{x}_1 - \bar{\mathbf{x}} \,|\, \mathbf{x}_2 - \bar{\mathbf{x}} \,|\, \cdots \,|\, \mathbf{x}_M - \bar{\mathbf{x}}\right] = \bar{\bar{\mathbf{X}}}\left(\mathbf{I} - \mathbf{U}\right) \tag{18}$$

Using the ensemble of perturbations we can obtain the sample covariance:

$$\mathbf{P} = \left(M-1\right)^{-1}\mathbf{X}\mathbf{X}^T = \left(M-1\right)^{-1}\bar{\bar{\mathbf{X}}}\left(\mathbf{I} - \mathbf{U}\right)\bar{\bar{\mathbf{X}}}^T \tag{19}$$

For the assimilation cycles in the EnKF one must obtain the analysis ensemble from the background ensemble. This is not an obvious task since obtaining $\mathbf{X}$ from $\mathbf{P}$ in (12) has an infinite number of solutions: let $\mathbf{P} = \left(M-1\right)^{-1}\mathbf{X}\mathbf{X}^T$ and $\mathbf{Z} = \mathbf{X}\mathbf{\Phi}$, then $\mathbf{P}_\mathbf{Z} = \left(M-1\right)^{-1}\mathbf{Z}\mathbf{Z}^T = \mathbf{P}$ for any unitary matrix $\mathbf{\Phi}$.

Evensen's original idea (1994) was to update each member in the same way the mean is updated. A revision of this method (Burgers *et al.*, 1998; Houtekamer and Mitchell, 1998) is known as the 'perturbed observations' method. In this case, for each ensemble member the observations are randomly perturbed to avoid the ensemble collapse. The

stochastic EnKF, however, does not fulfill the KF covariance equation exactly, but only in a statistical sense.

Another way to update the perturbations -which is deterministic rather than stochastic- is the family of square root filters (EnSRFs Tippett *et al.*, 2003). The deterministic EnKFs rely on explicit mathematical transformations for the ensemble update. Some members of this family are the Ensemble Adjustment Kalman Filter (EAKF, Anderson, 2001), the serial EnSRF (Whitaker and Hamill, 2002), the Ensemble Transform Kalman Filter (Bishop *et al*, 2001; Wang *et al*, 2004) and the Local Ensemble Transform Kalman Filter (Ott *et al.*, 2004, Hunt *et al.*, 2007).

2.1.4. Local Ensemble Transform Kalman Filter and a non-symmetric solution

In this work we will use as reference a post-multiplication-type EnSRF known as local ensemble transform Kalman filter (LETKF; Hunt *et al.*, 2007). This formulation is unbiased (Livings *et al.*, 2008), and without localization it is equivalent to the spherical-symplex ETKF (Wang et al, 2004). The LETKF obtains the analysis ensemble of perturbations $\mathbf{X}^a$ by a post-multiplication of the background ensemble of perturbations and a matrix of weights:

$$\mathbf{X}^a = \mathbf{X}^b \mathbf{W}^a \tag{20}$$

$\mathbf{W}^a$ has to be obtained in a way such that $\mathbf{P}^a$ has the value prescribed by the KF. In particular, for the LETKF:

$$\mathbf{W}^a = \mathbf{C}(\mathbf{I}+\mathbf{\Gamma})^{-1/2}\mathbf{C}^{\mathbf{T}} = \left((M-1)\tilde{\mathbf{P}}^a\right)^{1/2} \tag{21}$$

where

$$\mathbf{C}\,\mathbf{\Gamma}\,\mathbf{C}^{\mathbf{T}} = eig\left(\frac{\mathbf{Y}^{\mathbf{b}\,\mathbf{T}}\mathbf{R}^{-1}\mathbf{Y}^{\mathbf{b}}}{M-1}\right) \tag{22}$$

The matrix $\mathbf{Y}^{\mathbf{b}} = \mathbf{H}\mathbf{X}^{\mathbf{b}}$ is the mapping of the ensemble of background perturbations into observational space. The matrix $\mathbf{\Gamma}$ contains the eigenvalues of the multidimensional ratio of ensemble covariance (projected into observational space) and observational error covariance, while $\mathbf{C}$ is the matrix with the corresponding eigenvectors as columns. As indicated in (21), $\mathbf{W}^a$ is proportional to the symmetric square root of the analysis covariance in ensemble space $\tilde{\mathbf{P}}^a$. This solution minimizes the 'distance' between $\mathbf{W}^a$ and the identity matrix, thus getting an $\mathbf{X}^a$ as close as possible as $\mathbf{X}^b$ (Ott *et al.*, 2004). This form automatically guarantees the analysis perturbations to be unbiased (Hunt *et al.*, 2007; Livings *et al.*, 2008), i.e.

$$\mathbf{X}^a\mathbf{1} = \mathbf{0} \tag{23}$$

where $\mathbf{1} \in \Re^M$ and $\mathbf{0} \in \Re^N$. The mean analysis mean can be computed as:

$$\overline{\mathbf{x}}^a = \overline{\mathbf{x}}^b + \mathbf{X}^b\overline{\mathbf{w}}^a \tag{24}$$

i.e. a lineal combination of the ensemble of background perturbations departing from the background mean. The vector of weights $\overline{\mathbf{w}}^a$ is computed in the following way:

$$\overline{\mathbf{w}}^{a} = \frac{\mathbf{W}^{a}\mathbf{W}^{a^{T}}}{M-1}\mathbf{Y}^{b^{T}}\mathbf{R}^{-1}\left(\mathbf{y}-\overline{\mathbf{y}}^{b}\right) \tag{25}$$

where $\overline{\mathbf{y}}^{b} = \mathbf{H}\overline{\mathbf{x}}^{\mathbf{b}}$ is the projection of the background mean into observational space.

The factor $\mathbf{C}(\mathbf{I}+\mathbf{\Gamma})^{-1/2}$ in $\mathbf{W}^{a}$ is enough to guarantee the fulfillment of the KF covariance equation. A general non-symmetric ETKF can be written as

$$\mathbf{W}^{a} = \mathbf{C}(\mathbf{I}+\mathbf{\Gamma})^{-1/2}\mathbf{S}^{\mathbf{T}} \tag{26}$$

where $\mathbf{S}$ is any orthonormal matrix. Equation (26) does not automatically guarantee the analysis perturbations to be unbiased, i.e.

$$\mathbf{X}^{\mathbf{a}}\mathbf{1} = \mathbf{0} \tag{27}$$

where $\mathbf{1} \in \Re^{M}$. The symmetric solution is unbiased (Wang et al, 2004; Hunt et al, 2007), a non-symmetric solution will be unbiased if $\mathbf{S}$ is such that $\mathbf{W}$ contains $\mathbf{1}$ as an eigenvector. A simple way to construct a matrix $\mathbf{S}$ with the desired zero-mean preserving characteristic is presented in chapter 4. We denominate any solution of this form a Mean-Preserving Non-Symmetric ETKF (MPNS-ETKF). These types of solutions -which involved a random rotation through the action of the matrix $\mathbf{S}$- can be regarded a constrained resampling of the ensemble, akin to that used in particle filters (see e.g. Spiller *et al.*, 2008).

2.1.5. Ensemble Kalman-Bucy Filters

The pseudo-time implementation of the KBF discussed in section 2.1.2 can also be used in an ensemble setting. Starting from (12), BGR09 used the sample estimator for covariance:

$$\frac{d}{ds}\left[\frac{\mathbf{X}\mathbf{X}^T}{M-1}\right] = -\frac{\mathbf{X}\mathbf{X}^{\mathbf{T}}}{M-1}\mathbf{H}^{\mathbf{T}}\mathbf{R}^{-1}\mathbf{H}\frac{\mathbf{X}\mathbf{X}^{\mathbf{T}}}{M-1} \tag{28}$$

One can use the chain rule for the derivative in the left hand side.

$$\left(\frac{d}{ds}\mathbf{X}\right)\mathbf{X}^{\mathbf{T}} + \mathbf{X}\left(\frac{d}{ds}\mathbf{X}^{\mathbf{T}}\right) = 2\left(\frac{d}{ds}\mathbf{X}\right)\mathbf{X}^{\mathbf{T}} = -\frac{1}{M-1}\mathbf{X}\mathbf{X}^{\mathbf{T}}\mathbf{H}^{\mathbf{T}}\mathbf{R}^{-1}\mathbf{H}\mathbf{X}\mathbf{X}^{\mathbf{T}}$$

A simplification leads to the equation for the update the ensemble of perturbations using the sample covariance:

$$\boxed{\frac{d\mathbf{X}}{ds} = -\frac{1}{2(M-1)}\mathbf{X}\mathbf{X}^T\mathbf{H}^T\mathbf{R}^{-1}\mathbf{H}\mathbf{X}} \tag{29}$$

so that given $\mathbf{X}(0) = \mathbf{X}^b$ we can obtain $\mathbf{X}^a = \mathbf{X}(1)$. Thus the perturbations are updated via an ODE while the mean is still updated using (6) with the sample estimators. The BGR09 computational implementation is as follows: given $\mathbf{X}^b$ compute $\mathbf{X}^a$ by the numerical integration of (29). Then compute $\mathbf{K} = (M-1)^{-1}\mathbf{X}^a\mathbf{X}^{a^T}\mathbf{H}^T\mathbf{R}^{-1}$ and use it to compute $\bar{\mathbf{x}}^a$ by (6).

BR10 differs from BGR09, in that the two Bucy equations in pseudo-time (12) and (13) are combined to get a single ODE formulation for the full ensemble itself; a brief derivation of BR10 is presented next. The ODE representing the analysis step for the full ensemble can be written as:

$$\frac{d\overline{\overline{\mathbf{X}}}}{ds} = \frac{d}{ds}\left(\mathbf{X} + \bar{\mathbf{x}}\mathbf{1}^T\right) = \frac{d}{ds}\mathbf{X} + \left(\frac{d}{ds}\bar{\mathbf{x}}\right)\mathbf{1}^T \tag{30}$$

The two terms of in this equation correspond to the ensemble version of the KBF equations for the perturbations (29) and the mean:

$$\frac{d\bar{\mathbf{x}}}{ds} = -\frac{1}{M-1}\mathbf{X}\mathbf{X}^T\mathbf{H}^T\mathbf{R}^{-1}\left(\mathbf{H}\bar{\mathbf{x}} - \mathbf{y}\right) \tag{31}$$

Substitute (29) and (31) into (30) and factorize:

$$\frac{d\overline{\overline{\mathbf{X}}}}{ds} = -\frac{1}{M-1}\mathbf{X}\mathbf{X}^T\mathbf{H}^T\mathbf{R}^{-1}\left[\frac{1}{2}\mathbf{H}\mathbf{X} + \left(\mathbf{H}\bar{\mathbf{x}} - \mathbf{y}\right)\mathbf{1}^T\right] \tag{32}$$

This equation describes the assimilation of the $\overline{\overline{\mathbf{X}}}$ in terms of $\mathbf{X}$ and $\bar{\mathbf{x}}$. To obtain an expression in terms of $\overline{\overline{\mathbf{X}}}$, recall that $\bar{\mathbf{x}} = M^{-1}\overline{\overline{\mathbf{X}}}\mathbf{1}$ and $\mathbf{X} = \overline{\overline{\mathbf{X}}}\left(\mathbf{I} - \mathbf{U}\right)$, where $\mathbf{U} = M^{-1}\mathbf{1}\mathbf{1}^T$. Substituting these into (32), using the fact that $\mathbf{I} - \mathbf{U}$ is idempotent and simplifying we obtain the BR10 formulation:

$$\boxed{\frac{d\overline{\overline{\mathbf{X}}}}{ds} = -\frac{1}{2(M-1)}\overline{\overline{\mathbf{X}}}\left[\mathbf{I} - \mathbf{U}\right]\overline{\overline{\mathbf{X}}}^T\mathbf{H}^T\mathbf{R}^{-1}\left[\mathbf{H}\overline{\overline{\mathbf{X}}}\left[\mathbf{I} + \mathbf{U}\right] - 2\mathbf{y}\,\mathbf{1}^T\right]} \tag{33}$$

In this formulation, the entire ensemble is updated by solving (33) as $\overline{\overline{\mathbf{X}}}^{a} = \overline{\overline{\mathbf{X}}}(1)$ given $\overline{\overline{\mathbf{X}}}(0) = \overline{\overline{\mathbf{X}}}^{b}$. We note that this equation appears in BR10 in the equivalent form of the gradient of a cost function.

A fundamental difference between BGR09 and BR10 is that BGR09 computes the analysis mean $\bar{\mathbf{x}}^{a}$ separately using (6). Accordingly, observations $\mathbf{y}$ themselves impact only the analysis mean $\bar{\mathbf{x}}^{a}$ but not the analysis ensemble perturbation $\mathbf{X}^{a}$. In BGR10, observations $\mathbf{y}$ affect both $\mathbf{X}^{a}$ and $\bar{\mathbf{x}}^{a}$. This difference can be important for numerical implementations as the update of the ensemble mean will be affected by the chosen time-stepping. It is worth mentioning that neither BGR09 nor BR10 requires any matrix inversion except $\mathbf{R}^{-1}$, which is frequently diagonal and usually can be pre-computed.

2.2. Dynamical models used in this work

Here we present a description of the three dynamical systems used for experiments in this work. For all our experiments, identical twin experiments are carried out. In this type of experiments there are three elements: the nature run (truth), the observations and the background/analysis ensemble.

Each one of the models allows testing different aspects: very strong nonlinearities, the need for localization and multiplicative covariance inflation, as well as situations that mimic real-life NWP aspects.

2.2.1. The Lorenz 1963 model

The Lorenz 1963 model (L63) is a strongly nonlinear 3-variable model widely used in evaluating data assimilation schemes because of its challenging properties near regime changes (e.g. Miller *et al.*, 1994; Evensen, 1998; Evans *et al.*, 2004). It comes from the simplification of the Rayleigh-Benard convection process (Lorenz, 1963). The system of nonlinear coupled ODEs describing its evolution is:

$$\begin{aligned} \dot{x}^{(1)} &= \sigma\left(x^{(2)} - x^{(1)}\right) \\ \dot{x}^{(2)} &= x^{(1)}\left(r - x^{(3)}\right) - x^{(2)} \\ \dot{x}^{(3)} &= x^{(1)}x^{(2)} - bx^{(3)} \end{aligned} \tag{34}$$

The standard values used for the parameters are: $\sigma = 10$, $r = 28$ and $b = 8/3$. This choice results in a chaotic behavior with two regimes in a very well-known butterfly-shaped fractal attractor in the phase space. The model is integrated with the Runge-Kutta

4th order method using a time step of $\Delta t = 0.01$. A depiction of the time evolution of the variables as well as a snapshot of the attractor is presented next.

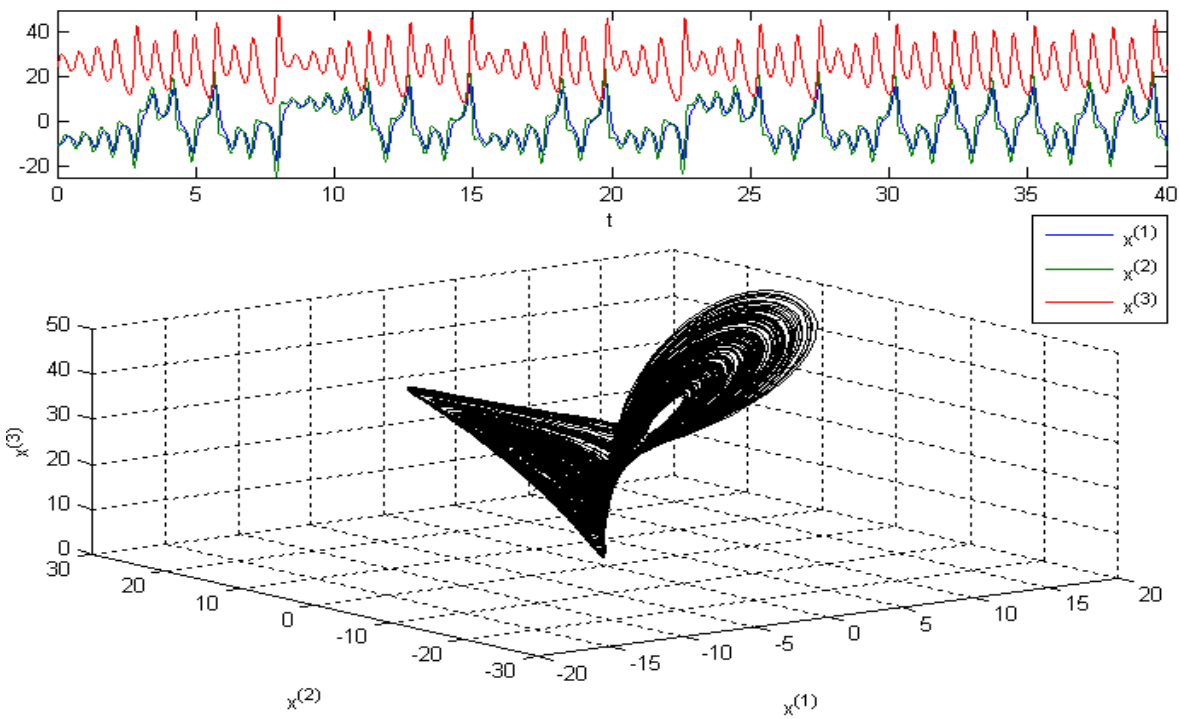

Figure 4. Lorenz 1963 model. The top panel depicts the time evolution of the three variables in the model. The bottom panel shows the shape of the attractor in phase space.

2.2.2. The 40-variable Lorenz 1996 model

The 40-variable L96 model (Lorenz 1996; Lorenz and Emanuel, 1998) is described by the set of differential equations:

$$\dot{x}^{(q)} = \left(x^{(q+1)} - x^{(q-2)}\right)x^{(q-1)} - x^{(q)} + F \tag{35}$$

for $q = 1,\ldots,40$, with $x^{(0)} = x^{(40)}$, $x^{(-1)} = x^{(39)}$ and $x^{(41)} = x^{(1)}$. The model is designed to mimic the time evolution of an atmospheric variable in a circle of latitude. The model is

schematic; it cannot be derived from physical laws (Lorenz, 2005). Nonetheless it represents a system in which three processes are present: nonlinear advection (first term), dissipation (second term) and forcing (last term, which is usually given a numerical value $F = 8$). The attractor of this model has a fractal dimension of about 27 and it has 13 positive Lyapunov exponents (Lorenz, 2005). It does not have regime transitions as L63. The model is integrated with a Runge-Kutta 4th order method and a time step of $\Delta t = 0.025$ units.

Figure 5 illustrates the behavior of this model. All variables are started from the (unstable) steady state $x^{(j)}(t=0) = F, \forall j$ except for a variable that is initially perturbed: $x^{(20)}(t=0) = F + 0.001$. One can notice that the transient lasts less than 2 time units. The left side of figure 5 shows the time evolution of 4 selected variables. The right side is a Hovmoller diagram showing the time evolution of all variables. In this diagram one can visualize the westward propagation of waves.

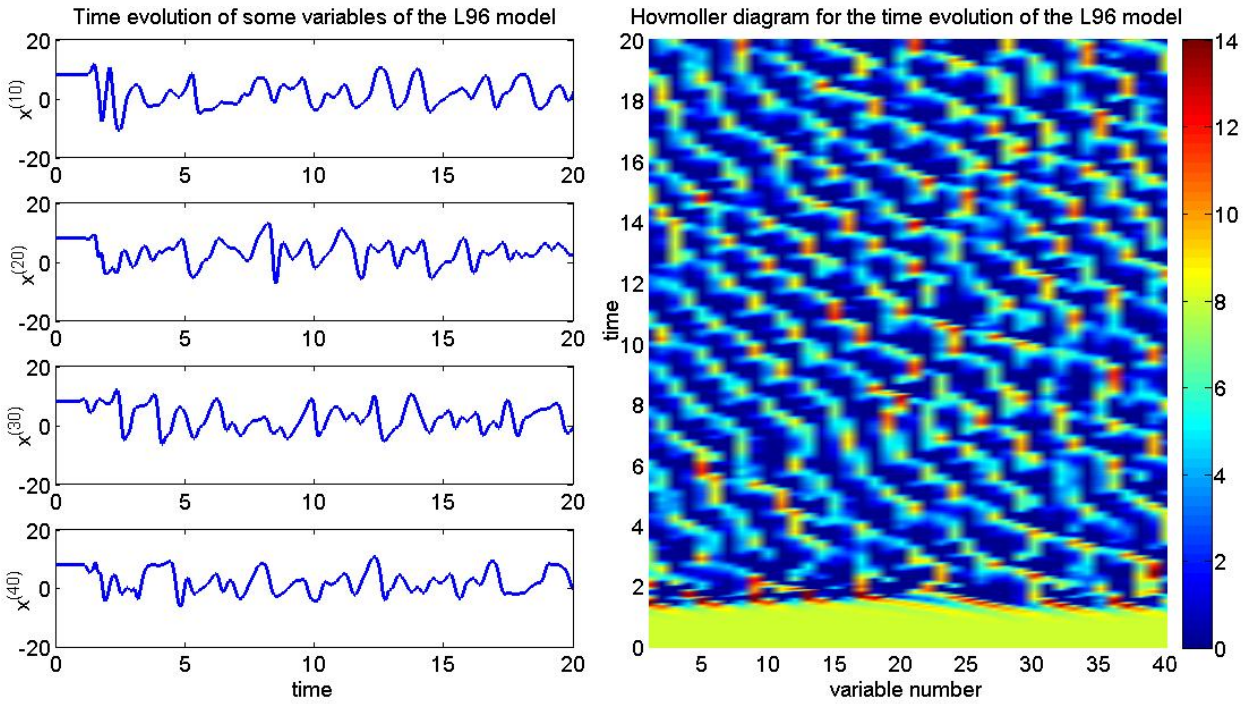

Figure 5. Lorenz 1996 model: time evolution of selected variables (left) and all the 40 variables using a Hovmoller diagram (right).

This model allows experiments with implementation aspects such as localization and multiplicative covariance inflation.

2.2.3. A medium complexity AGCM: SPEEDY

The Simplified Parameterizations, primitivE-Equation Dynamics (SPEEDY) model is a medium complexity Atmospheric General Circulation Model (AGCM) developed by Molteni (2003). As its name indicates, this model has a spectral primitive-equation dynamic core and a set of simplified physical parameterization schemes. It is useful for our experiments because it achieves computational efficiency while maintaining realistic simulations similar to those of state-of-the-art AGCMs with complex physics. Hence, it allows us to mimic situations that would arise in a real NWP scenario.

Miyoshi (2005) adapted SPEEDY for use in data assimilation, with output every 6 hours (the model time step is 40 minutes). This implementation has a resolution of T30L7, with horizontal spectral truncation at 30 wave numbers and 7 vertical levels. Data are output on a horizontal grid of 96 longitudinal and 48 latitudinal points. The model includes basic physical parameterizations, the description of which can be found in the appendix of Molteni (2003). It is based on a spectral dynamical core developed at the Geophysical Fluid Dynamics Laboratory. SPEEDY is a hydrostatic model formulated in σ coordinates, in the vorticity-divergence form described by Bourke (1974). It calculates five field variables: zonal wind u, meridional wind u, temperature T, relative humidity q and surface pressure ps. The geopotential height z for different pressure levels may be obtained by interpolation (since it is hydrostatic).

One can generate artificial observations that resemble a realistic radiosonde observational network as presented in figure 6 (reproduced from Miyoshi 2005). The observation density is higher over continents than over the oceans, and the Northern Hemisphere (NH) is better observed than the Southern Hemisphere (SH). In our experiments, observations are generated by adding Gaussian random perturbations to every variable (in each one of the 7 vertical levels) with the following standard deviations: 1 m/s for *u* and *v*, 1 K for *T*, 10^{-3} kg/kg for *q* and 1 hPa for *ps*.

To assess the performance of assimilation techniques in this model, a latitude-weighted RMSE was computed for each one of the variables:

$$RMSE_{lat-wei} = \sqrt{\frac{1}{J}\sum_{j=1}^{J}\left(x_j^t - x_j^a\right)^2 \cos\varphi_j} \tag{36}$$

where x^t corresponds to the nature run, x^a corresponds to the analysis, and φ is the latitude angle and J is the total number of state variables. Each one of the 6 variables (u, v, T, q, ps, z) should be considered separately at each one of the 7 vertical levels.

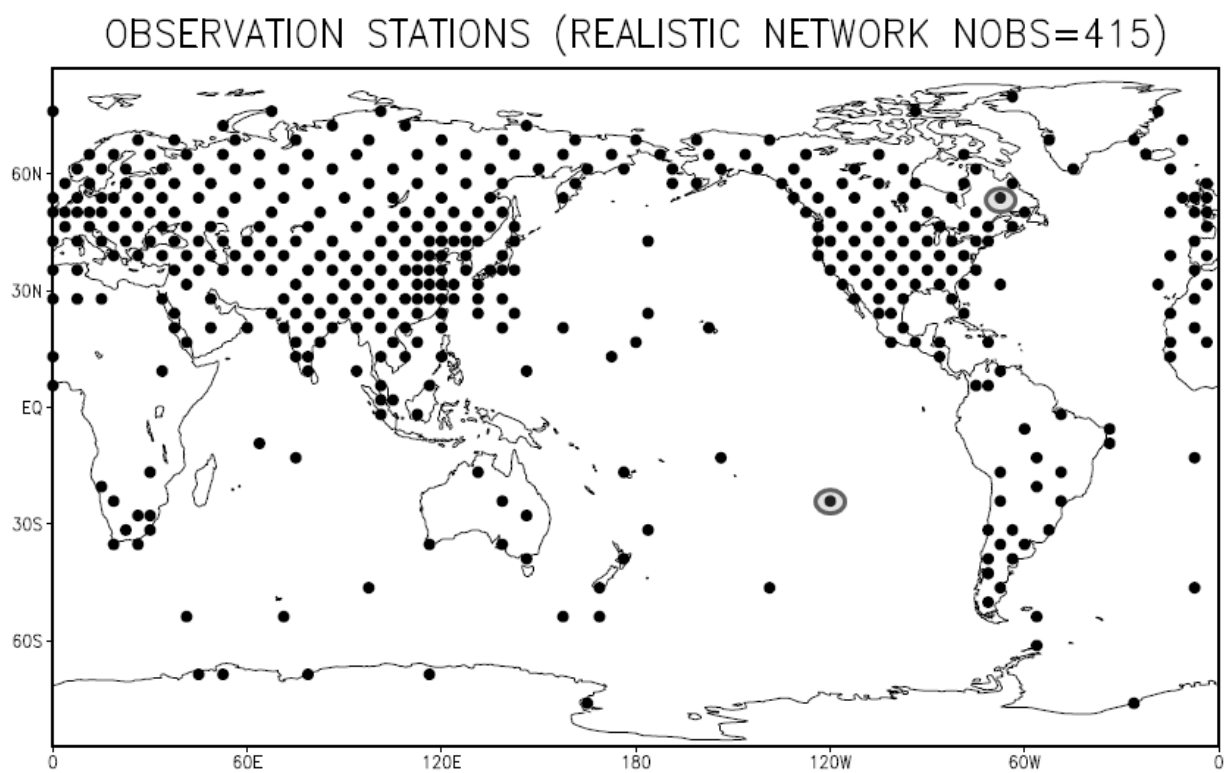

Figure 6. Observational density used for the experiments with the SPEEDY model. The spatial distribution of the observations resembles a realistic radiosonde network (Miyoshi, 2005). Two positions are circled, one over the Labrador Peninsula and other over the Southern Pacific Ocean; these locations will be used to display results in subsequent sections.

Furthermore, the RMSE can be computed separately for different geographical regions: NH, tropics and SH.

3. Analysis on the Ensemble Kalman-Bucy Filter

A consequence of sequential data assimilation is that there is a jump from the background mean to the analysis mean at the assimilation instant[3]. Then, the jumps from background to analysis can be depicted in the following way:

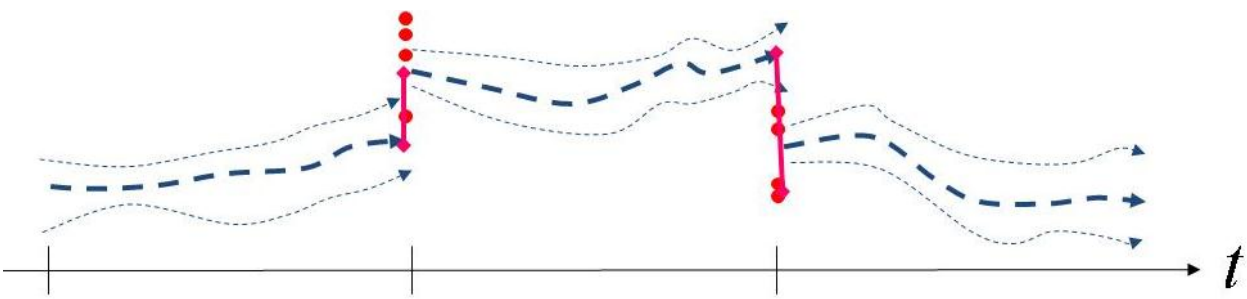

Figure 7. Schematic depicting the jump from background mean to analysis mean in sequential data assimilation. The bold dashed line depict the background/analysis mean, the red dots are observations, and the pink lines represent the jump from background mean to analysis mean when the assimilation is performed.

These jumps can have adverse consequences for some dynamical systems, especially for those containing balance relationships among variables (e.g., the geostrophic balance in an atmospheric model or in a shallow water equations system), since they can excite waves. Attempts have been made to distribute the impact of observations over finite time periods to generate a smooth transition from background mean to analysis mean. An example is the Incremental Analysis Update (IAU) from Bloom *et al.*, 1996.

[3] For the sake of this discussion, let us consider that the assimilation is performed every time an observation is available.

The EKBF for discrete observations discussed in section 2.5.1 is another framework to avoid these jumps. For the full ensemble $\overline{\overline{\mathbf{X}}}$, we can write the forecast and assimilation processes together in an ODE of the following form:

$$\frac{d\overline{\overline{\mathbf{X}}}}{dt} = f\left(\overline{\overline{\mathbf{X}}}\right) + \sum A\left(\overline{\overline{\mathbf{X}}}\right)\delta\left(t - t_{assim}\right) \tag{37}$$

Where $A\left(\overline{\overline{\mathbf{X}}}\right)$ represents the right-hand side of equation (33) and δ is the Dirac delta centered in the each assimilation instant. Bergemman and Reich (2011a) propose a method to extend the impact of the observations into a finite time interval by mollifying the Dirac delta functions. Schematically, this process is presented in the following figure:

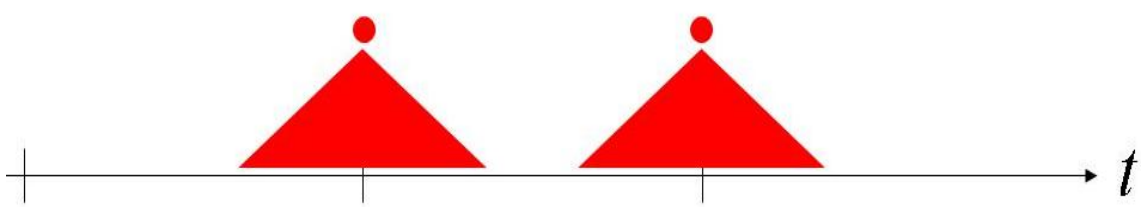

Figure 8. In order to create a smoother transition from background to analysis, the impact of the observation (red dot) can be extended into a finite time interval, represented by the base of the red triangles. The height of the triangle represents the relative importance given to the observation in this interval. This can be achieved in the EKBF by a mollification of the Dirac delta function.

Using a slow-fast extension of the Lorenz 1996 model with an intrinsic balance, Bergemman and Reich (2011a) showed that this mollified EKBF helps to avoid the loss of balance that would occur using a regular stochastic EnKF (see their figure 4). Before applying the mollified EKBF in more complicated systems, one would want to guarantee the robustness of the EKBF. This is the main purpose of this chapter: to analyze the behavior of the ODEs involved in the EKBF with respect to observational frequency, the

nonlinearity of the model, etc. It will be shown that these ODES suffer from stiffness under certain conditions, so that a robust and efficient integration scheme must be developed for their solution.

On the other hand, transform-based EnSRFs are efficient implementations since they perform most of the assimilation operations in the ensemble space rather than in the state space. Moreover, many implementation tools have been developed for transform-based EnSRFs, in particular the LETKF. These include an efficient R-localization and gridpoint adaptive multiplicative covariance inflation. To take advantage of these features, a transform alternative to the EKBF is developed; we call it Ensemble Transform Kalman-Bucy Filter (ETKBF).

This chapter is divided in three subsections. In the first section, the stiffening issue of the EnKBF is explained and a numerical integration scheme designed to tackle it is presented. In the second, the ETKBF is formulated and we provide a set of properties of this scheme that can make it advantageous. The third section presents experiments with different models; in particular, this section demonstrates that the ETKBF can be applied in atmospheric models.

3.1 Numerical integration in the EnKBF

An essential challenge in both formulations of the EnKBF (BGR09 and BR10) is to integrate the involved ODEs in pseudo-time in an efficient and affordable manner. In particular, the solution of these ODEs can present problems in the presence of nonlinear

perturbation growth resulting from infrequent observations (Kalnay *et al.*, 2007; Yang and Kalnay, 2009a). The nonlinear growth undermines the performance of EnKF since it violates the assumption that Gaussian analysis perturbations remain Gaussian after the forecast.

BGR09 used the Euler forward method (the simplest explicit integration method) with a variable number of steps. The optimal choice under their settings turned out to be 4, optimal in the sense that adding more steps did not translate in a further reduction of RMSE. In this section we show that the ODEs involved in the solution of BGR09 and BR10 stiffen under certain conditions, and that Euler forward is no longer an adequate choice for their solution.

Let us start the study of the ODEs in BGR09. To simplify, let us start our analysis with $\mathbf{R} = \sigma^2 \mathbf{I}$ and $\mathbf{H} = \mathbf{I}$, then equation (29) becomes:

$$\frac{d}{ds}\mathbf{X} = -\frac{1}{2\sigma^2(M-1)}\mathbf{X}\mathbf{X}^{\mathrm{T}}\mathbf{X} \tag{38}$$

This matrix ODE can be written down explicitly as:

$$\frac{d}{ds}\begin{bmatrix} x_1^{(1)} & x_2^{(1)} & \cdots & x_M^{(1)} \\ x_1^{(2)} & x_2^{(2)} & \cdots & x_M^{(2)} \\ \vdots & \vdots & \ddots & \vdots \\ x_1^{(N)} & x_2^{(N)} & \cdots & x_M^{(N)} \end{bmatrix} =$$

$$-\frac{1}{2\sigma^2(M-1)}\begin{bmatrix} \sum_{m=1}^{M}\left(x_m^{(1)}\sum_{n=1}^{N}x_1^{(n)}x_m^{(n)}\right) & \sum_{m=1}^{M}\left(x_m^{(1)}\sum_{n=1}^{N}x_2^{(n)}x_m^{(n)}\right) & \cdots & \sum_{m=1}^{M}\left(x_m^{(1)}\sum_{n=1}^{N}x_M^{(n)}x_m^{(n)}\right) \\ \sum_{m=1}^{M}\left(x_m^{(2)}\sum_{n=1}^{N}x_1^{(n)}x_m^{(n)}\right) & \sum_{m=1}^{M}\left(x_m^{(2)}\sum_{n=1}^{N}x_2^{(n)}x_m^{(n)}\right) & \cdots & \sum_{m=1}^{M}\left(x_m^{(2)}\sum_{n=1}^{N}x_M^{(n)}x_m^{(n)}\right) \\ \vdots & \vdots & \ddots & \vdots \\ \sum_{m=1}^{M}\left(x_m^{(N)}\sum_{n=1}^{N}x_1^{(n)}x_m^{(n)}\right) & \sum_{m=1}^{M}\left(x_m^{(N)}\sum_{n=1}^{N}x_2^{(n)}x_m^{(n)}\right) & \cdots & \sum_{m=1}^{M}\left(x_m^{(N)}\sum_{n=1}^{N}x_M^{(n)}x_m^{(n)}\right) \end{bmatrix} \quad (39)$$

This matrix differential equation is in fact a system of NM coupled ODEs; each ODE has NM 3rd order polynomial terms in the right hand side. Therefore, the best choice for numerical integration is an explicit method (as done in BGR09). Nonetheless, a deeper analysis reveals that the BGR09 ODEs can become stiff depending on the relative ratio of $\mathbf{P}$ and $\mathbf{R}$. Two main controlling factors of this ratio are the frequency of observations and length of the assimilation window. When this ratio is large, (29) loses stability due to stiffening. This challenge is addressed using an improved, semi-implicit numerical integration method for the EnKBFs.

Consider the analytical solution of the Bucy equation for the covariance in pseudo-time (appendix A):

$$\mathbf{P}(s) = \mathbf{P}^b\left(\mathbf{H}^T\mathbf{R}^{-1}\mathbf{H}\mathbf{P}^b s + \mathbf{I}\right)^{-1} \quad (40)$$

For illustration purposes, let $\mathbf{H} = \mathbf{I}$ and consider the scalar case of the previous equation, i.e. $N = 1$. It is convenient to write this equation as the following fraction, which is the ratio of the covariance at any moment *s* in pseudo-time and the background covariance:

$$\frac{P_1(s)}{P_1^b} = \frac{1}{\beta s + 1} \tag{41}$$

In (41), $\beta = P_1^b / \sigma_1^2$ represents the ratio of background error covariance to observational error covariance (variance, in this scalar example). The behavior of equation (41) depends upon the magnitude of this ratio as illustrated in the following figure:

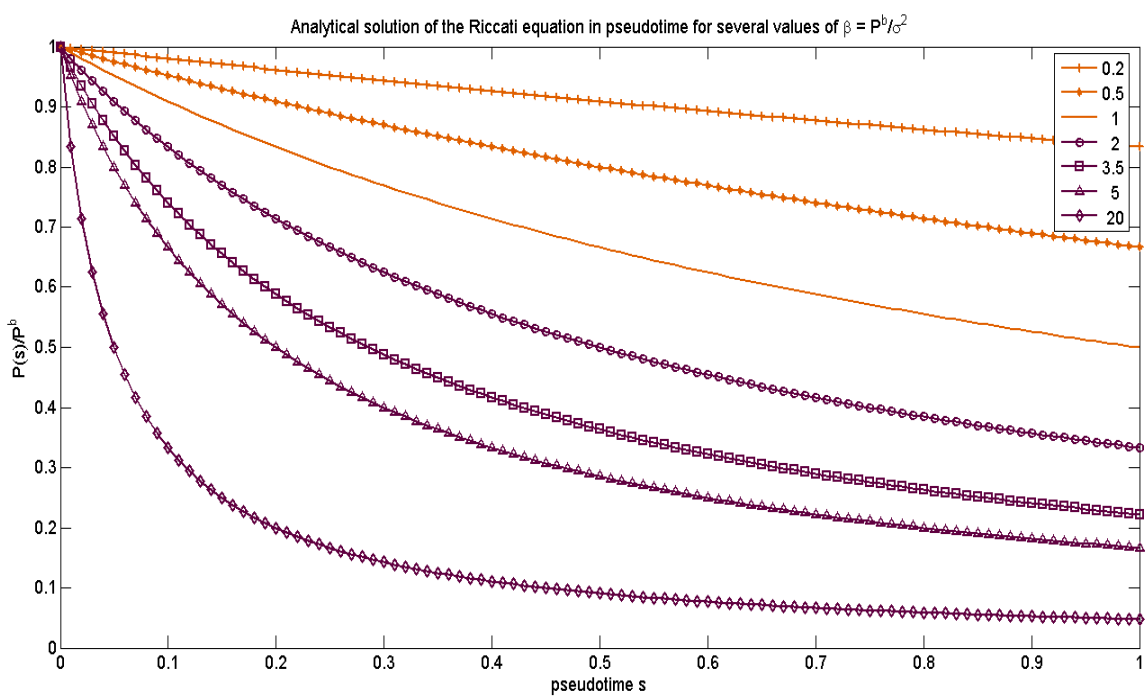

Figure 9. Analytical solution of the Bucy covariance equation in pseudo-time for a scalar case with the variable observed directly. Different lines correspond to different values ratio of background variance over observational error variance (see the legend). Two colors distinguish lines at different sides of the threshold of $\beta = 1$. The ODE stiffens as this ratio becomes larger.

The McLaurin expansion of (41) with respect to βs is:

$$\frac{P_1(s)}{P_1^b} = \sum_{ii=0}^{\infty} (-\beta s)^i = 1 - \beta s + (\beta s)^2 \ldots \tag{42}$$

It is clear then that for small values of β ($\beta < 1$, represented in the upper-right curves in figure 7), we have $P_1(s)/P_1^b \approx 1 - \beta s$, i.e. the function behaves close to linear. It is possible to get an accurate numerical approximation of these curves with the Euler forward method and using few steps. Nonetheless, for large values of β ($\beta > 1$, represented by the lower-left curves in figure 7), the solution becomes increasingly stiff and an explicit method such as Euler forward is no longer effective without significantly increasing the number of steps.

Returning to the general multivariate case with an arbitrary $\mathbf{H}$, the expression for β becomes:

$$\beta = \frac{\left| \mathbf{Y}^{b^T} \mathbf{R}^{-1} \mathbf{Y}^b \right|}{M - 1} \tag{43}$$

where $|\ |$ denotes the spectral matrix norm (maximum singular value). $\mathbf{P}^b$ and therefore β depend on the length of the forecast window. For short enough windows, $\mathbf{P}^b$ remains smaller than the observational error covariance $\mathbf{R}$ (hence $\beta < 1$), while for long windows it can become considerably larger (hence $\beta > 1$). As an illustration, we consider an assimilation experiment using LETKF and the Lorenz 1963 model for both frequent observations (β_s) and infrequent observations (β_l) windows (defined as

observing every 8 or 25 steps respectively; the details are explained in section 3.4.1). The empirical cumulative distribution functions (ECDF) of β_s and β_l are shown in the following figure:

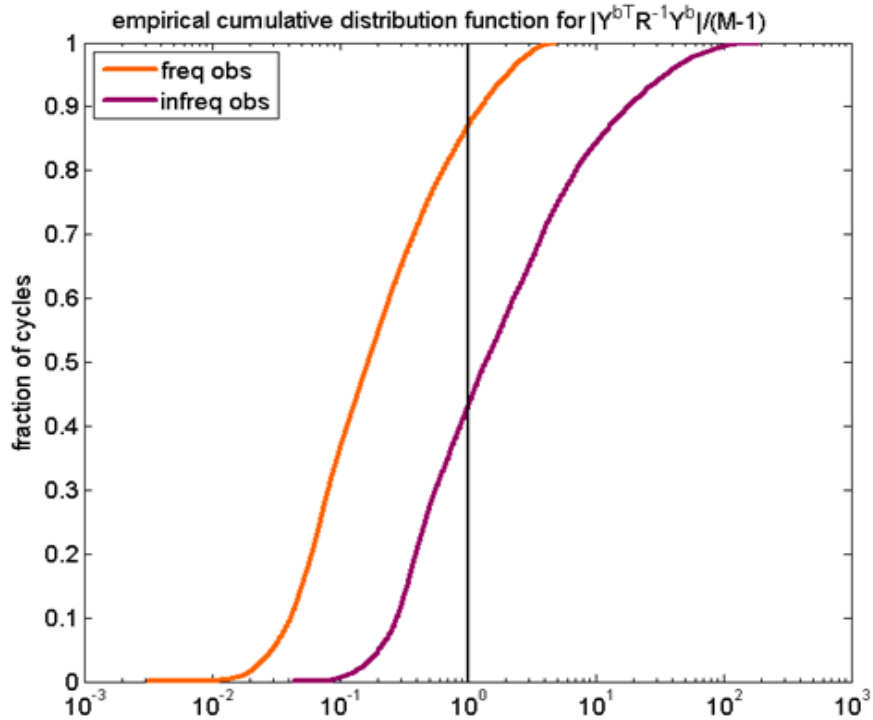

Figure 10. Empirical cumulative distribution function of $\beta = \left|\mathbf{Y}^{b^T}\mathbf{R}^{-1}\mathbf{Y}^b\right| \Big/ (M-1)$ for short (orange line) and long (purple line) assimilation windows using the Lorenz 1963 model. The value of this ratio for infrequent observations is in general an order of magnitude larger than for frequent observations.

From this figure we see that the ECDF for β_s is an order of magnitude to the smaller than the one for β_l. For short windows $\beta_s < 10^{-1}$ occurs about 45% of the cycles, and $\beta_s > 1$ only 15% (in fact $\max(\beta_s) = 4.81$). By contrast, for long windows $\beta_l < 10^{-1}$ only 1% of the times, $\beta_l > 1$ for about 60% of the cases, and $\max(\beta_l) = 187.07$. Hence, for the latter case the ODEs involved in the Bucy-type formulations are bound to stiffen.

We develop a Diagonal Semi-Implicit (DSI) method to overcome this stiffness. For convenience, let us recall the ODE for BGR09 (29):

$$\frac{d\mathbf{X}}{ds} = -\frac{1}{2}\mathbf{P}\mathbf{H}^T\mathbf{R}^{-1}\mathbf{H}\mathbf{X}$$

where $\mathbf{P} = \frac{\mathbf{X}\mathbf{X}^T}{M-1}$. A linearly[4] semi-implicit solution of this equation is:

$$\frac{\mathbf{X}_{k+1} - \mathbf{X}_k}{\Delta s} = -\frac{1}{2}\left(\alpha\mathbf{P}_k\mathbf{H}^T\mathbf{R}^{-1}\mathbf{H}\mathbf{X}_k + (1-\alpha)\mathbf{P}_k\mathbf{H}^T\mathbf{R}^{-1}\mathbf{H}\mathbf{X}_{k+1}\right) \tag{44}$$

Solving for $\mathbf{X}_{k+1}$ we obtain:

$$\mathbf{X}_{k+1} = \left(\mathbf{I} + \frac{(1-\alpha)\Delta s}{2}\mathbf{P}_k\mathbf{H}^T\mathbf{R}^{-1}\mathbf{H}\right)^{-1}\left(\mathbf{I} - \frac{\alpha\Delta s}{2}\mathbf{P}_k\mathbf{H}^T\mathbf{R}^{-1}\mathbf{H}\right)\mathbf{X}_k \tag{45}$$

Using the Sherman-Morrison-Woodbury lemma for the first factor in the rhs of the last equation:

$$\left(\mathbf{I} + \frac{(1-\alpha)\Delta s}{2}\mathbf{P}_k\mathbf{H}^T\mathbf{R}^{-1}\mathbf{H}\right)^{-1} = \mathbf{I} - \frac{(1-\alpha)\Delta s}{2}\mathbf{P}_k\mathbf{H}^T\left(\mathbf{R} + \frac{(1-\alpha)\Delta s}{2}\mathbf{H}\mathbf{P}_k\mathbf{H}^T\right)^{-1}\mathbf{H}$$

Then this becomes:

$$\mathbf{X}_{k+1} = \left(\mathbf{I} - \frac{(1-\alpha)\Delta s}{2}\mathbf{P}_k\mathbf{H}^T\left(\mathbf{R} + \frac{(1-\alpha)\Delta s}{2}\mathbf{H}\mathbf{P}_k\mathbf{H}^T\right)^{-1}\mathbf{H}\right)\left(\mathbf{I} - \frac{\alpha\Delta s}{2}\mathbf{P}_k\mathbf{H}^T\mathbf{R}^{-1}\mathbf{H}\right)\mathbf{X}_k \tag{46}$$

[4] It is linear since the quadratic term $\mathbf{P} = \mathbf{X}\mathbf{X}^{\mathbf{T}}$ is only evaluated in the instant k.

Letting $\alpha = 1$, we recover the Euler forward solution used in BGR09:

$$\mathbf{X}_{k+1} = \left(\mathbf{I} - \frac{\alpha \Delta s}{2} \mathbf{P}_k \mathbf{H}^T \mathbf{R}^{-1} \mathbf{H} \right) \mathbf{X}_k \tag{47}$$

On the other hand, letting $\alpha = 0$ leads to the linearly-implicit Euler scheme[5]:

$$\mathbf{X}_{k+1} = \mathbf{X}_k - \frac{\Delta s}{2} \mathbf{P}_k \mathbf{H}^T \left(\mathbf{I} + \frac{\Delta s}{2} \mathbf{H} \mathbf{P}_k \mathbf{H}^T \mathbf{R}^{-1} \right)^{-1} \mathbf{R}^{-1} \mathbf{H} \mathbf{X}_k \tag{48}$$

This scheme, however, can become excessively damping (i.e. $\mathbf{X}_{k+1} \to \mathbf{0}$) in the case $\Delta s \mathbf{P}_k >> \mathbf{R}$. Finally, if we let $\alpha = -1$ we obtain the following semi-implicit scheme:

$$\mathbf{X}_{k+1} = \mathbf{X}_k - \frac{\Delta s}{2} \mathbf{P}_k \mathbf{H}^T \left(\mathbf{I} + \Delta s \mathbf{H} \mathbf{P}_k \mathbf{H}^T \mathbf{R}^{-1} \right)^{-1} \mathbf{R}^{-1} \mathbf{H} \mathbf{X}_k \tag{49}$$

This scheme has the convenient property that $\mathbf{X}_{k+1} \to 1/2\, \mathbf{X}_k$ when $\Delta s \mathbf{P}_k >> \mathbf{R}$. Furthermore, to avoid computational burden, we substitute this equation by its diagonally semi-implicit (DSI) approximation:

$$\boxed{\mathbf{X}_{k+1} = \mathbf{X}_k - \frac{\Delta s}{2} \mathbf{P}_k \mathbf{H}^T \left(diag\left(\mathbf{I} + \Delta s \mathbf{H} \mathbf{P}_k \mathbf{H}^T \mathbf{R}^{-1} \right) \right)^{-1} \mathbf{R}^{-1} \mathbf{H} \mathbf{X}_k} \tag{50}$$

The inversion introduced is performed on a diagonal matrix and adds a negligible cost compared to the Euler forward method. In fact it does not change the order of accuracy of the Euler forward approximation (Hairer and Wanner, 1991). It does improve, however,

[5] Note that a regular implicit scheme would not suffer from this.

the stability and hence it is useful when the step size Δs is restricted by the method's stability rather than the accuracy.

The resulting update for the ensemble mean is:

$$\bar{\mathbf{x}}_{k+1} = \bar{\mathbf{x}}_k - \Delta s \mathbf{P}_k \mathbf{H}^T \left(diag\left(\mathbf{H}\mathbf{P}_k \mathbf{H}^T \mathbf{R}^{-1} \Delta s + \mathbf{I} \right) \right)^{-1} \mathbf{R}^{-1} \left[\mathbf{H}\bar{\mathbf{x}}_k - \mathbf{y} \right] \tag{51}$$

Finally, the DSI scheme of BR10 given by (33) is given by:

$$\boxed{\bar{\bar{\mathbf{X}}}_{k+1} = \bar{\bar{\mathbf{X}}}_k - \frac{\Delta s}{2} \mathbf{P}_k \mathbf{H}^T \left(diag\left(\mathbf{H}\mathbf{P}_k \mathbf{H}^T \mathbf{R}^{-1} \Delta s + \mathbf{I} \right) \right)^{-1} \mathbf{R}^{-1} \left[\mathbf{H}\bar{\bar{\mathbf{X}}}_k \left(\mathbf{I} + \mathbf{U} \right) - 2\mathbf{y}\mathbf{1}^T \right]} \tag{52}$$

The DSI method of (52) falls into the category of Rosenbrock methods with inexact Jacobian; it is also called the W methods in Hairer and Wanner (1991). Moreover, this method can handle non-diagonal $\mathbf{R}$.

To complement the DSI method, we choose a sequence of pseudo-time steps with increasing size that sum to one. For example a sequence of 7 steps will be {1/16,1/16,1/8,1/4,1/4,1/4}, a sequence of 8 steps will be {1/32,1/32,1/16,1/8,1/4,1/4,1/4} and so forth. The rationale behind this stepping is that the fastest change of equations (29) and (33) occurs at the beginning of pseudo-time, just around $s = 1/\beta$, so shorter steps are required there. This is illustrated in the following figure:

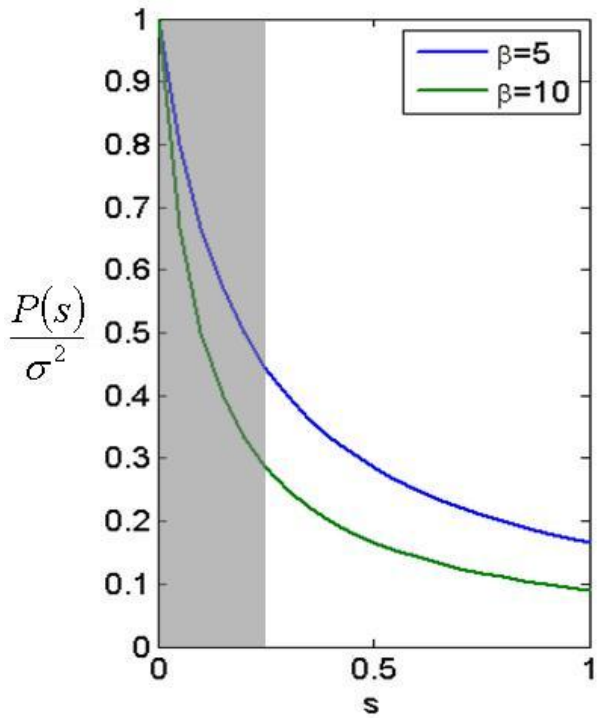

Figure 11. Analytical solution of the Kalman-Bucy equation for covariance in pseudo-time. For large values of β more resolution is needed at the beginning of the window (shaded region).

3.2. Transform-based alternatives for the EnKBF[6]

In the EnKBF formulations presented in BGR09 and BR10 some of the operations are performed in the state space and some are performed in the observation space. In an ensemble-transform approach, the analysis ensemble of perturbations is obtained as a product of the background ensemble of perturbations $\mathbf{X} \in \Re^{N \times M}$ in the model space and a matrix of weights in the ensemble space $\mathbf{W} \in \Re^{M \times M}$, i.e. $\mathbf{X}^a = \mathbf{X}^b \mathbf{W}^a$. This approach leads to the Ensemble Transform KF (ETKF; Bishop *et al*, 2001; Wang *et al*, 2004), the Local Ensemble Kalman Filter (Ott *et al*, 2004) and the Local ETKF (LETKF: Hunt *et al*, 2007). By incorporating the ensemble-transform approach, we develop two EnKF

[6] Professor Kayo Ide is kindly acknowledged for her idea to propose this alternative formulation.

methods that are stemmed from BGR09 and BR10 and refer to them as the Ensemble Transform KBFs (ETKBFs).

Working in the ensemble space can have several advantages. To begin with, the ensemble space $\Re^M$ is usually spanned in lower in dimensions than the state space $\Re^N$. If the majority of the operations are performed in this lower-dimensional space this can lead to computational savings and efficiency.

Another important feature is related with implementation aspects. Most practical data assimilation systems need two basic algorithms, localization and inflation, to attain successful performance. When the ensemble size is much smaller than the dimension of the model state ($M << N$), and more importantly smaller than the number of the positive Lyapunov exponents, straightforward application of any EnKF may lead to unreliable correlation estimations especially at long distance. The gridpoint **R**-localization (Hunt *et al*, 2007, Greybush *et al.*, 2011) is a simple yet powerful technique to handle this challenge for the EnKFs with the ensemble-transform approach. Underestimation of the background ensemble perturbation may also occur due to small *M* and other sources of imperfection. A common solution to overcome this problem is the use of multiplicative covariance inflation (Anderson and Anderson, 1999), in which the background ensemble covariance is multiplied by a factor larger than one. Usually, the search for an optimal inflation parameter is an ad-hoc tuning process, which can be time-consuming. Nonetheless, for the EnKFs with the ensemble-transform approach, an adaptive inflation scheme (Miyoshi, 2011) addresses this issue; this powerful scheme is tailored to **R**-

localization and provides an independent inflation parameter for each gridpoint of the model, each inflation parameter evolves with time.

In addition, having the weights available in the ensemble space, one can design a variety of schemes to improve the EnKF performance at no or very little cost; for example, the low-cost post-processing techniques such as accurate low-resolution analyses by weight interpolation (Yang *et al.*, 2009a), a no-cost smoother (Kalnay *et al*, 2007b), forecast sensitivity to observations without adjoint model (Liu and Kalnay, 2008, Li et *al*., 2009), and Running in Place/Quasi Outer-Loop (Kalnay and Yang, 2010; Yang and Kalnay, 2009). These techniques rely on the fact that the weights at the analysis time are valid through the entire forecast window (Kalnay *et al*, 2007b, Yang and Kalnay, 2009). These techniques have been shown to work effectively for data sparse situations that give rise to nonlinear perturbations (Kalnay and Yang, 2010; Yang *et al*, 2009).

In this section we develop two formulations: the transform-based alternative to BGR09 is denominated the Ensemble Transform Kalman-Bucy Filter (ETKBF), while the transform based alternative to BR10 is denominated Direct Ensemble Transform Kalman-Bucy Filter (ETKBF).

Derivation of ETKBF

For ETKBF, starting from BGR09 (29) and using the representation $\mathbf{X}(s) = \mathbf{X}^b\mathbf{W}(s)$, one can write:

$$\frac{d}{ds}\mathbf{X}^b\mathbf{W}(s) = -\frac{1}{2(M-1)}\mathbf{X}^b\mathbf{W}(s)\left(\mathbf{X}^{\mathbf{b}}\mathbf{W}(s)\right)^T\mathbf{H}^T\mathbf{R}^{-1}\mathbf{H}\mathbf{X}^b\mathbf{W}(s)$$

Recalling the mapping $\mathbf{Y}^b = \mathbf{H}\mathbf{X}^{\mathbf{b}}$ and simplifying the previous expression allows us to get the update analysis equation for ETKBF:

$$\boxed{\frac{d\mathbf{W}}{ds} = -\frac{1}{2(M-1)}\mathbf{W}\mathbf{W}^T\mathbf{Y}^{b^T}\mathbf{R}^{-1}\mathbf{Y}^b\mathbf{W}} \tag{53}$$

Solving this equation in pseudo-time s over $0 \le s \le 1$ with the initial condition $\mathbf{W}(0) = \mathbf{I}$, we obtain the analysis weight matrix $\mathbf{W}^a = \mathbf{W}(1)$ at $s = 1$. The ensemble mean is updated using equation (24).

For the numerical integration, the corresponding Euler forward scheme yields:

$$\mathbf{W}_{k+1} = \mathbf{W}_k - \frac{\Delta s}{2}\tilde{\mathbf{P}}_k\mathbf{Y}^{b^T}\mathbf{R}^{-1}\mathbf{Y}^b\mathbf{W}_k \tag{54}$$

where $\tilde{\mathbf{P}}_k = (M-1)^{-1}\mathbf{W}_k\mathbf{W}_k^{\ T}$ is the covariance in the ensemble space. The corresponding DSI integration scheme is:

$$\boxed{\mathbf{W}_{k+1} = \mathbf{W}_k - \frac{\Delta s}{2}\tilde{\mathbf{P}}_k\mathbf{Y}^{b^T} diag\left(\mathbf{I} + \Delta s\mathbf{Y}^b\tilde{\mathbf{P}}_k\mathbf{Y}^{b^T}\mathbf{R}^{-1}\right)^{-1}\mathbf{R}^{-1}\mathbf{Y}^b\mathbf{W}_k} \tag{55}$$

It can be shown that in the limit of infinite steps, the ETKBF is numerically equivalent to the LETKF (Hunt *et al.*, 2007). To proceed, we start by writing the expressing the covariance in ensemble space for any instant in pseudo-time:

$$\tilde{\mathbf{P}}(s) = \frac{\mathbf{W}(s)\mathbf{W}^T(s)}{M-1} \tag{56}$$

with $\tilde{\mathbf{P}}(0)=\tilde{\mathbf{P}}^b=(M-1)^{-1}\mathbf{I}$ and $\tilde{\mathbf{P}}(0)=\tilde{\mathbf{P}}^a$. Using the chain rule, we can find the pseudo-time derivate of this expression and perform simplifications:

$$\frac{d}{ds}\tilde{\mathbf{P}}(s)=\frac{2}{M-1}\left(\frac{d}{ds}\mathbf{W}(s)\right)\mathbf{W}^T(s)=\frac{2}{M-1}\left(-\frac{1}{2(M-1)}\mathbf{W}(s)\mathbf{W}^T(s)\mathbf{Y}^{b^T}\mathbf{R}^{-1}\mathbf{Y}^b\mathbf{W}(s)\right)\mathbf{W}^T(s)$$

Hence,

$$\frac{d}{ds}\tilde{\mathbf{P}}=-\frac{\mathbf{W}\mathbf{W}^T}{M-1}\mathbf{Y}^{b^T}\mathbf{R}^{-1}\mathbf{Y}^b\frac{\mathbf{W}\mathbf{W}^T}{M-1}=-\tilde{\mathbf{P}}\mathbf{Y}^{b^T}\mathbf{R}^{-1}\mathbf{Y}^b\tilde{\mathbf{P}} \tag{57}$$

The analytical solution to this Riccati equation is (appendix A):

$$\tilde{\mathbf{P}}(s)=\tilde{\mathbf{P}}(0)\left(\mathbf{Y}^{b^T}\mathbf{R}^{-1}\mathbf{Y}^b\tilde{\mathbf{P}}(0)s+\mathbf{I}\right)^{-1}=\frac{\mathbf{I}}{M-1}\left(\mathbf{Y}^{b^T}\mathbf{R}^{-1}\mathbf{Y}^b\frac{s}{M-1}+\mathbf{I}\right)^{-1}$$

$$\tilde{\mathbf{P}}(s)=\left(\mathbf{Y}^{b^T}\mathbf{R}^{-1}\mathbf{Y}^b s+(M-1)\mathbf{I}\right)^{-1} \tag{58}$$

In particular, for $s=1$ we get the same expression as for the LETKF:

$$\tilde{\mathbf{P}}(1)=\tilde{\mathbf{P}}^a=\left(\mathbf{Y}^{b^T}\mathbf{R}^{-1}\mathbf{Y}^b+(M-1)\mathbf{I}\right)^{-1} \tag{59}$$

Derivation of DETKBF

For DETKBF, we let $\overline{\overline{\mathbf{W}}}\in\Re^{M\times M}$ transform the background ensemble into the analysis ensemble, i.e. $\overline{\overline{\mathbf{X}}}^a=\overline{\overline{\mathbf{X}}}^b\overline{\overline{\mathbf{W}}}^a$. We note that the full ensemble space matrix $\overline{\overline{\mathbf{W}}}$ is different from the perturbation matrix $\mathbf{W}$ of the ETKBF. Then, (33) can be written as:

$$\frac{d}{ds}\left(\overline{\overline{\mathbf{X}}}^{b}\overline{\overline{\mathbf{W}}}(s)\right)=-\frac{1}{2(M-1)}\overline{\overline{\mathbf{X}}}^{b}\overline{\overline{\mathbf{W}}}(s)[\mathbf{I}-\mathbf{U}]\left(\overline{\overline{\mathbf{X}}}^{b}\overline{\overline{\mathbf{W}}}(s)\right)^{T}\mathbf{H}^{T}\mathbf{R}^{-1}\left[\mathbf{H}\overline{\overline{\mathbf{X}}}^{b}\overline{\overline{\mathbf{W}}}(s)[\mathbf{I}+\mathbf{U}]-2\mathbf{y}\,\mathbf{1}^{T}\right]$$

After simplifying, the DETKBF obtain the analysis $\overline{\overline{\mathbf{W}}}$ by solving:

$$\boxed{\frac{d\overline{\overline{\mathbf{W}}}}{ds}=-\frac{1}{2(M-1)}\overline{\overline{\mathbf{W}}}(\mathbf{I}-\mathbf{U})\overline{\overline{\mathbf{W}}}^{T}\overline{\overline{\mathbf{Y}}}^{b^{T}}\mathbf{R}^{-1}\left[\overline{\overline{\mathbf{Y}}}^{b}\overline{\overline{\mathbf{W}}}(\mathbf{I}+\mathbf{U})-2\mathbf{y}\mathbf{1}^{T}\right]} \tag{60}$$

with the initial condition $\overline{\overline{\mathbf{W}}}(0)=\mathbf{I}$, where $\overline{\overline{\mathbf{Y}}}^{b}=\mathbf{H}\overline{\overline{\mathbf{X}}}^{b}$ is the mapping of the (full) background ensemble into observations space. At $s=1$, we obtain the analysis weight matrix $\overline{\overline{\mathbf{W}}}^{a}=\overline{\overline{\mathbf{W}}}(1)$. The corresponding Euler forward integration is:

$$\overline{\overline{\mathbf{W}}}_{k+1}=\overline{\overline{\mathbf{W}}}_{k}-\frac{\Delta s}{2}\tilde{\mathbf{P}}_{k}\overline{\overline{\mathbf{Y}}}^{b^{T}}\mathbf{R}^{-1}\left[\overline{\overline{\mathbf{Y}}}^{b}\overline{\overline{\mathbf{W}}}_{k}(\mathbf{I}+\mathbf{U})-2\mathbf{y}\,\mathbf{1}^{T}\right] \tag{61}$$

where $\tilde{\mathbf{P}}_{k}=(M-1)^{-1}\mathbf{W}_{k}\mathbf{W}_{k}^{T}=(M-1)^{-1}\overline{\overline{\mathbf{W}}}_{k}(\mathbf{I}-\mathbf{U})\overline{\overline{\mathbf{W}}}_{k}^{T}$. The corresponding DSI integration scheme is:

$$\boxed{\overline{\overline{\mathbf{W}}}_{k+1}=\overline{\overline{\mathbf{W}}}_{k}-\frac{\Delta s}{2}\tilde{\mathbf{P}}_{k}\overline{\overline{\mathbf{Y}}}^{b^{T}}\left(diag\left(\mathbf{I}+\Delta s\overline{\overline{\mathbf{Y}}}^{b}\tilde{\mathbf{P}}_{k}\overline{\overline{\mathbf{Y}}}^{b^{T}}\mathbf{R}^{-1}\right)\right)^{-1}\mathbf{R}^{-1}\left[\overline{\overline{\mathbf{Y}}}^{b}\overline{\overline{\mathbf{W}}}_{k}(\mathbf{I}+\mathbf{U})-2\mathbf{y}\,\mathbf{1}^{T}\right]} \tag{62}$$

3.3. Localization in the ETKBFs

A problem that is common to all EnKF formulations is the appearance of long distance spurious correlations as a result of the finite size of the ensemble (Hamill *et al.* 2001). Localization is a common solution to this problem. It is essential when the size of the

ensemble is smaller than the size of the state space, and more importantly, smaller than the number of positive Lyapunov exponents.

Different localization techniques can lead to different filter performance and behavior, for example in the conservation of balance (Greybush *et al.*, 2011). Within the EnKF framework, there are mainly two types of localizations: B-localization and R-localization. Roughly speaking, B-localization reduces the forecast (background) error covariance between a pair of grid points by a factor depending monotonically on the distance between them, while R-localization increases the observational error by the inverse of the same factor (see a more detailed discussion in Greybush *et al.*, 2011). In R-localization, an independent analysis is carried out for every single grid point using observations within a certain distance, and assuming that the observation error increases with the distance to the grid point. An schematic of this localization is presented next:

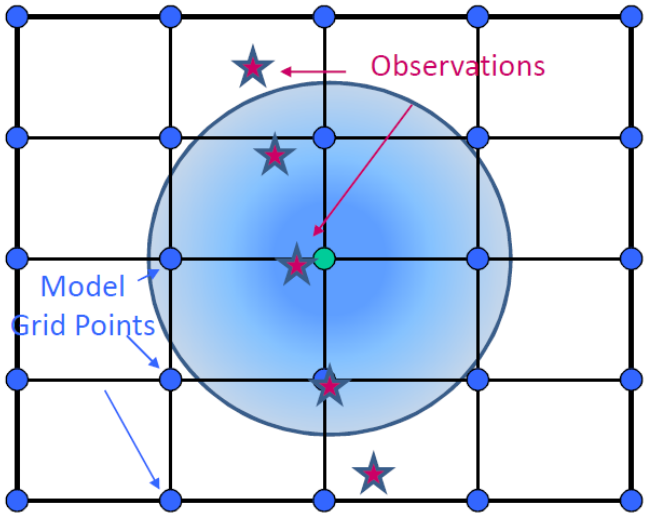

Figure 12. Schematic of R-localization (courtesy of Dr. Greybush).

In the previous figure, the gridpoints are shown with blue circles, the observations with pink starts. For a given gridpoint (shown in green, in the center), only observations within a radius of influence (shown as a large blue area with a color intensity decreasing radially) are used with a weighting that depends on the distance to the gridpoint. A commonly used compact support weighting function that approximates a Gaussian can be found in Gaspari and Cohn (1999).

BGR09 and BR10 are amenable to B-type localization. The localization matrix $\mathbf{C} \in \Re^{N \times L}$ is in fact applied to $\mathbf{PH}^T$, the elements of $\mathbf{C}$ depend upon the distance between observations and state variables. A localized version of BR10 can be written as:

$$\frac{d\overline{\overline{\mathbf{X}}}}{ds} = -\frac{1}{2}\left(\mathbf{C} \circ \left(\mathbf{PH}^T\right)\right)\mathbf{R}^{-1}\left[\mathbf{H}\overline{\overline{\mathbf{X}}}\left[\mathbf{I} + \mathbf{U}\right] - 2\mathbf{y}\mathbf{1}^T\right] \tag{63}$$

where the symbol $\circ$ indicates Schur (element-wise) product. In some of our experiments we will compare the performance of B-localized BR10 against that of R-localized ETKBFs. For both ETKBF and DETKBF a gridpoint R-localization can be implemented in a straightforward manner. We illustrate this procedure for DETKBF, but the same sequence of steps apply for ETKBF.

a) Compute the mapping of the global background ensemble into the observation space $\overline{\overline{\mathbf{Y}}}^b = \mathbf{H}\overline{\overline{\mathbf{X}}}^b$. This is the only global operation. For each gridpoint *i*, a local (denoted with the subindex $[l]$) subset of this mapping $\overline{\overline{\mathbf{Y}}}_{i[l]}^b$ along with a local subset of observations

$\mathbf{y}_{i[l]}$ are selected. These sets correspond to the observations in the physical region where the product $\mathbf{C}_i\mathbf{R}^{-1}$ is nonzero, where $\mathbf{C}_i$ is the localization matrix for the gridpoint *i*.

b) The rest of the operations are local, for greater efficiency steps (b) and (c) can be done in parallel. For the ith gridpoint, the Euler forward and DSI schemes can be written as:

$$\overline{\overline{\mathbf{W}}}_{k+1,i} = \overline{\overline{\mathbf{W}}}_{k,i} - \frac{\Delta s}{2}\tilde{\mathbf{P}}_{k,i}\,\overline{\overline{\mathbf{Y}}}^{b\,T}_{i[l]}\,\mathbf{C}_{i[l]}\mathbf{R}^{-1}_{i[l]}\left[\overline{\overline{\mathbf{Y}}}^{b}_{i[l]}\overline{\overline{\mathbf{W}}}_{k,i}\left[\mathbf{I}+\mathbf{U}\right]-2\mathbf{y}_{i[l]}\mathbf{1}^T\right] \tag{64}$$

$$\begin{aligned}\overline{\overline{\mathbf{W}}}_{k+1,i} = \overline{\overline{\mathbf{W}}}_{k,i} - \frac{\Delta s}{2}\tilde{\mathbf{P}}_{k,i}\,\overline{\overline{\mathbf{Y}}}^{b\,T}_{i[l]}\left(diag\left(\mathbf{I}+\Delta s\,\overline{\overline{\mathbf{Y}}}^{b}_{i[l]}\tilde{\mathbf{P}}_{k,i}\,\overline{\overline{\mathbf{Y}}}^{b\,T}_{i[l]}\,\mathbf{C}_{i[l]}\mathbf{R}^{-1}_{i[l]}\right)\right)^{-1}\times \\ \mathbf{C}_{i[l]}\mathbf{R}^{-1}_{i[l]}\left[\overline{\overline{\mathbf{Y}}}^{b}_{i[l]}\overline{\overline{\mathbf{W}}}_{k,i}\left[\mathbf{I}+\mathbf{U}\right]-2\mathbf{y}_{i[l]}\mathbf{1}^T\right]\end{aligned} \tag{65}$$

The matrices $\mathbf{C}_{i[l]}$ and $\mathbf{R}_{i[l]}$ are submatrices of $\mathbf{C}_i$ and $\mathbf{R}$ respectively.

c) After performing the integration to get $\overline{\overline{\mathbf{W}}}^{a}_{i}$, the analysis at that gridpoint is obtained as $\overline{\overline{\mathbf{X}}}^{a}_{i} = \overline{\overline{\mathbf{X}}}^{b}_{i}\,\overline{\overline{\mathbf{W}}}^{a}_{i}$. This matrix has size $\overline{\overline{\mathbf{X}}}^{b}_{i} \in \Re^{N_i \times M}$, where N_i is the number of state variables in said gridpoint.

The computational expense for R-localized DETKBF is estimated next. The local procedure in each one of the N gridpoints is $O\left(\max\left(L_{[l]}M^2, M^3\right)\right)$, where $L_{[l]}$ is the number of observations used for that location. Since each gridpoint is independent from the others, they can be processed in parallel. Nonetheless, as with the LETKF, an important aspect to ensure stability of this localization is to have significant overlap in the

observations used for the analysis in neighboring gridpoints. For a broader discussion on this issue the reader is referred to Hunt *et al.* (2007).

3.4. Experiments

Now we use the three models described in section 2.2 to test the ETKBF. The high nonlinearity of the Lorenz 1963 model will help to test the ability of the DSI integration method to handle stiffness. The Lorenz 1996 will allow us to test localization aspects, and in particular to see the interaction between different combinations of values for localization and multiplicative covariance inflation. The SPEEDY model will allow us to prove that these formulations can be used in a real life NWP setting.

3.4.1. Experiments with the 3-variable Lorenz 1963 model

We use settings similar to those of Kalnay *et al.* 2007 and Miller *et al.* 1994. An initial period of 1000 time steps in the nature run was discarded to ensure that it is on the model manifold. The "observations" are generated by adding a random term $N(\mathbf{0}, \mathbf{R} = 2\mathbf{I})$ to the nature run. All the variables are observed directly, i.e., $\mathbf{H} = \mathbf{I}$.

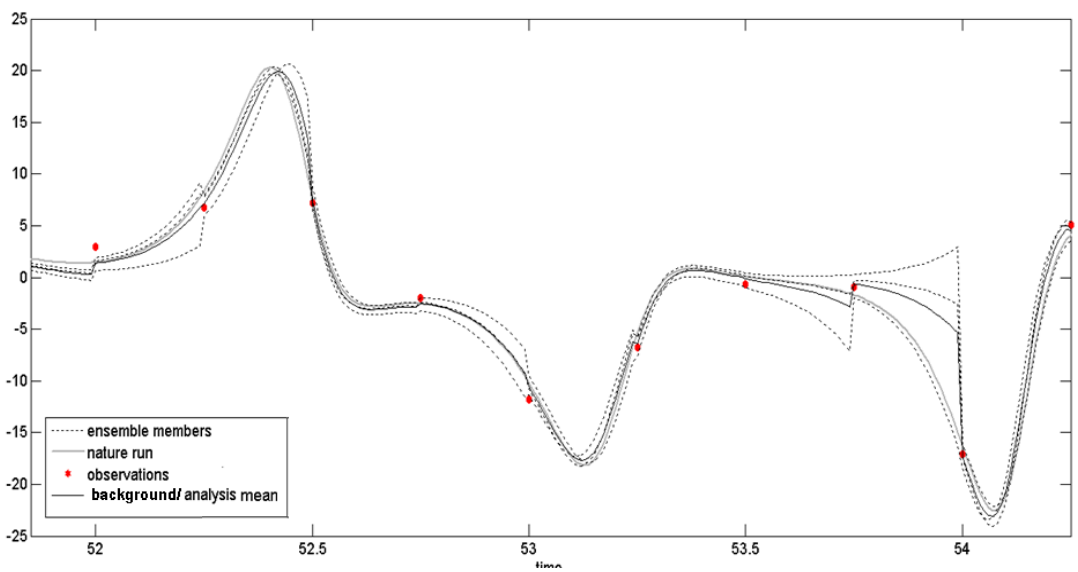

Figure 13. Example of the evolution and assimilation of $x^{(2)}$ in the infrequent observations case with LETKF. The true run, the observations and the analysis ensemble are shown.

Two cases are considered:

- "Frequent" observations. These are taken every 8 time steps and lead to short windows in which the perturbations grow essentially linearly; this roughly corresponds to a 6-hr assimilation cycle in an atmospheric global circulation model.
- "Infrequent" observations. These are taken at 25 time steps and lead to long assimilation windows in which perturbations grow nonlinearly and their distribution is no longer Gaussian; Kalman filtering becomes less accurate for this long case.

An ensemble of size $M = 3$ was used for the assimilation. It is a small size (e.g., Evensen, 1997 used over a thousand members for this model), but it emulates the fact that in atmospheric models the number of state variables is usually much larger than the number of ensemble members that is computationally feasible. The ensemble members are initialized by adding random noise to the truth with the same covariance as the observational error. Figure 10 illustrates the time evolution of one of the state variables; it illustrates the truth, the observations, and each one of the ensemble members. In this case, the original EnKBF formulations and our EnTKBF formulations are practically equivalent.

In order to optimize the performance of the filter (and avoid divergence in the infrequent observations case) we use multiplicative covariance inflation (Anderson and Anderson, 1999). Under this scheme, the background ensemble perturbation is multiplied by a factor $\mathbf{X}^b \to \mathbf{X}^b(1+\delta)$, with $\delta > 0$, equivalent to multiplying the background covariance matrix by $\mathbf{P}^b \to \mathbf{P}^b(1+\delta)^2$. For both frequent and infrequent observations, we examine the effect of different values of δ in the Bucy-type formulations as well as in the LETKF. In

addition to δ we also vary the number of pseudo-time steps in our experiments to achieve optimal performance. Due to the size and structure of the model, there is no need to apply localization.

Frequent observations

For the frequent observations case, the values of δ are taken from $0 \leq \delta \leq 0.15$ (in Kalnay *et al.*, 2007, the optimal value was found to be $\delta = 0.04$). First, we test the original EnKBF formulations with a variable number of steps in pseudo-time were used. We started using the Euler forward integration scheme; the results of these experiments are shown in figure 14 (a sample size of 125000 analysis cycles was used in this case).

For both BGR09 and BR10 it is found that using less than 3 steps for the integration leads to a poor performance. The filters started performing well with 3 steps, and with just 5 steps the performances of both EnKBFs converge to that of LETKF. The computing time was indistinguishable even with 6 steps in pseudo-time. The three formulations show similar behavior with respect to the inflation parameter. From $\delta = 0$ to about $\delta \approx 0.03$, the performance of the filter improves fast as inflation increases. After this value, there is an optimal performance region for the three filters. Beyond this region, the covariance inflation becomes excessive and the filter begins to lose skill slowly in an apparent linear way. The results coming from using the ETKBFs are identical.

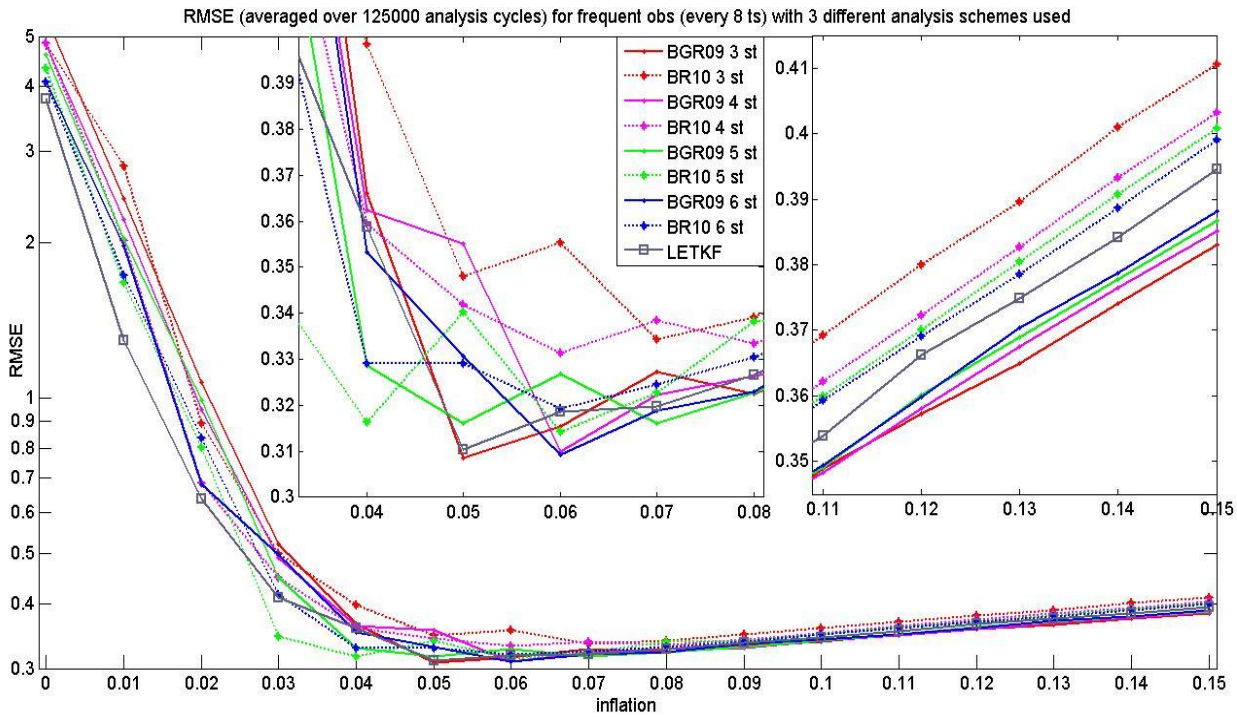

Figure 14. Analysis RMSE for LETKF and the two Bucy-based formulations in the case of frequent observations in the Lorenz 1963 model. The integration uses the EF method.

The experiments were repeated with the DSI integration method. No perceivable increase in computational time was detected. In order to produce smoother curves, the sample size was increased to 10^6 analysis cycles. The results of this experiment are presented in the following figure; in this case we depict the results using the ETKBFs. One can notice the almost perfect equivalence in the performance of LETKF and ETKBF and DETKBF with 5 steps in pseudo-time.

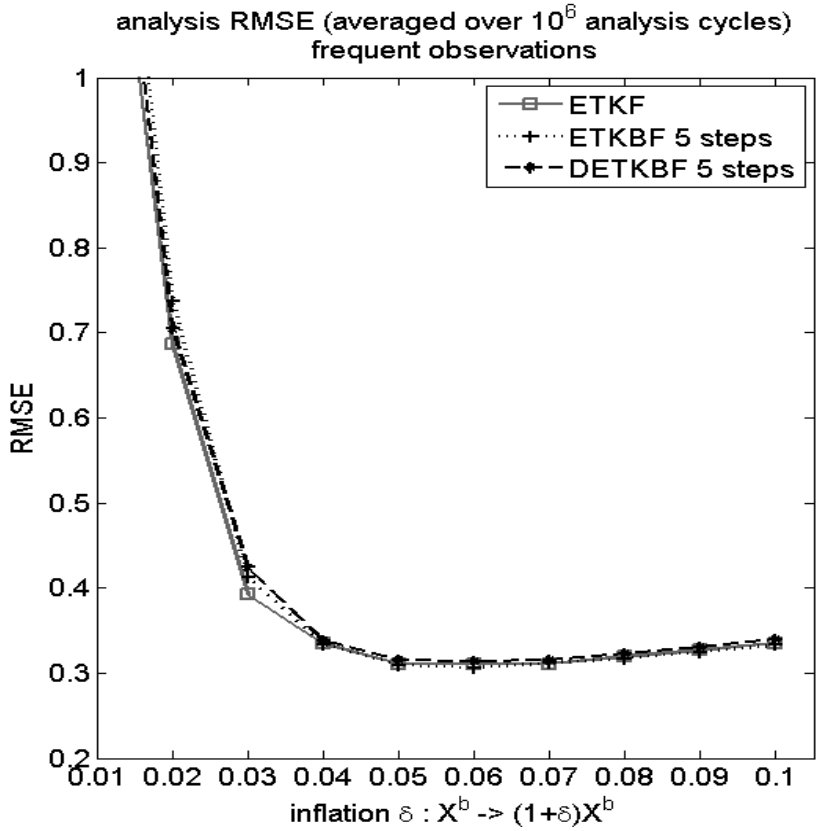

Figure 15. Analysis RMSE for LETKF and ETKBF and DETKBF with 5 steps in pseudo-time in the frequent observations case. The DSI integration method is used for the Bucy-type formulations.

Infrequent observations

For the infrequent observations case, inflation values are taken from $0 \le \delta \le 1$ (in Kalnay *et al.* 2007, the optimal inflation was $\delta = 0.39$). Again, we start by testing both original EnKBF formulations. Our first experiments use the Euler forward integration method. As expected from the analysis performed in section 3.1, stiffening occurrs and this scheme fails with a number of steps of $O(1-10)$. A large number of pseudo-time steps (~70 for BGR09 and ~300 for BR10) are necessary to achieve a performance similar to LETKF, and occasional failure is still observed. The next figure shows the slow convergence in

the case of BGR09 using EF with increasing number of steps in pseudo-time; this figure was produced using sample sizes of 40,000 analysis cycles.

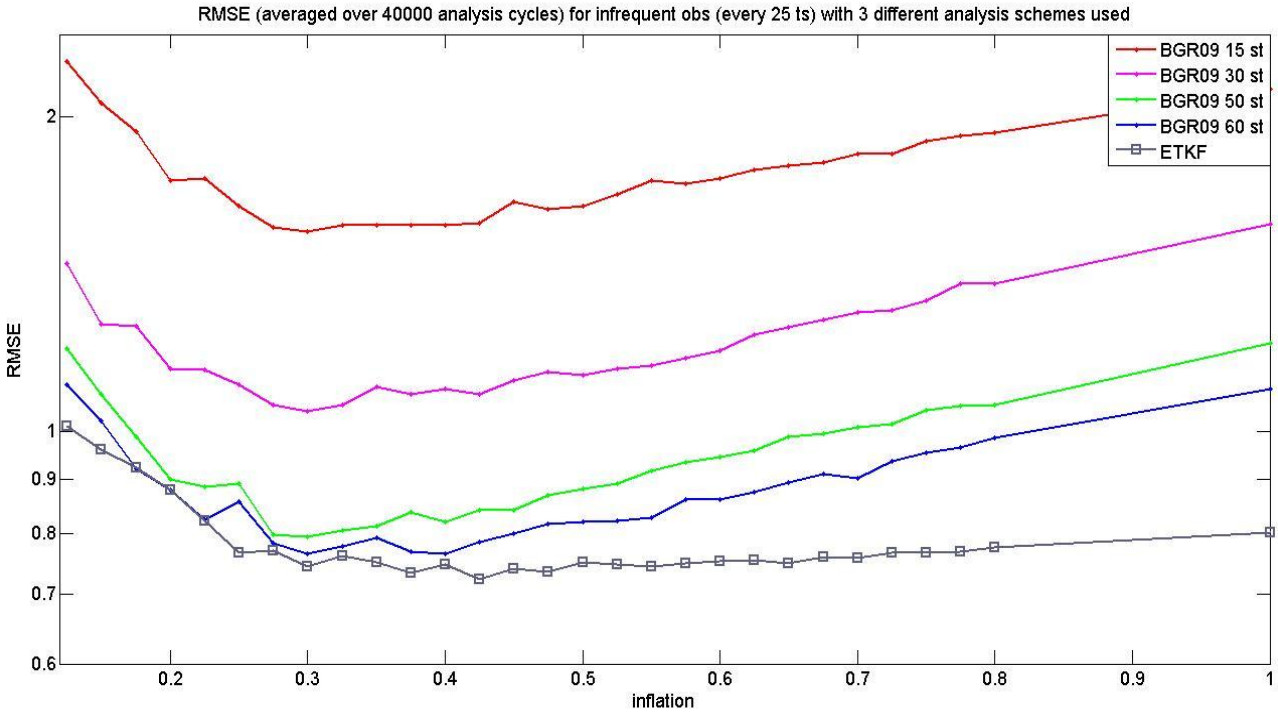

Figure 16. Analysis RMSE for LETKF and BGR09 in the case of infrequent observations in the Lorenz 1963 model. The integration uses the EF method.

We don't show the results for BR10 since constant filter failure does not allow producing smooth curves. The fact that BR10 presents more problems than BGR09 can be understood if we remember that for BR10 the observations participate in the update of both the analysis mean and the analysis ensemble of perturbations. Moreover, the update for the mean in BGR09 is linear while in BR10 it is not. Again, the experiments using the ETKBF formulations lead to the same conclusions.

We then switch to the DSI integration method, first using uniform pseudo-time steps. Under these settings we find that at least 30 steps are needed for BGR09 to achieve the performance of the LETKF and for BR10 we find that this number is ~50. Switching to the variable time stepping discussed at the end of section 3.1, we find a reduction of these numbers to 8.

In the next figure, we show the results of using the DSI scheme with variable time stepping with the ETKBF formulations. A sample size of 10^6 assimilation cycles is used. Again, for the 3 formulations a rapid reduction in RMSE is observed as one increases the value of inflation before $\delta \approx 0.3$; then an optimal inflation region is found.

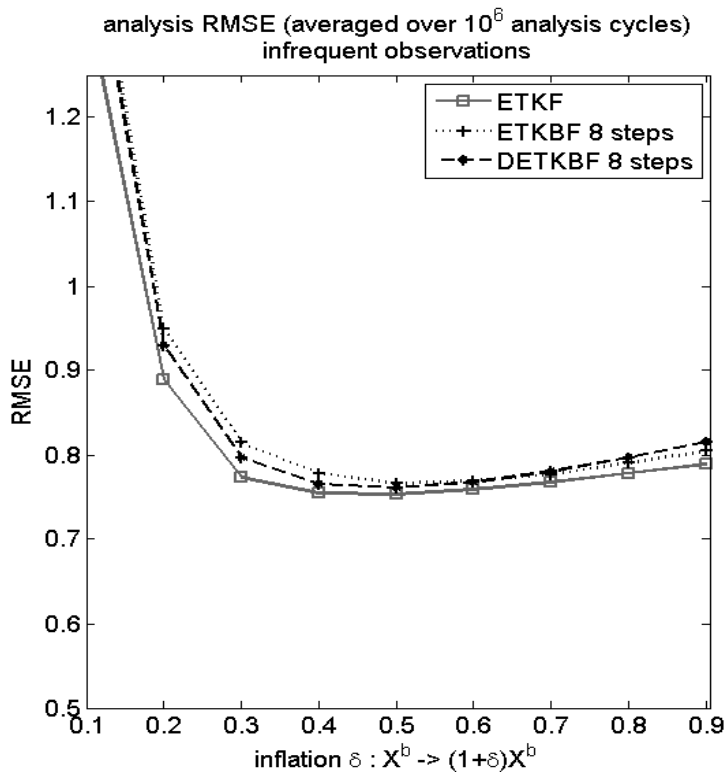

Figure 17. Analysis RMSE values (averaged over 10^6 assimilation cycles) for ETKF, ETKBF and DETKBF in L63 in the the infrequent observations case is shown. The Bucy-type formulations were integrated using the (DSI) method with 8 non-uniform steps.

Summary

The next table summarizes the lowest RMSE results for both frequent and infrequent observations using DSI integration with variable time stepping for the ETKBFs and a sample of 10^6 analysis cycles. The performance of the LETKF is also shown as reference. In the infrequent observations case, the lowest RMSE values are about 1% larger for both Bucy-based formulations than for LETKF but with comparable computing time.

	LETKF	ETKBF	DETKBF
Frequent observations	0.3108 ($\delta = 0.07$)	0.3064 ($\delta = 0.06$)	0.3163 ($\delta = 0.06$)
Infrequent observations	0.7544 ($\delta = 0.4$)	0.7664 ($\delta = 0.5$)	0.7612 ($\delta = 0.5$)

Table 1. Lowest RMSE values in the Lorenz 1963 model with frequent and infrequent observations using three filters. The optimal inflation value is indicated in parenthesis.

3.4.2. Experiments with the 40-variable Lorenz 1996 model

In this case, observations are taken every 2 time steps, i.e. in intervals of length $\Delta t = 0.05$. For L96 with $F = 8$ this is roughly equivalent to a 6 hours window in an atmospheric general circulation model (Lorenz and Emmanuel, 1998). We observe every other grid point with an observational error covariance $\mathbf{R} = \mathbf{I}$. An ensemble of $M = 10$ members is used for the experiments. The first 500 analysis cycles were discarded as a transient.

With these settings, localization is necessary to avoid filter divergence. First, we test the B-localized BR10 and the R-localized DETKBF schemes and compar their performance with that of the LETKF. Fixed multiplicative covariance inflation is used with inflation values taken from $0 \le \delta \le 0.125$. The values for the localization radius are taken from $1.5 \le \lambda \le 9$. The two integration schemes (EF and DSI with varying time steps) are tested with 3 to 6 integration steps.

For both integration schemes, the performance with 3 pseudo-time steps was comparable to that of the LETKF and after 4 steps we found only marginal improvements. Figure 18 shows the results of this experiment for the case of 4 steps; the performance of the 3 methods is shown as function of both multiplicative inflation and localization radius. B-localized BR10 corresponds to the left column, R-localized DETKBF corresponds to the center column and LETKF corresponds to the right column. The Bucy-based formulations were integrated using the DSI method. These results are computed from a sample of 10^5 analysis cycles. The top row of the figure shows the analysis RMSE; only

the RMSE values smaller than the observational error (equal to 1) are colored, but all the RMSE values obtained are finite and smaller than ~ 4.6. The bottom row shows the ratio of the average spread of the ensemble divided by the analysis RMSE; ideally the value should be close to 1.

The overall performance is quite similar among the 3 methods; the best RMSE values are within 1% of each other. In this case the computational time is not shown; the comparison is not straightforward –as in the non-localized case of L63- since it depends on details of the implementation, in particular if the gridpoints can be processes in parallel for the R-localized case. In general, for both integration schemes and different steps (not shown) the methods using gridpoint R-localization achieve their optimum for smaller localization radii than the B-localization. Similar findings were reported in the experiments performed by Greybush *et al.* 2011 with other models.

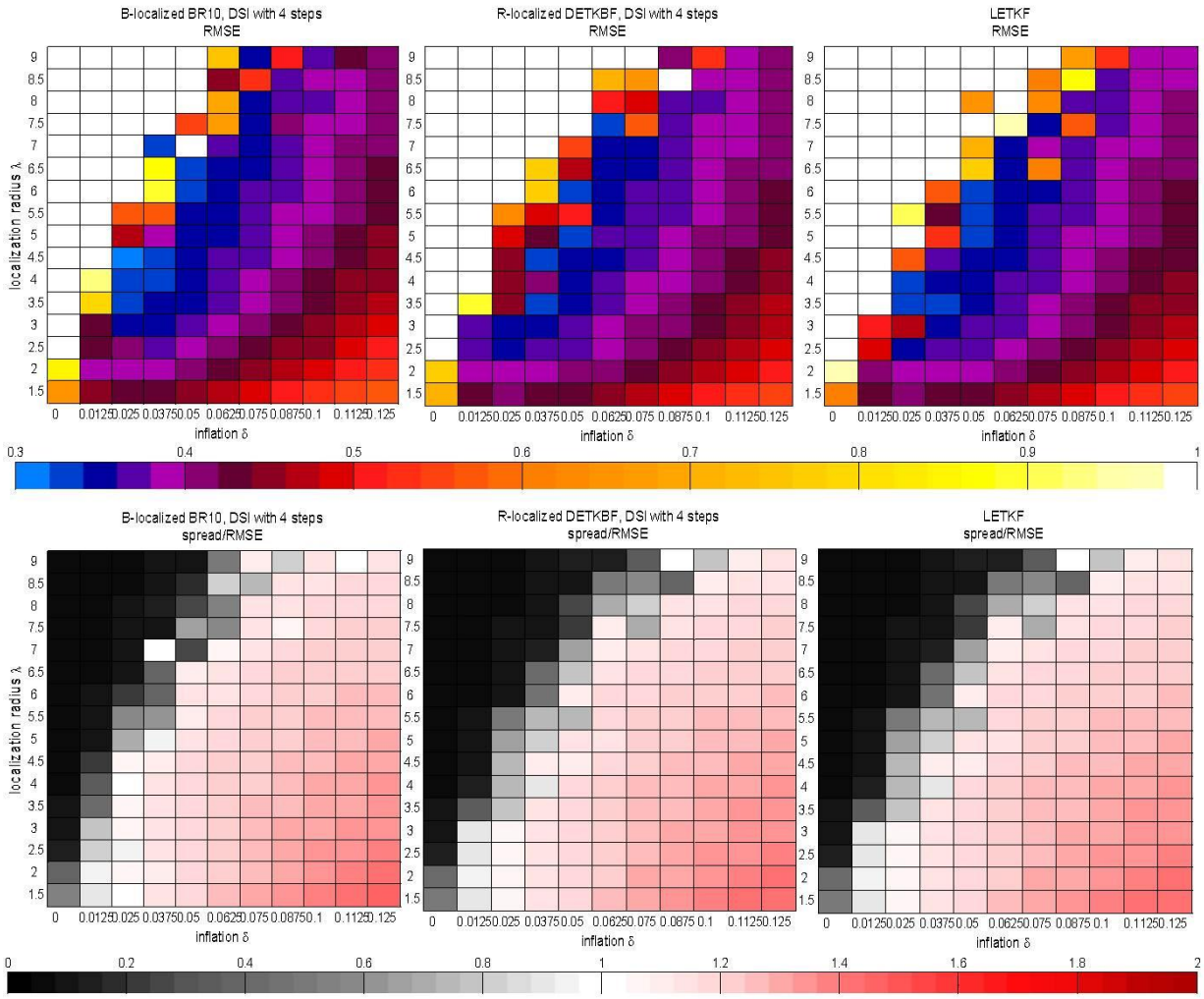

Figure 18. Filter performance for B-localized BR10 (left), R-localized DETKBF (center) and LETKF (right) in the L96; for the Bucy-type formulations the DSI integration scheme with 4 uniform steps is used. The effects of multiplicative inflation and localization radius are shown; each tile represents an average over 10^5 analysis cyles. The top row show the analysis RMSE, the uncolored tiles denote RMSE values larger than the observational error, but all the RMSE values were finite and < 4.6. The bottom row shows the ratio of the average ensemble spread divided by the analysis RMSE; ideally this ratio should be close to 1.

In the previous experiments, little difference was found between the two integration schemes. This is due to the following facts: (a) this model is slower than L63, (b) our settings correspond to a frequent assimilation scheme, and (c) the observation network is relatively dense. Nonetheless, the value of the DSI integration method becomes clear if

we consider the issue of initializing our background ensemble. If this initial ensemble is too far from the truth, using the Euler Forward integration often leads to failure. This fact can be illustrated with a simple experiment described next and illustrated in figure 19. The unstable steady state of the L96 system is $\mathbf{X}_j = F \ \forall j$. Hence a simple way to generate an initial ensemble is to add random perturbations to this steady state for each one of the $N = 40$ variables and $M = 10$ ensemble members. Using R-localized DETKBF with $\delta = 0.05$ and $\lambda = 5$, we generated initial ensembles using the observational error $\mathbf{R}$ (top panel), then $2\mathbf{R}$ (center panel) and $3\mathbf{R}$ (bottom panel) and let the forecast/analysis cycles evolve; the first 150 analysis cycles are shown. As the random perturbations of the initial ensemble decreases, using the Euler Forward method leads to very large analysis RMSE values in first cycles as the filter stabilizes. This does not happen with the DSI method. For even larger initial perturbations (not shown), the EF usually fails in the first analysis cycles.

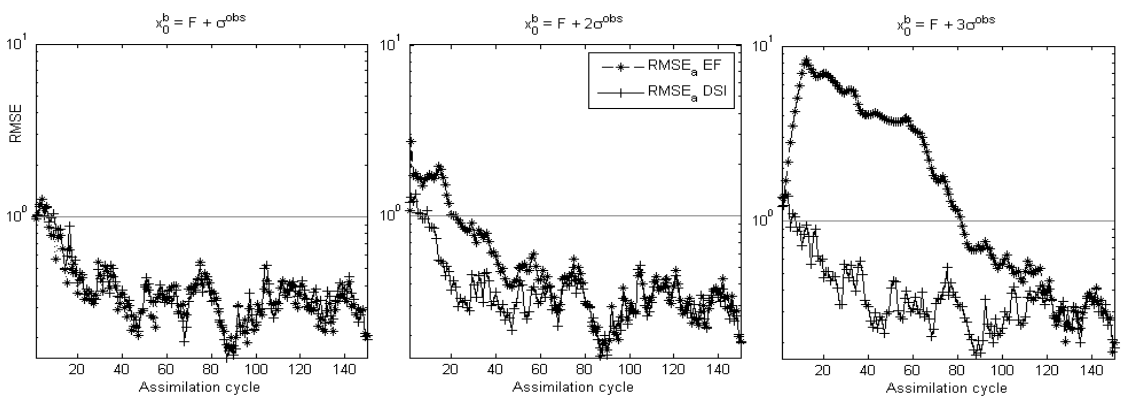

Figure 19. Analysis RMSE for the first 150 assimilation cycles of an experiment using L96 and R-localized DETKBF. The effect of the two integration schemes (Euler Forward and Diagonal Semi-Implicit) is shown for different initial ensembles. As the initial ensemble is more inaccurate (from left to right), EF takes longer to initialize the filter while DSI does not present problems.

So far, in the previous experiments we have manually tuned the multiplicative covariance inflation parameter δ, and its value has been fixed for all gridpoints and for all time. An attractive feature of R-localization is that gridpoint-by-gridpoint adaptive multiplicative covariance inflation can be implemented (Miyoshi, 2011). This scheme uses the diagnostic relationships of Desroziers *et al*, 2005. Besides avoiding the manual tuning of δ, it allows each gridpoint to have its own inflation which evolves with time.

In the next set of experiments, we use this scheme. We extend the sample size to 10^6 analysis cycles and, since we do not have to tune anything, we allow ourselves use two ensemble sizes: $M = \{10,15\}$. In table 1 we present the average analysis RMSE, the average analysis ensemble spread and the average (both in space and time) covariance inflation parameter. Each column corresponds to a different filter: LETKF, ETKBF and DETKBF (the latter two with 4 steps in pseudo-time), and each row corresponds to a different ensemble size. As expected the RMSE is smaller for the larger ensemble size (albeit by little). On the other hand, there is negligible difference in the performance of the three filters. The RMSE values are slightly smaller than those obtained with the fixed tuned inflation case.

	LETKF	ETKBF (4 steps)	DETKBF (4 steps)
$M = 10$	RMSE = 0.3215 (0.0832) spread = 0.3532(0.0324) δ = 0.0289 (0.0112)	RMSE = 0.3215 (0.0862) spread = 0.3515(0.0327) δ = 0.0289 (0.0114)	RMSE = 0.3227 (0.0883) spread = 0.3513(0.0330) δ = 0.0289 (0.0115)
$M = 15$	RMSE = 0.3190 (0.0789) spread = 0.3694(0.0329) δ = 0.0294 (0.0115)	RMSE = 0.3184 (0.0793) spread = 0.3671(0.0326) δ = 0.0292 (0.0114)	RMSE = 0.3197 (0.0791) spread = 0.3670(0.0328) δ = 0.0292 (0.0114)

Table 2. Results of the experiments with the L96 model. Three assimilation methods (columns) and two ensemble sizes (rows) are used. In each case, a sample of 10^6 assimilation cycle was used to find the average analysis RMSE, average ensemble spread and average inflation parameter (averaged also over the 40 gridpoints). The numbers in parenthesis correspond to the standard deviations of the reported parameters.

In the next figure, we plot the time-averaged value of multiplicative covariance inflation in each one of the 40 gridpoints. No noticeable differences are found between observed and unobserved gridpoints or among filters.

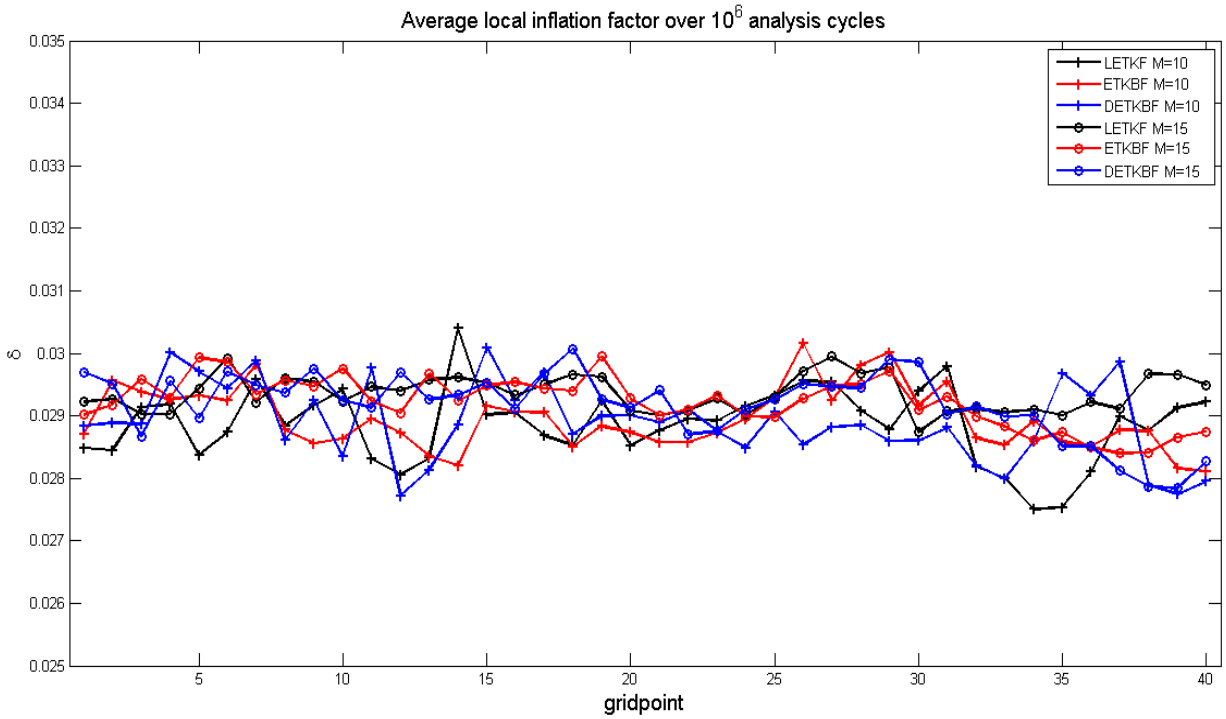

Figure 20. Local value of (multiplicative covariance inflation) for each one of the 40 gridpoints, averaged over 10^6 analysis cycles. Three filters and two ensemble sizes are presented.

3.4.3. Experiments with the SPEEDY model

Finally, we implement ETKBF and DETKBF in a model that is more representative of those used in operational numerical weather prediction. For the assimilation, an ensemble with M=20 members is used. The R-localization parameters are $\lambda = 500km$ in the horizontal and $\lambda_v = 0.1 \ln p$ in the vertical. As in the last experiments with L96, adaptive multiplicative covariance inflation (Miyoshi, 2011) is applied to avoid manual tuning. The model is started from rest (zero winds and an isothermal atmosphere) and run for a year for spin up. Then, the model is run for 2 months (January and February); these months constitute the truth. The observations are taken in locations resembling a realistic radiosonde network as explained in section 2.3.3. The performance of the different formulations was evaluated using the latitude weighted analysis RMSE presented in the same section.

As with the previous models, for the ETKBFs we look for the minimum number of pseudo-time steps that led to a performance equal to that of the LETKF. Using 3 steps or less leads to noticeable differences, starting at 4 the differences are minimal and by 6 the impact is practically indistinguishable. Moreover, for this number of steps the computational time required for an assimilation cycle is comparable to that of LETKF. For the results presented hereafter, we use a DSI scheme with 6 non-uniform steps in pseudo-time.

It will be illustrative to perform single-observation experiments in different regions of the world, especially contrasting densely observed regions vs. poorly observed regions.

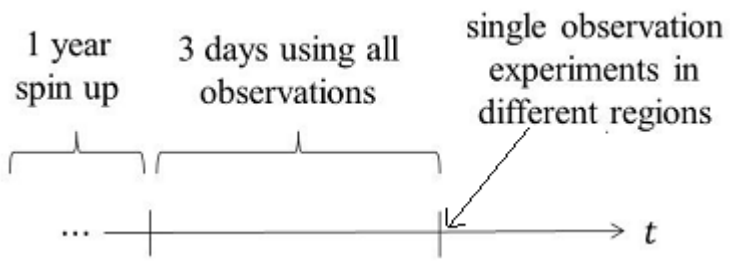

Figure 21. Schematic of set up for single-observation experiments. After the spin-up period, all observations are assimilated for three days. These allows for the differences caused by the observational density in different regions of the world to appear.

The previous figure shows the set-up for single-observations experiments. After the spin-up period, we assimilate all the observations for a short period of 3 days. This allows for the effects of the observational network density to arise. In densely observed regions of the globe the magnitude of the background error covariance is bound to be smaller than in poorly observed regions. It is after this 3-day period that we conduct the single-observation experiments described next.

In figure 22 we illustrate the impact of a single observation located over the Labrador Peninsula using the three filters. The variable depicted is zonal wind at 510 hPa. In the bottom panel of the figure we present the background value for the variable, as well as the location (red star) and magnitude of the observation being assimilated. We compute the difference between analysis mean and background mean (top part, one panel for each filter). We notice that the result is nearly identical for the three cases.

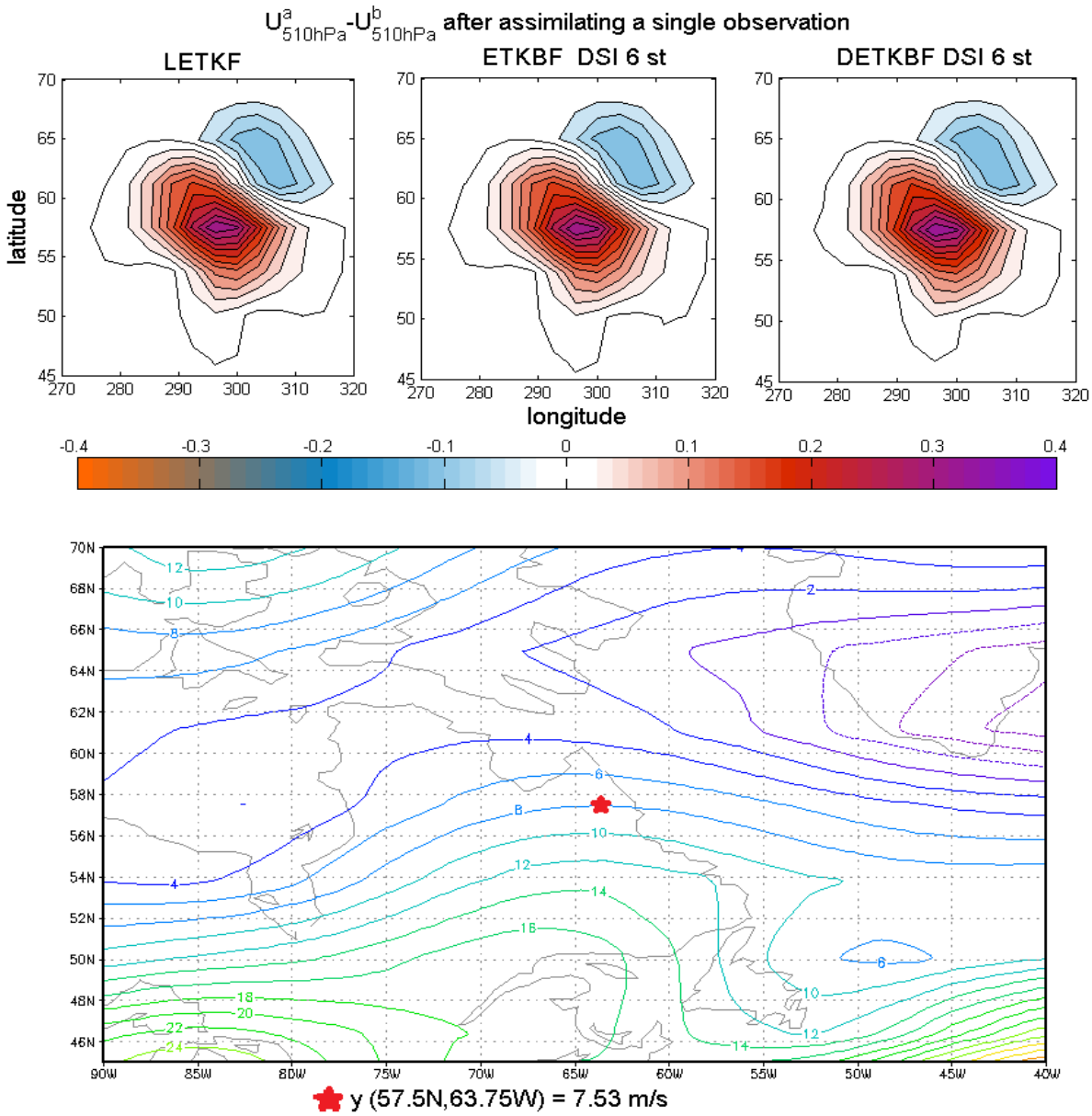

Figure 22. Impact of a single-observation experiment. The observation is located in the well-observed Labrador Peninusula. The difference between analysis mean and background mean is the same using the three methods; the variable illustrated is zonal wind at 510 hPa.

Furthermore, we use the same location and the same variable to show the time evolution (with output every 6 hours) of the background and analysis mean resulting from each one of the three filters, as well as the evolution of the background and ensemble spread. In

this case, we use all observations. The results are shown in the next figure, which again exhibits an almost indistinguishable behavior among the three formulations.

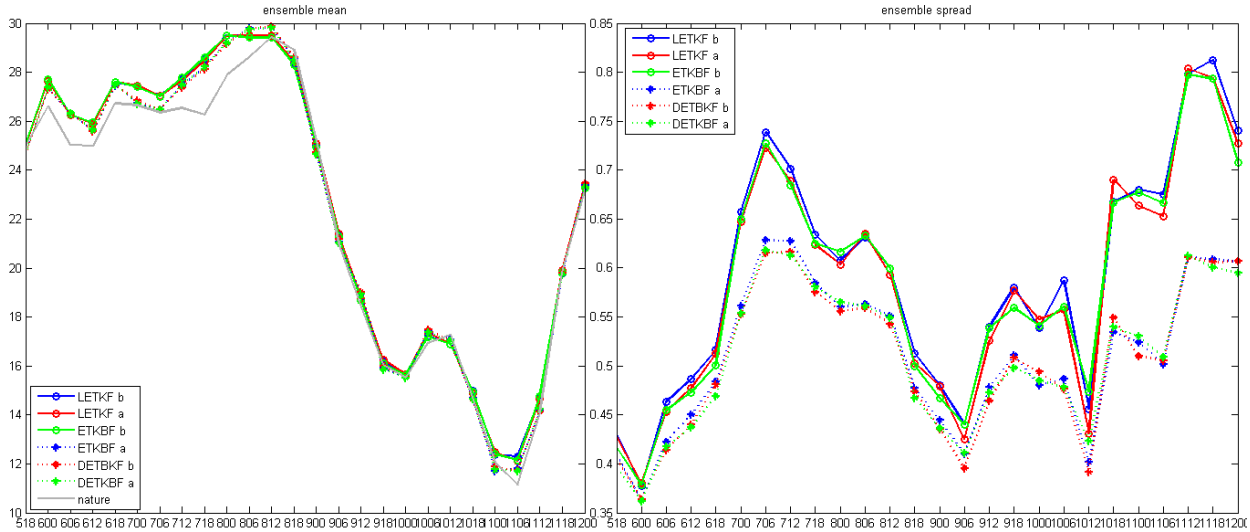

Figure 23. Time evolution of the background and analysis mean (left panel) and ensemble spread (right panel) for LETKF, ETKBF and DETKBF. The depicted variable is zonal wind at 510hPa in a location over the Labrador peninsula.

Can we expect stiffening for this model for the EnKBF/ETKBF equations? A 6-hour assimilation window can be considered linear, especially for synoptic scale features. Nonetheless, we had stated that the magnitude of $\mathbf{P}^b$ also depends on the density of the observational network. Hence, we should expect stiffness in the poorly observed areas like the southern Pacific Ocean. Figure 24 depicts a single observation experiment for an observation in this area. We choose to depict the ratio of analysis spread to background spread for the meridional wind at 950 hPa. If this ratio is small, it implies that the background ensemble covariance is reduced considerably with the information taken from observations (and hence stiffness is present). As one can notice, both ETKBF and DETKBF using the DSI method with 6 non-uniform steps in pseudo-time give the same results as LETKF. In gridpoints closest to the observation, we can observe that the

background ensemble spread was reduced by ~70%, but the DSI method could properly handle any stiffness without any further complication while the EF method failed.

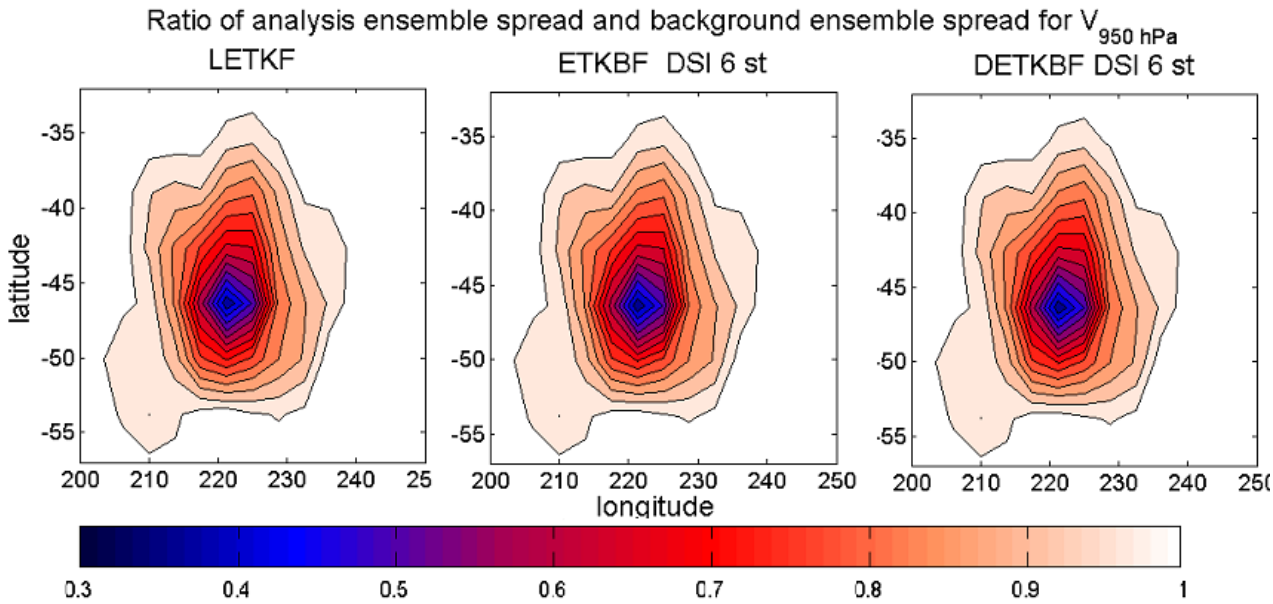

Figure 24. Impact of two single-observation experiments. The observation is located in the poorly-observed Southern Pacific, hence in an area prone to stiffness. We show the ratio of the analysis spread to background spread for the meridional wind at 950 hPa.

So far only results of particular cases have been shown. Next, we show the results from the assimilation experiments through the two months for which we generated the truth. In figure 27, we depict the time average latitude-weighted analysis RMSE for the variables $\{u, v, T, q, z\}$ (each one in every row) at each pressure level (different columns). In each panel the bars represent 1 standard deviation around the time average RMSE, which is computed globally. This figure displays indistinguishable results from the three filters.

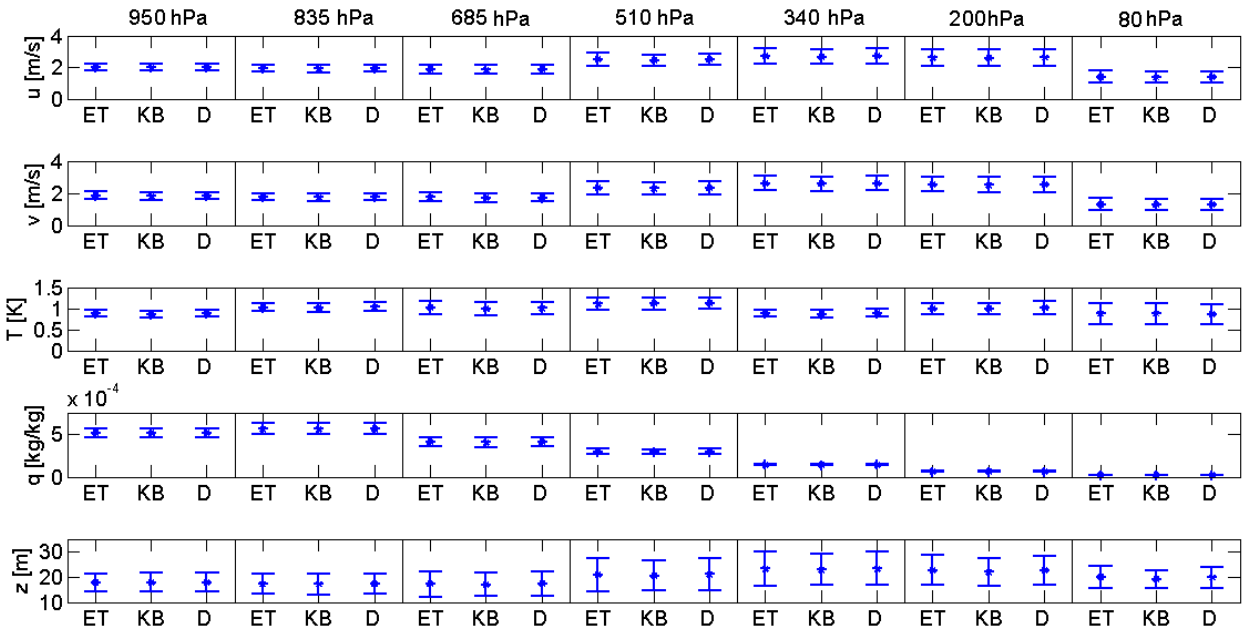

Figure 25. Analysis RMSE values computed globally for each variable at different pressure levels for the three filters.

Next we re-compute this metric separately for the following regions: Northern Hemisphere (25N-75N), topics (25S-25N) and Southern Hemisphere (75S-25S). In figures 26-28 we show the analysis RMSE for different variables; each vertical level is represented in each column and a different region represented in each row. Figure 26 shows the results for zonal and meridional wind, figure 27 shows the results for temperature and geopotential height, and figure 28 shows the results for relative humidity. For all variables, the effect of the observational density is clear and the same for the three filters. For the (well-observed) NH the mean analysis RMSE is about half of the observational error while for the SH it is generally more than the double.

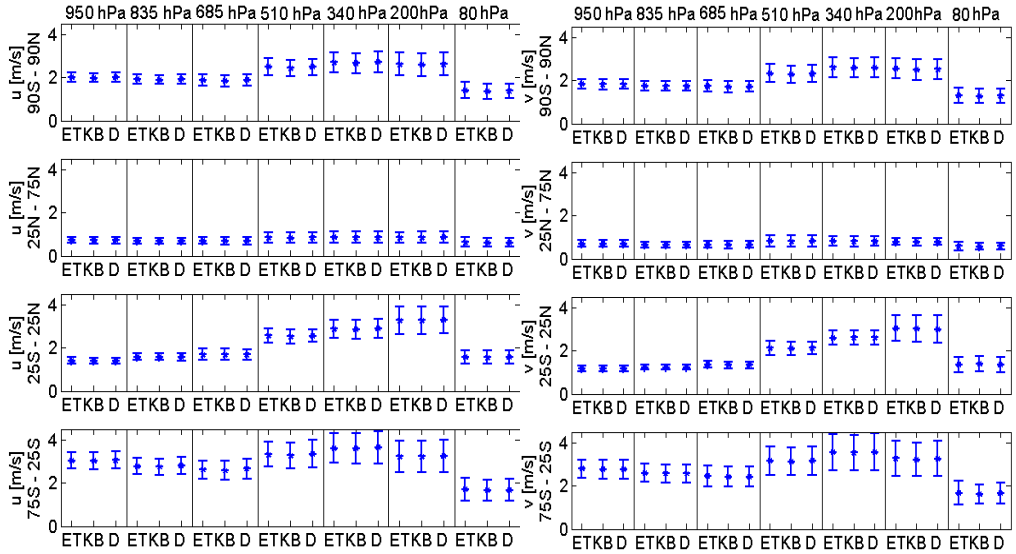

Figure 26. Analysis RMSE for zonal (left) and meridional (right) wind computed for different regions (rows) at different pressure levels (columns) for the three filters.

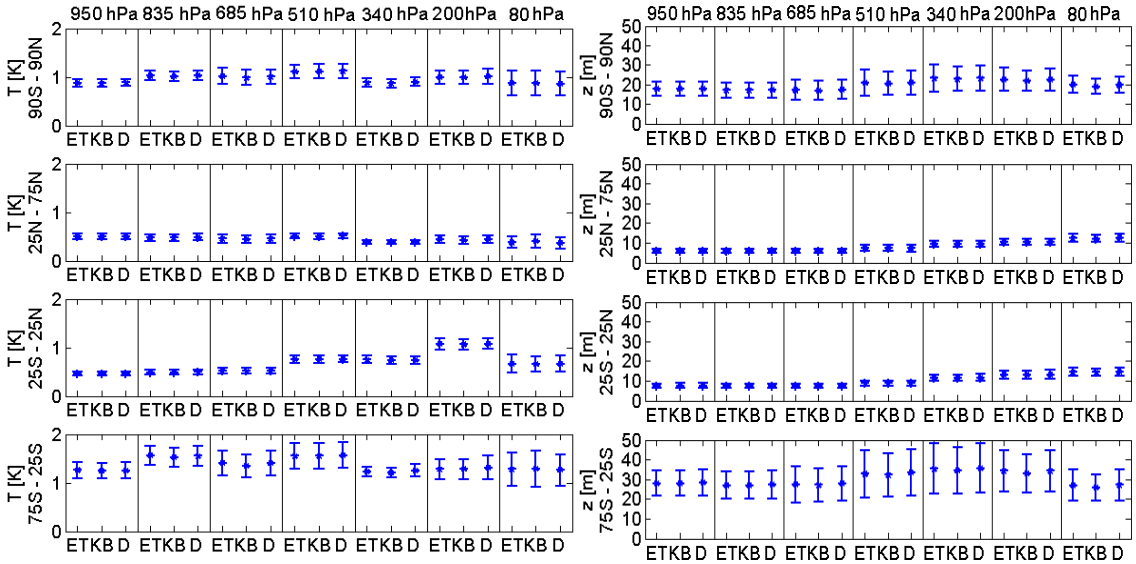

Figure 27. Analysis RMSE for temperature (left) and geopotential height (right) computed for different regions (rows) at different pressure levels (columns) for the three filters.

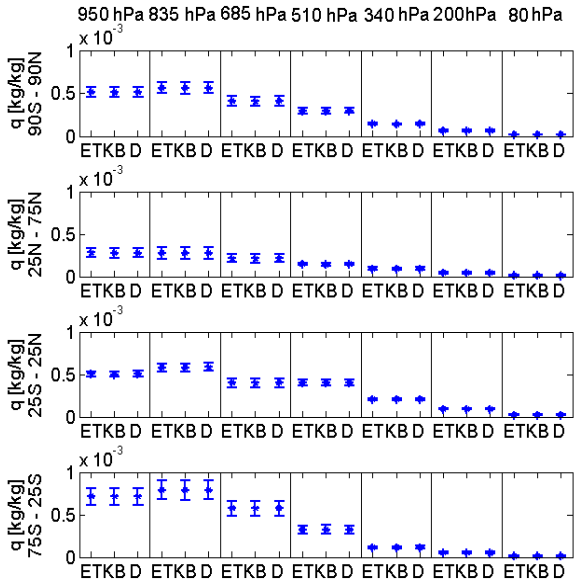

Figure 28. Analysis RMSE for relative humidity computed for different regions (rows) at different pressure levels (columns) for the three filters.

4. Ensemble clustering in ensemble square root filters

As with the KF, the optimality of any EnKF is no longer guaranteed when the nonlinearity of the error growth in the forecast becomes significant and the distribution of the ensemble members is no longer Gaussian. In nonlinear forecast models, the departure from linearity depends upon the frequency of observations, the length of the assimilation window and the magnitude of the observational error covariance **R** (Lawson and Hansen, 2004; Kalnay *et al.*, 2007).

In a seminal study, Lawson and Hansen (2004) analyzed the update mechanisms of the stochastic EnKF and the serial EnSRF, and compared their performance in linear and nonlinear regimes for the two-dimensional Ikeda system (Ikeda, 1979). Their analysis showed that the EnSRF is better at retaining higher order moments of the background distribution than the stochastic EnKF. This implies, however, that any departure from Gaussianity in the background ensemble is retained in the analysis and propagated forward in time. An important finding was that using the serial EnSRF in nonlinear regimes could lead to ensemble clustering, a phenomenon in which an *M*-member ensemble splits in an outlier and a tight cluster of *M-1* members, where the outlier is responsible for keeping the variance predicted by the KF. A result from their experiments illustrating clustering is presented in the left of figure 29. The higher order moments of the EnSRF ensembles presented non-Gaussian values, and the rank histograms (Talagrand diagrams) for the verification of the truth were U-shaped, implying that the truth and the analysis ensemble members could not be considered statistically

indistinguishable. Nonetheless, there was no difference reported in the analysis root mean squared error (RMSE) between the stochastic and the deterministic EnKFs.

Lawson and Hansen (2004) also suggested that a periodic resampling of the ensemble (e.g. via bootstrapping) could revert clustering when using an EnSRF. This idea was first implemented by Leeuwenburg *et al.* (2005) for temperature assimilation in an ocean model. They compared the performance of the one-sided ETKF (Bishop *et al.*, 2001) and a randomized alternative (which they called EnSRF+) that post-multiplied the transform matrix of the one-sided ETKF by a random rotation matrix. The EnSRF+ outperformed the one-sided ETKF in terms of the RMSE, with the higher order moments of the ensemble closer to the Gaussian. There is a caveat, however, in this study. The one-sided ETKF is not an unbiased square root filter (Livings et al, 2008; Sakov and Oke, 2008), and the EnSRF+ was not unbiased either. In fact, the one-sided ETKF is not suited to be used in data assimilation since it introduces a bias because the analysis ensemble of perturbations is not centered in zero[7]. The resulting problems are illustrated in Sakov and Oke (2008), who also compared the performance of the (unbiased) spherical-simplex ETKF (Wang et al, 2004) and an unbiased randomly rotated ETKF. Using the 40-variable Lorenz 1996 model (L96; Lorenz and Emmanuel, 1998) with different ensemble sizes and multiplicative covariance inflation factors, Sakov and Oke (2008) found similar performance for the both filters in terms of analysis RMSE (see their figure 3). Their rotated ETKF, however, produced ensembles with more Gaussian-like characteristics in terms of higher order moments and flatter rank histograms in the verification of the truth.

[7]The original purpose of the one-sided ETKF was adaptive sampling, for which it does not present any issue.

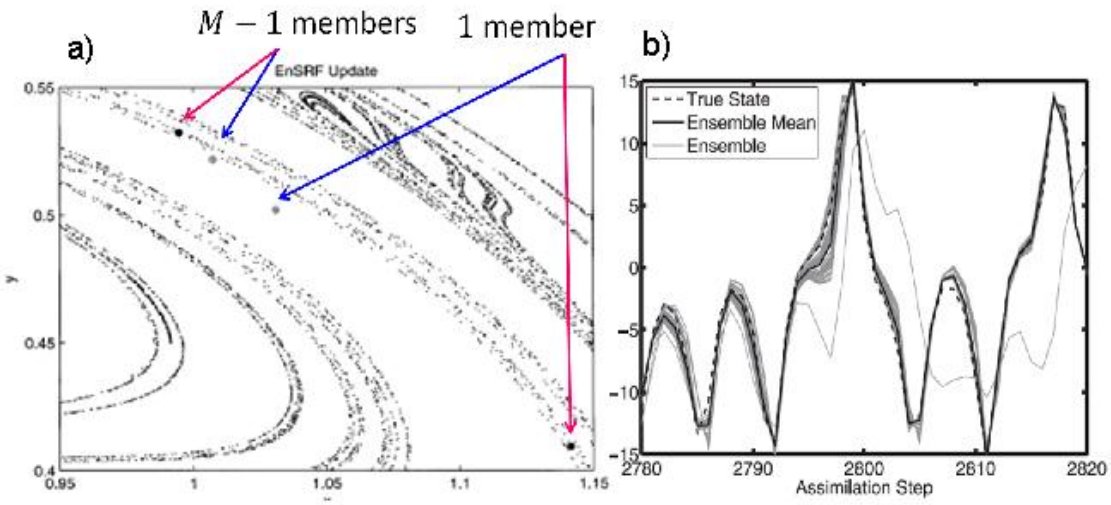

Figure 29. Examples of ensemble clustering in (a) the Ikeda model (Lawson and Hansen, 2004) and the L63 model (Anderson, 2010).

Anderson (2010) proposed a Rank Histogram Filter (RHS) as an alternative to the EAKF in highly nonlinear scenarios. Starting with a simple quadratic univariate model, he concluded that clustering is the result of the disparity between the nonlinear expansion of the ensemble spread in the forecast and the linear contraction of the ensemble spread in the analysis. This causes the outermost member to eventually become an outlier since the linear compaction needed to keep the variance constrained is sufficient for this member but larger than required for the rest of the ensemble (Anderson, 2010). Using other models (e.g. L63, shown in the right panel of figure 29), this study also showed that the analysis RMSE of the EAKF increased with ensemble size due to the nonlinear expansion in the forecast.

These problems might suggest that once clustering occurs due to the nonlinearity in the forecast model, it sets in and severely handicaps the performance of an EnSRF. The objective of this chapter is to dispel this notion. We show that clustering is in general a

transient phenomenon and illustrate the mechanism for emergence and decay. To quantify ensemble clustering at a given time, we introduce a metric, which we denominate it clustering degree (CD). Through analysis and experiments, we show advantages and disadvantages in both traditional EnSRFs and those that include random rotations to avoid clustering; each assimilation method appeals to different situations and different requirements.

All our experiments are identical twin experiments using two EnSRFs: the LETKF (Hunt et al, 2007) that is prone to the ensemble clustering, and the Mean Preserving Non-Symmetric LETKF (MPNS-LETKF), which we develop in the next subsection. The methods are compared through the background (i.e., forecast) and analysis RMSE, the higher order moment of the ensemble with sample skewness as defined in the appendix of Lawson and Hansen (2004), and the time evolution of the *CD*.

4.1 Generating mean-preserving non-symmetric solutions of ETKF

As mentioned before, ETKF is a post-multiplicative scheme such that $\mathbf{X}^a = \mathbf{X}^b \mathbf{W}^a$. In this subsection we show a simple way construct non-symmetric solutions that preserve a zero mean. First, recall the one-sided ETKF (Bishop *et al.*, 2001), which uses the following matrix of weights:

$$\mathbf{W}^a_{1-sided} = \mathbf{C}\left(\mathbf{I} + \mathbf{\Gamma}\right)^{-1/2} \tag{66}$$

where the matrices $\mathbf{C}$ and $\mathbf{\Gamma}$ come from the eigenvalue decomposition:

$$\mathbf{C}\,\mathbf{\Gamma}\,\mathbf{C}^{\mathbf{T}} = \frac{\mathbf{Y}^{\mathbf{b}\,\mathbf{T}}\mathbf{R}^{-1}\mathbf{Y}^{\mathbf{b}}}{M-1}$$

The covariance in ensemble space is:

$$\tilde{\mathbf{P}}^{a} = \mathbf{W}^{a}_{1-sided}\left(\mathbf{W}^{a}_{1-sided}\right)^{T} = \mathbf{C}\left(\mathbf{I}+\mathbf{\Gamma}\right)^{-1}\mathbf{C}^{\mathbf{T}} \tag{67}$$

This scheme, however, does not preserve a mean zero for the analysis ensemble of perturbations, i.e. if $\mathbf{1} \in \Re^{M}$ and $\mathbf{0} \in \Re^{M}$ then in general:

$$\mathbf{X}^{a}_{1-sided}\mathbf{1} = \mathbf{C}\left(\mathbf{I}+\mathbf{\Gamma}\right)^{-1/2}\mathbf{1} \neq \mathbf{0}$$

The equality is fulfilled in very restricted cases (Livings *et al.*, 2008). An alternative to the one-sided ETKF is the spherical simplex ETKF (Wang *et al.*, 2004), which is equivalent to the Local ETKF (Hunt *et al*., 2007) with no localization. This scheme uses a 'symmetric' form for the matrix of weights:

$$\mathbf{W}^{a}_{sym} = \mathbf{C}\left(\mathbf{I}+\mathbf{\Gamma}\right)^{-1/2}\mathbf{C}^{\mathbf{T}} \tag{68}$$

Since $\mathbf{C}$ is an orthonormal matrix, the covariance in ensemble space is the same as the one obtained with the one-sided ETKF:

$$\tilde{\mathbf{P}}^{a} = \mathbf{W}^{a}_{sym}\left(\mathbf{W}^{a}_{sym}\right)^{T} = \mathbf{C}\left(\mathbf{I}+\mathbf{\Gamma}\right)^{-1/2}\mathbf{C}^{\mathbf{T}}\mathbf{C}\left(\mathbf{I}+\mathbf{\Gamma}\right)^{-1/2}\mathbf{C}^{\mathbf{T}} = \mathbf{C}\left(\mathbf{I}+\mathbf{\Gamma}\right)^{-1}\mathbf{C}^{\mathbf{T}} \tag{69}$$

Moreover, this formulation guarantees the preservation of the zero mean, i.e.:

$$\mathbf{X}^{a}_{sym}\mathbf{1} = \mathbf{C}\left(\mathbf{I}+\mathbf{\Gamma}\right)^{-1/2}\mathbf{C}^{\mathbf{T}}\mathbf{1} = \mathbf{0}$$

A general 'non-symmetric' ETKF can be written as

$$\mathbf{W}_{ns}^{a} = \mathbf{C}(\mathbf{I}+\mathbf{\Gamma})^{-1/2}\mathbf{S}^{\mathbf{T}} \tag{70}$$

where $\mathbf{S}$ must be orthonormal (to preserve the prescribed covariance) and guarantee that:

$\mathbf{X}_{ns}^{a}\mathbf{1} = \mathbf{X}^{b}\mathbf{C}(\mathbf{I}+\mathbf{\Gamma})^{-1/2}\mathbf{S}^{\mathbf{T}}\mathbf{1} = \mathbf{0}$.

This occurs *as long as* $\mathbf{S}$ *contains the column* $\mathbf{1}$ *as an eigenvector*. Instructions to construct this matrix as well as a proof of the claim are listed next:

a) Generate a matrix with random entries $\overline{\overline{\mathbf{G}}} = [\mathbf{g}_1, \mathbf{g}_2, \cdots, \mathbf{g}_M] \in \Re^{M\times M}$.

b) Compute a matrix of perturbations $\mathbf{G} = [\mathbf{g}_1 - \overline{\mathbf{g}}, \mathbf{g}_2 - \overline{\mathbf{g}}, \cdots \mathbf{g}_M - \overline{\mathbf{g}}]$, where $\overline{\mathbf{g}} = M^{-1}\overline{\overline{\mathbf{G}}}\mathbf{1}$. By construction $\mathbf{G1} = \mathbf{0}$.

c) Perform the eigenvalue decomposition of the matrix $\mathbf{G}^{\mathbf{T}}\mathbf{G} = \mathbf{S}\mathbf{\Lambda}\mathbf{S}^{\mathbf{T}}$. Since $\mathbf{G}^{\mathbf{T}}\mathbf{G}$ is symmetric (and therefore normal), $\mathbf{S}$ has orthonormal columns, i.e. $\mathbf{S}^{\mathbf{T}}\mathbf{S} = \mathbf{S}\mathbf{S}^{\mathbf{T}} = \mathbf{I}$. Moreover, all the eigenvalues in $\mathbf{\Lambda}$ are nonnegative.

d) Sort the eigenvalues by magnitude, and order the eigenvectors in $\mathbf{S}$ correspondingly. Since $\mathbf{G} \in \Re^{M\times M}$ and $\mathbf{G1} = \mathbf{0}$, $\lambda_M = 0$ and $\mathbf{s}_M = M^{-1/2}\mathbf{1}$. The elements of $\mathbf{\Lambda}$ and $\mathbf{S}$ are:

$\mathbf{\Lambda} = diag([\lambda_1, \lambda_2, \cdots, \lambda_{M-1}, 0])$, $\mathbf{S} = [\mathbf{s}_1, \mathbf{s}_2, \cdots, \mathbf{s}_{M-1}, M^{-1/2}\mathbf{1}]$.

Now let's prove that the solution preserves the zero mean. First, we perform the operation:

$$\mathbf{X}_{ns}^{a}\mathbf{1} = \mathbf{X}^{b}\mathbf{C}(\mathbf{I}+\mathbf{\Gamma})^{-1/2}\left[\mathbf{s}_1^{\mathbf{T}},\mathbf{s}_2^{\mathbf{T}},\cdots,\mathbf{s}_{M-1}^{\mathbf{T}},M^{-1/2}\mathbf{1}^{\mathbf{T}}\right]\mathbf{1} = \mathbf{X}^{b}\mathbf{C}(\mathbf{I}+\mathbf{\Gamma})^{-1/2}\left[0,0,\cdots,0,M^{1/2}\right]^{\mathbf{T}} \quad (71)$$

To proceed any further, we have to consider the structure of $\mathbf{C}$ and $\mathbf{\Gamma}$. Since $\mathbf{Y}^{\mathbf{b}^{\mathbf{T}}}\mathbf{R}^{-1}\mathbf{Y}^{\mathbf{b}}/(M-1)$ is symmetric (hence normal), the columns of $\mathbf{C}$ are orthonormal and the eigenvalues of $\mathbf{\Gamma}$ are nonnegative. Two cases arise:

<u>Case 1:</u> $M < N$. This is the most common case in practice, and also the one for the proof is simpler. If we sort the eigenvalues of $\mathbf{\Gamma}$ by magnitude and the columns of $\mathbf{C}$ correspondingly, then we have that $\gamma_M = 0$ and $\mathbf{c}_M = M^{-1/2}\mathbf{1}$. Therefore:

$$\mathbf{X}_{ns}^{a}\mathbf{1} = \mathbf{X}^{b}\left[\mathbf{s}_1^{\mathbf{T}},\mathbf{s}_2^{\mathbf{T}},\cdots,M^{-1/2}\mathbf{1}^{\mathbf{T}}\right]\begin{bmatrix}(1+\gamma_1)^{-1/2} & 0 & \cdots & 0\\ 0 & (1+\gamma_2)^{-1/2} & \cdots & 0\\ \vdots & \vdots & \ddots & \vdots\\ 0 & 0 & \cdots & 1\end{bmatrix}\left[0,0,\cdots,M^{1/2}\right]^{\mathbf{T}}$$

If we perform operations we find that:

$$\mathbf{X}_{ns}^{a}\mathbf{1} = \mathbf{X}^{b}\left[\mathbf{s}_1^{\mathbf{T}},\mathbf{s}_2^{\mathbf{T}},\cdots,\mathbf{s}_{M-1}^{\mathbf{T}},M^{-1/2}\mathbf{1}^{\mathbf{T}}\right]\left[0,0,\cdots,0,M^{1/2}\right]^{\mathbf{T}} = \mathbf{X}^{b}\mathbf{1} = \mathbf{0} \quad (72)$$

<u>Case 2</u> $M > N$. It is unusual in practice to have more ensemble members than variables. This is the case, nonetheless, of our experiments with the univariate quadratic model. For this case the last $M-N$ eigenvalues in $\mathbf{\Gamma}$ will be zero, but we cannot say much about

the corresponding eigenvectors, only that they are not orthogonal to the vector $\mathbf{1}$ (hence we cannot apply the procedure used in the other case). We can write:

$$\mathbf{X}_{ns}^{a}\mathbf{1} = \mathbf{X}^{b}\left[\mathbf{s}_1^{\mathbf{T}}, \mathbf{s}_2^{\mathbf{T}}, \cdots, \mathbf{s}_{M-1}^{\mathbf{T}}\right]\begin{bmatrix} (1+\gamma_1)^{-1/2} & 0 & \cdots & 0 \\ 0 & (1+\gamma_2)^{-1/2} & \cdots & 0 \\ \vdots & \vdots & \ddots & \vdots \\ 0 & 0 & \cdots & (1+\gamma_M)^{-1/2} \end{bmatrix}\left[0,0,\cdots,0,M^{1/2}\right]^{\mathbf{T}}$$

And performing the operations we have:

$$\mathbf{X}_{ns}^{a}\mathbf{1} = \mathbf{X}^{b}\mathbf{C}\left[0,0,\ldots,\sqrt{\frac{M}{1+\gamma_M}}\right]^{T} \tag{73}$$

At this point we focus on the structure of $\mathbf{X}^{b} \in \Re^{N\times M}$. Its singular value decomposition is $\mathbf{X}^{b} = \mathbf{U\Sigma V}^{\mathbf{T}}$ where $\mathbf{U} \in \Re^{N\times N}$, $\mathbf{V} \in \Re^{M\times M}$ and $\mathbf{\Sigma} \in \Re^{N\times M}$ is a rectangular diagonal matrix. Taking this into consideration, we find:

$$\mathbf{C\Gamma C}^{\mathbf{T}} = \frac{\mathbf{Y}^{\mathbf{b}^{\mathbf{T}}}\mathbf{R}^{-1}\mathbf{Y}^{\mathbf{b}}}{(M-1)} = \mathbf{X}^{\mathbf{b}^{\mathbf{T}}}\frac{\mathbf{H}^{\mathbf{T}}\mathbf{R}^{-1}\mathbf{H}}{(M-1)}\mathbf{X}^{\mathbf{b}} = \mathbf{V\Sigma}^{\mathbf{T}}\mathbf{U}^{\mathbf{T}}\frac{\mathbf{H}^{\mathbf{T}}\mathbf{R}^{-1}\mathbf{H}}{(M-1)}\mathbf{U\Sigma V}^{\mathbf{T}}$$

Therefore, $\mathbf{C} = \mathbf{V}$ and $\mathbf{\Gamma} = \mathbf{\Sigma}^{\mathbf{T}}\mathbf{U}^{\mathbf{T}}\mathbf{H}^{\mathbf{T}}\mathbf{R}^{-1}\mathbf{HU\Sigma}/(M-1)$. With this in mind:

$$\mathbf{X}_{ns}^{a}\mathbf{1} = \mathbf{U\Sigma C}^{\mathbf{T}}\mathbf{C}\left[0,0,\ldots,(1+\gamma_M)^{-1/2}M^{1/2}\right]^{T} = \mathbf{U\Sigma}\left[0,0,\ldots,\sqrt{\frac{M}{1+\gamma_M}}\right]^{T} \tag{74}$$

Since $\mathbf{\Sigma} \in \Re^{N\times M}$ is a rectangular diagonal matrix and $M > N$, the last $M-N$ rows are columns of zeros. Therefore, the product $\mathbf{\Sigma}\left[0,0,\ldots,(1+\gamma_M)^{-1/2}M^{1/2}\right]^{T} = \mathbf{0} \in \Re^{N}$. Therefore

$$\mathbf{X}_{ns}^{a}\mathbf{1} = \mathbf{U\Sigma}\left[0,0,\ldots,\sqrt{\frac{M}{1+\gamma_M}}\right]^{T} = \mathbf{U0} = \mathbf{0} \tag{75}$$

This concludes the proof for the two cases.

When localization is used, we may need to rotate the symmetric solution of the ETKF (section 4.4), namely to have a transformation matrix of the form:

$$\mathbf{W}^a = \mathbf{W}^a_{sym}\hat{\mathbf{S}}^{\mathbf{T}} = \mathbf{C}\left(\mathbf{I}+\mathbf{\Gamma}\right)^{-1/2}\mathbf{C}\hat{\mathbf{S}}^{\mathbf{T}} \tag{76}$$

$\hat{\mathbf{S}} \in \Re^{M\times M}$ obviously needs to be orthogonal and we also require $\hat{\mathbf{S}}^{\mathbf{T}}\mathbf{1} = \mathbf{1}$. An easy way to construct this matrix is the following (based on Sakov and Oke (2008b) and Horn and Johnson (1985)):

$$\hat{\mathbf{S}} = \mathbf{S}\begin{bmatrix}\mathbf{T} & 0\\ 0 & 1\end{bmatrix}\mathbf{S}^T \tag{77}$$

Where $\mathbf{S} \in \Re^{M\times M}$ and $\mathbf{T} \in \Re^{(M-1)\times(M-1)}$ are constructed as indicated in the steps (a)-(d) of this appendix.

4.2. Metric for ensemble clustering and experimental setup

Starting with a univariate ensemble, we define clustering degree (*CD*) as:

$$CD = \frac{\sigma^2_{M-1}}{\sigma^2_M} \tag{78}$$

The denominator of (78) is the variance of the *M*-member ensemble, while the numerator is the variance of the *M-1*-member ensemble that remains after removing the outermost

member of the original. By this definition, *CD* spans from zero to one. If ensemble clustering is present, most of the variance comes from the outermost member and hence *CD* will tend towards zero. The time evolution of this metric for an unclustered ensemble will vary around a mean value which depends upon *M*, so that an accurate interpretation of this metric is restricted in identifying clustering.

For a multidimensional case, this metric can be generalized to:

$$CD = \frac{Trace\left(P_{M-1}\right)}{Trace\left(P_M\right)} \tag{79}$$

The denominator is the trace of the *M*-member ensemble covariance matrix, while the numerator is the trace of the *M-1*-member ensemble covariance matrix after removing the outermost member. Equation (79) is adequate in the multidimensional case only when the variables have the same units. If this is not the case, one can use a proper norm (e.g. an energy norm) when summing the variances, or one can perform the analysis separately for different sets of variables.

4.3. Ensemble clustering in a simple nonlinear model

We start from a simple model to explain the mechanisms that set in and reverse clustering. Following Anderson (2010), we consider the univariate quadratic ODE $dx/dt = x + b|x|x$. A prediction model based on the Euler forward discretization of this ODE is:

$$x_{t+1} = x_t + \Delta\left(x_t + b\,|x_t|x_t\right) \tag{80}$$

where $\Delta = 0.05$ is the time step. This model exhibits the desirable nonlinear expansion described in the previous section through the nonlinear coefficient *b*. The system described by (80) has an unstable fixed point at the origin, which we use as the truth, i.e., $x^t = x^* = 0$. Observations are made every 2 model steps unless otherwise noted, by adding a random noise term $\sim N(0,1)$. We assimilate every time we observe. We vary the ensemble size, $M = \{10,20,100\}$ and the nonlinearity coefficient, $b \in [0,0.2]$, where Anderson (2010) used $b = 0.2$. The members of the initial ensemble are drawn uniformly from the interval $[-1,1]$.

Figure 30 shows the time evolution of the analysis ensemble for the case $b = 0.1$ and $M = 10$ with LETKF (panel (a)) and MPNS-ETKF (panel (b)). Panel (c) illustrates the application of CD: for LETKF, CD smoothly decreases towards zero, while for MPNS-ETKF it changes abruptly at every analysis, but the variation remains around the mean.

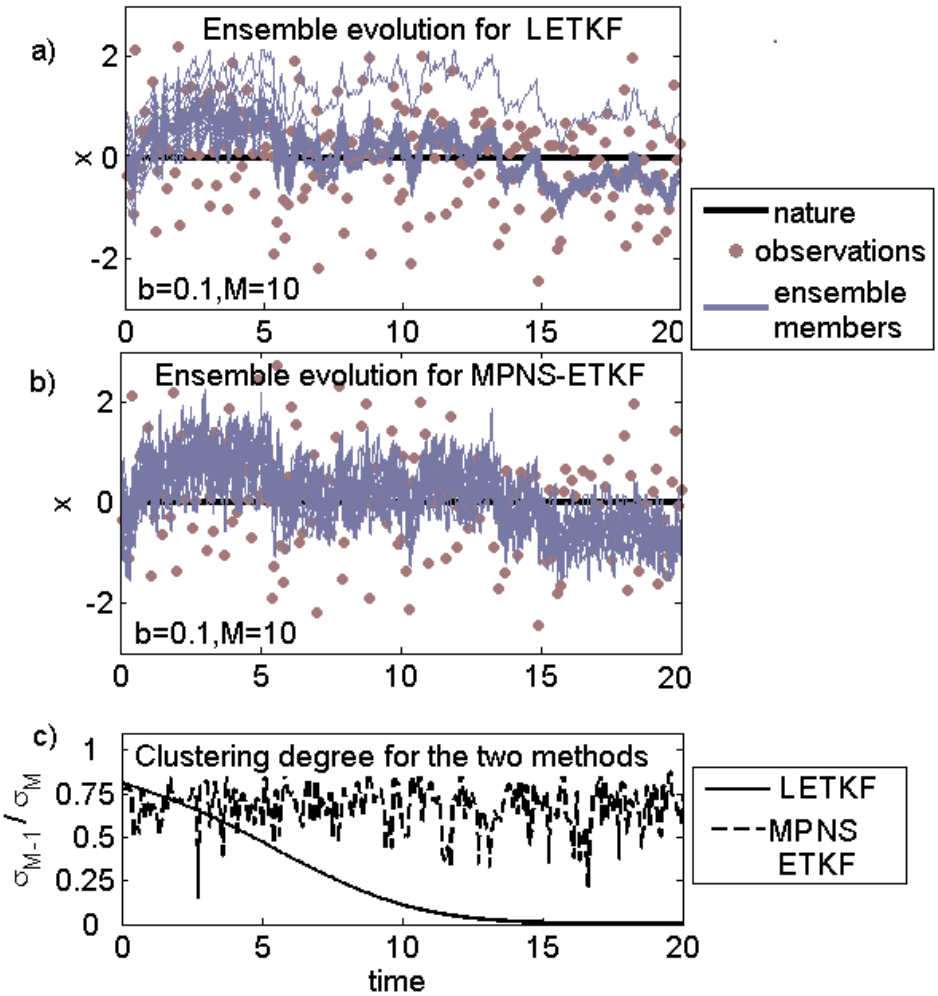

Figure 30. Data assimilation experiment with the model $x_{t+1} = x_t + 0.05\left(x_t + b\left|x_t\right|x_t\right)$, observations every 2 model steps, and $M = 10$. For panels (a)-(c) $b = 0.2$. LETKF (a) presents ensemble clustering soon after 5 time units while the MPNS-ETKF (b) doesn't. In (c) we quantify the clustering degree for both filters.

Then we study how the combinations of different ensemble sizes *M* and degrees of nonlinearity b affect the appearance of clustering; this is shown in the next figure. Clustering occurs for the LETKF for any $b > 0$; it emergence occurs earlier as b increases. The clustering tends occur more gradually for smaller *M* and more abruptly for larger *M*. In all cases the ensembles seem to collapse at the same time that depends solely on b.

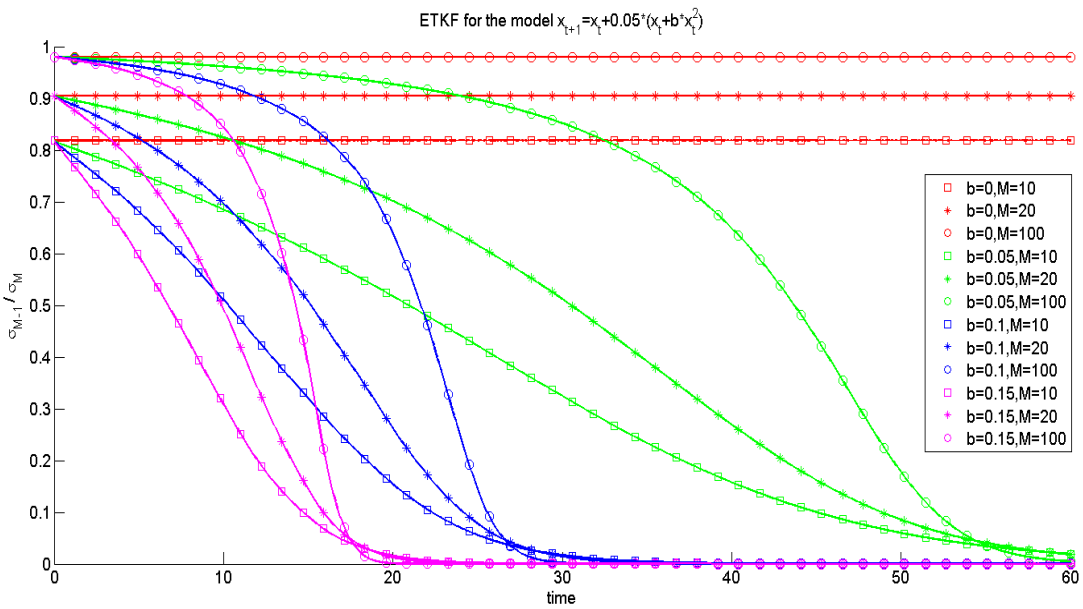

Figure 31. Data assimilation experiment with the model $x_{t+1} = x_t + 0.05\left(x_t + b\left|x_t\right|x_t\right)$. The clustering degree is measured for LETKF different ensemble sizes and values of *b*.

So far our experiments have shown that clustering does not arise when using MPNS-ETKF. To illustrate why this non-symmetric formulation prevents EC, we depict the update process of both filters from background to analysis for each one of the $M = 10$ members in the figure 32. To accelerate the emergence of clustering we take observations every 5 model steps and $b = 0.2$. For LETKF (top panel), the analysis ensemble is chosen to be as close as possible to the background ensemble (Ott *et al.*, 2004). Therefore, any deformation introduced by the nonlinear expansion in the forecast will remain in the analysis; the separation of the outliner member from the cluster cannot be stopped once it starts. By contrast, MPNS-ETKF (bottom panel) effectively erases any deformation occurred during the forecast via a constrained resampling at each analysis.

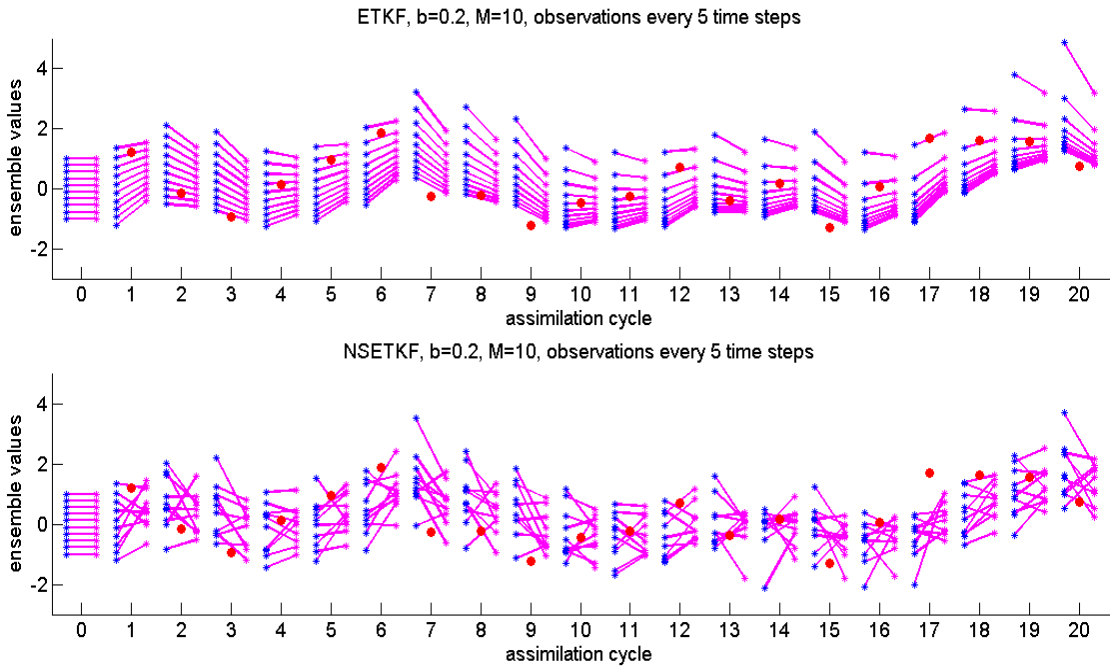

Figure 32. Update mechanisms for LETKF and MPNS-ETKF for the individual ensemble members, with the red dots indicating the observation value. LETKF preserves the structure from the background ensemble into the analysis ensemble. The MPNS-ETKF effectively scrambles the ensemble every time an assimilation occurs. The model is $x_{t+1} = x_t + 0.05\left(x_t + b|x_t|x_t\right)$, $b = 0.2$, observations every 5 model steps, and $M = 10$.

The verification of the truth with respect to the analysis ensemble was computed for both methods. This information is presented in figure 33: the blue line represents the evolution of CD (measured in the left axis) with respect to time, and the green asterisks represent the position of the truth (measured in the right axis) within the ensemble for different times. As shown in this figure, for LETKF the truth very often falls either outside the ensemble or between the outlier and the cluster. For MPNS-ETKF the truth is statistically undistinguishable for the ensemble, leading to flat rank histograms (not shown). Both methods, however, estimate very similar analysis means, leading to indistinguishable performances in terms of RMSE. Nonetheless, an important aspect is that for LETKF one

can trace individual ensemble trajectories to the past (this is one of the benefits of EnSRFs pointed out by Anderson 2001), but for MPNS-ETKF the information about the individual trajectories is lost every time at every assimilation. This is shown in figure 34.

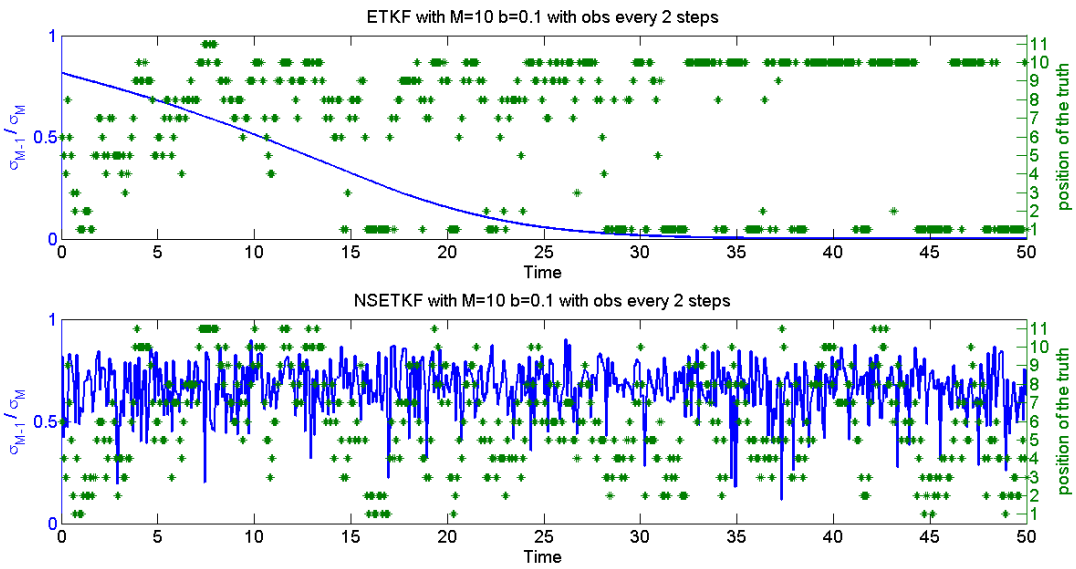

Figure 33. Clustering degree (left axis) and position of the truth within the ensemble (right axis) for LETKF and MPNS-ETKF for the individual ensemble members.

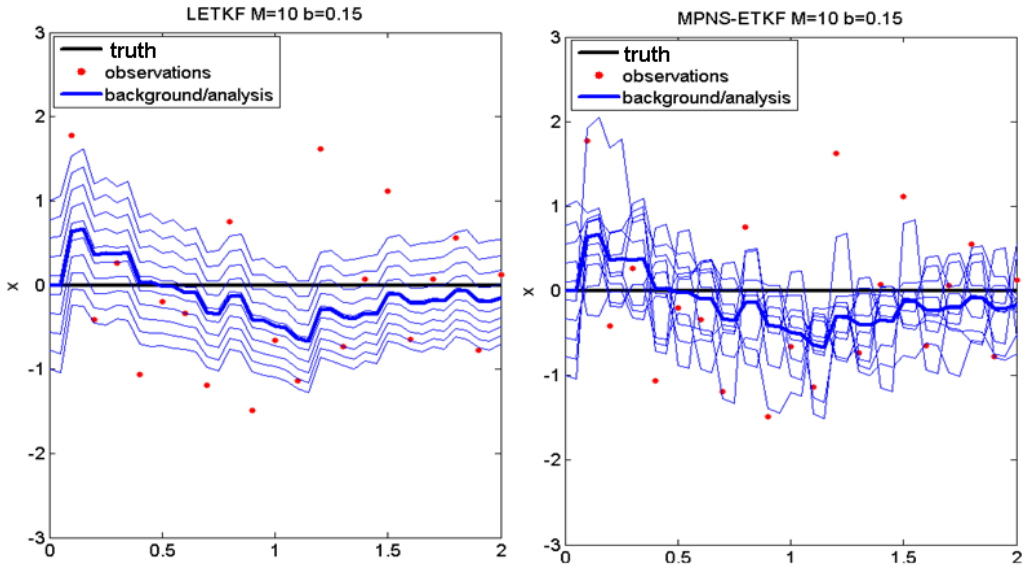

Figure 34. Data assimilation with the simple univariate model. When using LETKF (left) one can follow individual trajectories for the ensemble members. This ability is lost when using MPNS_ETKF (right) since the ensemble is 'rebooted' every time assimilation is performed.

The experiments presented so far seem to suggest that once the clustering sets in, it is irreversible and can imply a major obstacle for an EnSRF. It is crucial to realize that nonlinearity is kept constant by keeping b fixed using the simple univariate model (80); in higher-dimensional models, however, nonlinearity is spatially and temporally variable as the trajectory may visit different regions of the phase space. In the reminder of this chapter, we demonstrate that this variability of the nonlinearity can help revert the clustering and thus the clustering is a transient phenomenon.

To introduce the variability of nonlinearity in (80), we let b change every T model time steps, where T comes from a uniform distribution $\sim U(T_0, 2T_0)$. Every time a 'cycle' of length T completes, a new b is drawn from $N(0,0.1)$. Hence, forecast model dynamics experience different dynamical regimes for ensemble spread near the truth: unstable expansion ($b > 0$) or stable contraction ($b < 0$). Dynamics is quasi linear for $|b| \sim 0$, and ~95% of the cycles have $|b| < 0.2$.

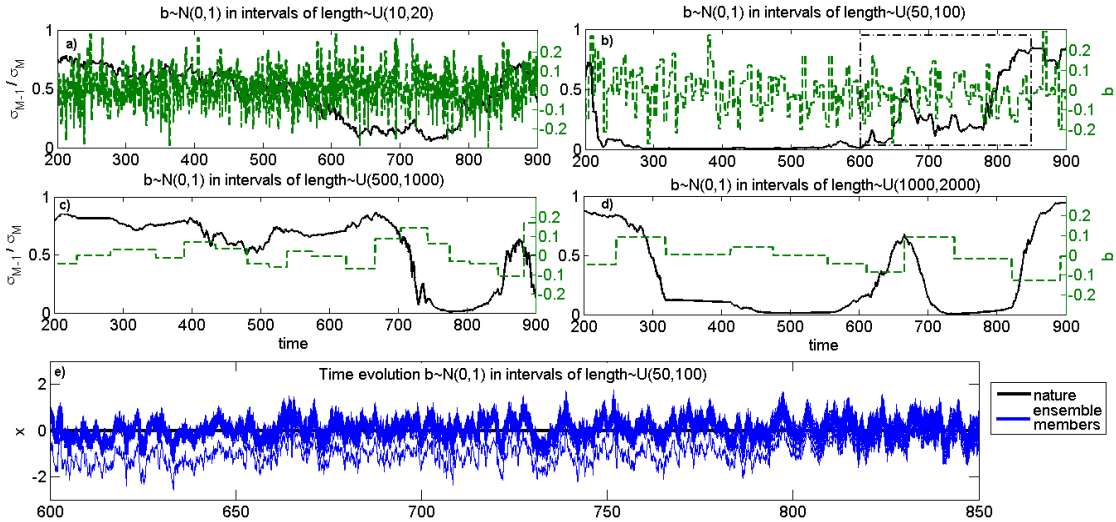

Figure 35. Assimilation experiments with the model $x_{t+1} = x_t + 0.05\left(x_t + b|x_t|x_t\right)$. We allow the nonlinear coefficient b_t to vary as a piece-wise function of time (green line, right vertical axes). The clustering degree is represented by the black line and left vertical axes. The time intervals in which b_t is fixed are different for each panels. Panel (e) shows the ensemble evolution for the time interval $t \in [600,850]$ of case (b); the reattachment of the outlier occurs in a natural way.

In panels (a)-(d) of figure 35 we show the time evolution of *b* in gray line (right vertical axis) along with the clustering degree (*CD*) of the LETKF in black line (left vertical axis) for the interval $t \in [200,900]$. We show the results for the cases $T_0 = \{50,100,500,1000\}$ model steps in these panels. By introducing the variability in nonlinearity of the forecast model, the LETKF no longer suffers from irreversible clustering. In panel (b), around $t \approx 200$ clustering sets in due to large positive values of *b*. Clustering persists until $t \approx 600$ but decays as the outlier returns to the rest of the ensemble as shown in panel (e).

In this simple model, clustering can persistent over a long period although introduction of the artificial variability in nonlinearity eventually resolves the clustering. In higher-dimensional model with natural variability in nonlinearity, the clustering is less persistent as we demonstrate in the next sections.

4.3 Localization aspects of the MPNS-LETKF

As discussed in previous sections R-localization (Hunt *et al.*, 2007) is a natural choice for post-multiplicative EnSRFs. In this scheme, an independent analysis is carried out for every single grid point using observations within a certain distance, and assuming that the observation error increases with the distance to the grid point (see Greybush *et al.*, 2011 for details). For stability in the model forecast, it is important that the analyses obtained in neighboring grid points vary smoothly. This was one of the reasons behind the symmetric square root used in the LETKF (Hunt *et al.*, 2007).

The smoothness among grid points in the analysis is not guaranteed automatically by MPNS-ETKF. We perform a simple assimilation experiment with the 40-variable L96 model to illustrate that this method cannot be applied *directly* with R-localization and that it requires some additional steps.

With R-localization, the filter independently calculates a local matrix of weights $\mathbf{W}^{a}_{local} \in \Re^{M \times M}$ for each one of the $N = 40$ gridpoints, as illustrated schematically in the next figure:

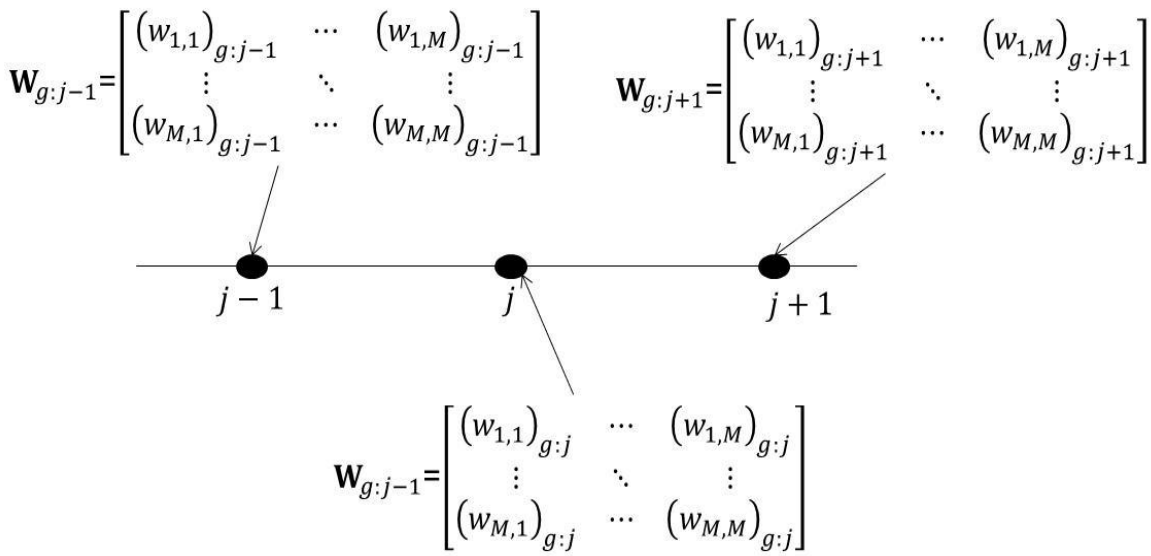

Figure 36. Schematic depicting the effect of R-localization in the LETKF. Each grid-point has its own matrix of weights; a smooth transition among these weights is indispensable to ensure stability.

For illustration purposes, we select gridpoint 12 (the result is valid for all gridpoints) and calculate the correlation of each one of its $M^2 = 10^2$ weights with respect to the weights from the all the other gridpoints. Figure 37 shows these correlations for LETKF (black line, left vertical axis) and MPNS-ETKF (gray line, right vertical axis). The difference is evident: while the correlation obtained by LETKF varies smoothly and with values very close to unity, for MPNS-ETKF this curve varies sharply and in general has small correlation values. As expected, we observe filter divergence when using this method.

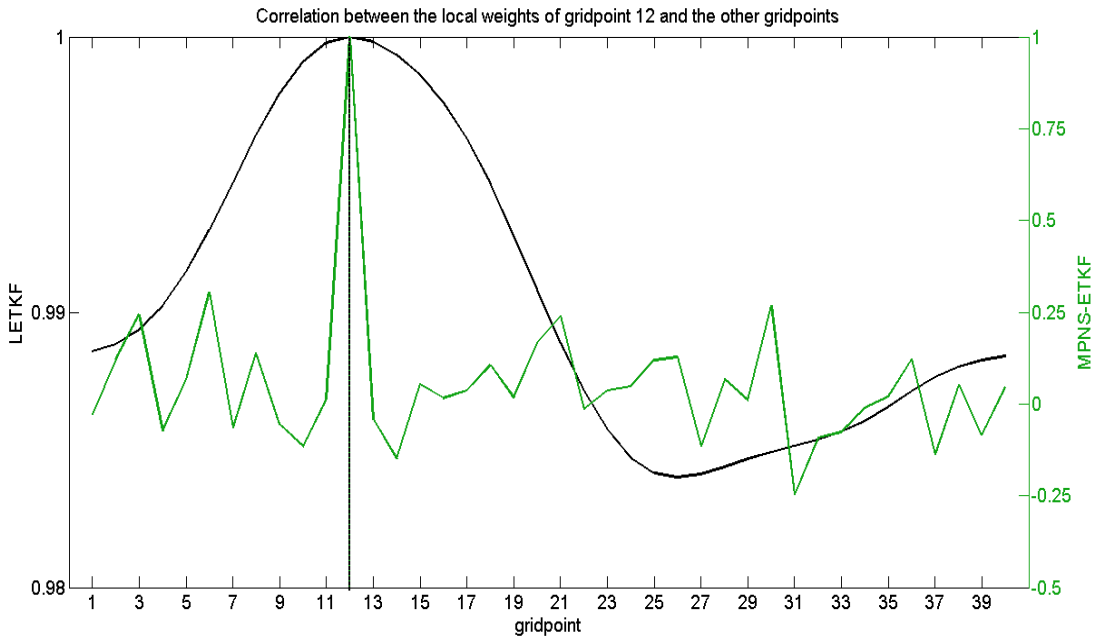

Figure 37. Correlation between the analysis weights of gridpoint 12 with respect to the weights in neighboring gridpoints for the L96 model. For LETKF (black line, left vertical axis) the correlation values are high and they present a smooth transition. For MPNS-ETKF (gray line, right vertical axis), the transition is not smooth and the correlation values are low. MPNS-ETKF cannot be directly applied with R-localization.

Random rotations can still be applied in this case. Using R-localization implies building $\mathbf{X}^a$ by sets of rows at a time, the size of each set corresponding to the number of variables in every gridpoint. Once $\mathbf{X}^a$ is completely calculated from local symmetric analyses (i.e., using LETKF), it can be globally rotated. This version of the MPNS-ETKF has no problems of divergence and can benefit from the ensemble resampling.

4.4. Experiments

We now proceed to perform experiments with larger dimensional models, first with L63 and then with SPEEDY.

4.3.1 Experiments with the Lorenz 1963 model

Focuses of this section are the effect of the ensemble size *M* with respect to the model dimension *N* as well as that of linear and nonlinear dynamics on the background ensemble spread in the forecast. In these experiments, we use ensemble sizes $M = \{3,10,20\}$. For $M = 3$ with the rank-deficient background covariances P_M and P_{M-1} in (79) $M-1<N$, multiplicative covariance inflation $\mathbf{X}^b \to \mathbf{X}^b(1+\delta)$ is applied with $\delta = 0.04$ for the short assimilation window and $\delta = 0.4$ for the long assimilation window. These values are close to the optimal values obtained in Kalnay *et al.* (2007) and those obtained in the experiments in the chapter 3 of this work. As in section 3.3.1, two types of observing system are used: one with a short assimilation window using frequent observations at every 8 model steps and the other with a longer window sing infrequent observations at every 24 model steps. The short and long assimilation windows respectively correspond to the linear and nonlinear regimes for ensemble spread in the mode forecast (Kalnay *et al.*, 2007).

Figure 38 shows the CD for the $t \in [1525,1550]$. The top row illustrates the cases for the linear regime, while the bottom row represents the cases within the nonlinear regime. For

$M = 3$ (left column), we observe very rapid variations in the CD for both LETKF (black line) and MPNS-ETKF (gray line). This is natural, since the sample size is rather small. Still some instances of clustering (e.g. $t \approx 1548$ in the nonlinear regime) emerge in the nonlinear regime for LETKF. With larger ensemble sizes there is a clear difference in the CD between LETKF and MPNS-ETKF. For MPNS-ETKF it varies abruptly (but around a mean value) every time the assimilation is performed, but the variation is smaller as the ensemble size increases. For LETKF the variations in the CD are slower and smoother; CD can reach low values in both the linear and nonlinear regimes, but it does so more often in the nonlinear regime. There are no cases of irreversible collapse of the ensemble; when clustering occurs it is only transient and not as persistent as with the simple quadratic model.

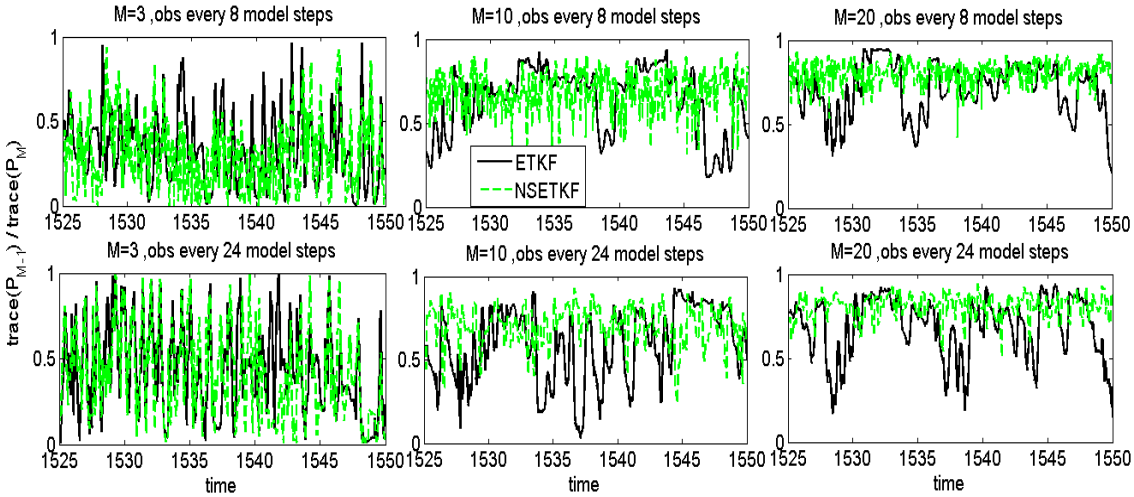

Figure 38. Time evolution of the ensemble clustering degree for LETKF (black solid line) and MPNS-ETKF (green dashed line) from an assimilation experiment with the L63 model. Three ensemble sizes (columns) are used in a linear regime (top row) and a nonlinear regime (bottom row).

Figure 39 deals in more detail with the nonlinear regime case with $M = 20$ using LETKF. Instances of set in and reversal of clustering can be identified. The top panel shows the CD evolution for a longer time period $t \in [165,200]$. There is an indication of clustering around $t = 190$. The three panels in the bottom row of this figure show the trajectories for the truth (black line) and the analysis ensemble members (gray lines) at three different instants with different CD values. The middle panels shows the case with clustering, being evident in what seems to be a two member ensemble. This, however, does not prevent the ensemble to revert the clustering afterwards. We find many episodes like this in the time evolution of the ensemble.

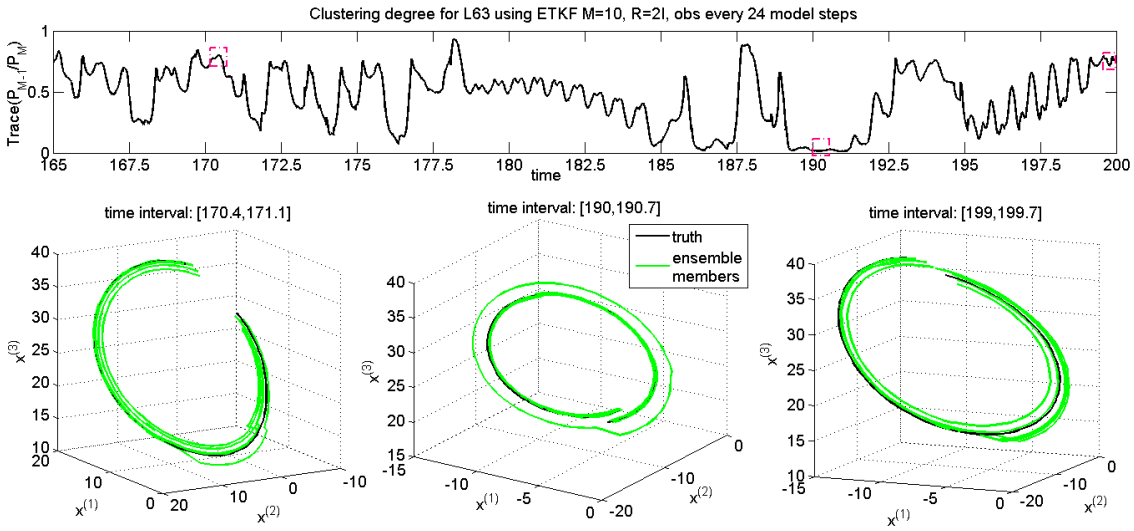

Figure 39. Experiments with L63, observations every 24 model steps and *M=3*. The evolution of the clustering degree is shown in the top. Snapshots of the phase space are presented for three time intervals with contrasting *CD* values, the one in the middle shows clustering occurring.

Why is clustering less persistent in this model? In the univariate quadratic model, clustering occurs and decays with the varying magnitude of the nonlinear expansion and contraction of the ensemble spread. In higher dimensional models, not only the

magnitude but also the direction changes temporally and spatially. A way to study the characteristics in the local perturbation growth is by using bred vectors (Toth and Kalnay, 1997). Evans *et al.* (2004) applied this technique in the Lorenz 1963 model and showed different magnitudes of growth for different regions of the attractor. In figure 41 we reproduce one of their main results. In the left panel, the attractor is depicted in phase space, the color represent the magnitude of the bred vector growth (the breeding time is 8 model steps). Dark blue represent negative values, i.e. quiescent regions where perturbations tend to vanish. All the other colors represent regions with positive growth, in particular the red color is associated with a strong growth of perturbations. Hence, as the trajectory travels by different regions of the attractor, it indeed feels changes in the magnitude and sign of growth (both linear and nonlinear). The right panels in this figure show the time evolution for the three variables. As stated in Evans *et al* (2004), the largest bred vector growth occurs near regime transitions. Zhang *et al.* (2012) have recently extended this study and have illustrated the change in direction as well.

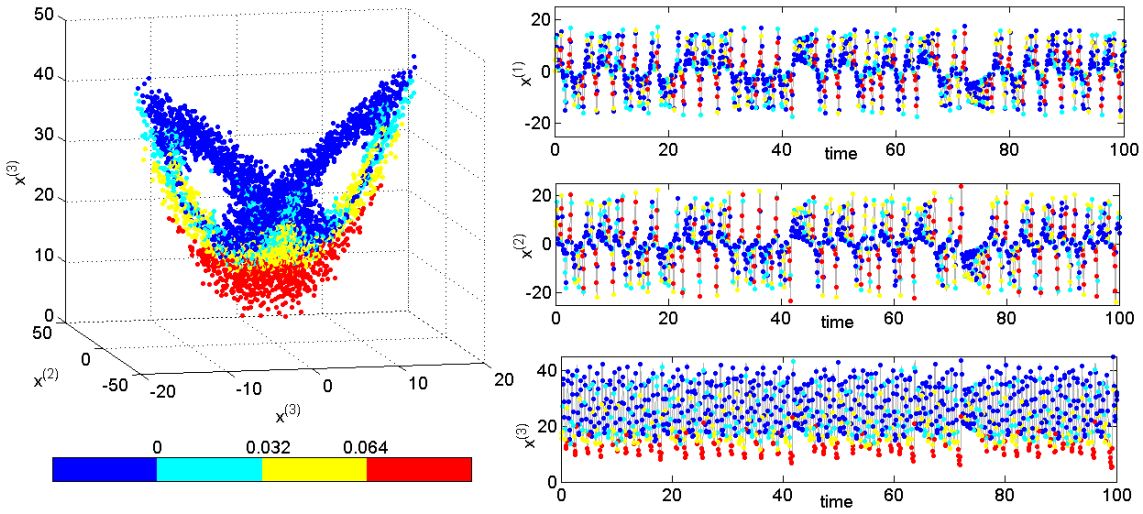

Figure 40. Bred vector growth rate in the Lorenz 1963 attractor. In the left panel, a picture of the attractor in phase space is shown. In the right three panels, the time evolution of each variable is shown colored by growth rate (reproduced from Evans *et al*, 2004).

We have presented study cases of particular instances in our experiments. A more robust statistical summary is performed now for both LETKF and MPNS-ETKF in the linear and nonlinear regimes and with different ensemble sizes; the results come from a run of 10^6 model steps after a short transient. Figure 41 shows statistical measures of both filters for the linear (left column) and nonlinear (right column) regimes, with boxplots for *CD* (top row), and analysis RMSE (right column) for the three ensemble sizes. The black dots accompanying the boxplots represent the mean for each metric; these values are also displayed in the figure. For a small ensemble size, performance of the LETKF and MPNS-ETKF is practically the same. For a larger ensemble size differences arise. The LETKF in general presents smaller *CD* values, a sign that it is more prone to clustering. For the linear regime, both for the background and analysis RMSEs have a similar distribution with little difference in the mean for the two EnSRFs. For the nonlinear regime, the MPNS-ETKF exhibits less outliers in the ensemble spread, leading to smaller mean RMSE, especially for the case $M = 20$. This is consistent with the finding by Anderson (2010) that the mean analysis RMSE of the EAKF increased for the larger ensemble size. One can hypothesize whether there is a relationship between the mean *CD* value in the forecast and the analysis RMSE in the assimilation at the end of that window. One could think, for example, that having a low *CD* value is unequivocal sign of an 'unhealthy' ensemble and that this will lead to get a large analysis RMSE. Performing a scatter plot between *CD* and RMSE (both for background and analysis) we don't find any such relationship (not shown).

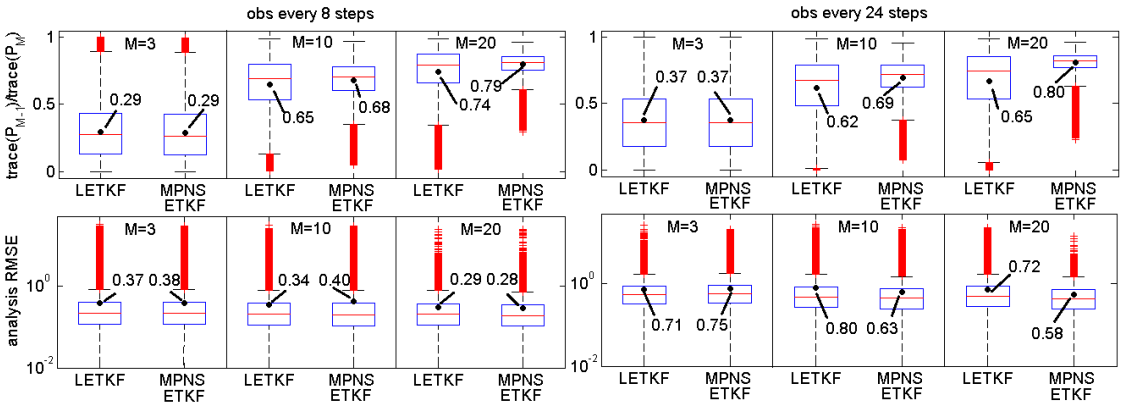

Figure 41. Boxplots for *CD* (top row) and analysis RMSE (bottom row) for both LETKF and MPNS-ETKF in the linear (left column) and nonlinear (right columns) regimes. Results are shown for three different ensemble sizes.

Finally, figure 42 presents the rank histograms for the verification of the truth with respect to the analysis ensemble for variable $x^{(1)}$ (the results are the same for the three variables). For $M = 3$ there is no difference between the EnSRFs: all ensembles are over-dispersive. This may be a result of the use of inflation. For $M = 20$, the LETKF has a U-shaped histograms, especially in the nonlinear regime. Using MPNS-ETKF, on the other hand, produces flat rank histograms; a similar behavior is observed with $M = 10$ (not shown).

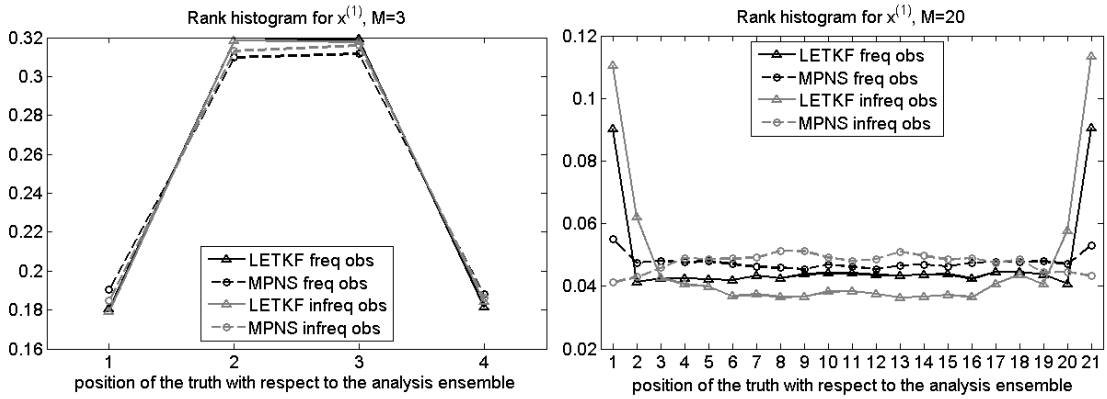

Figure 42. Rank histograms for the verification of the truth with respect to the analysis ensemble in the Lorenz 1963 model. Two different ensemble sizes are used in the linear and nonlinear regimes.

The results in this section show that MPNS-ETKF has a better performance in the nonlinear regime when $M>N$, and this difference is more evident as M grows. In practical applications, however, usually $M<<N$ and techniques such as localization and covariance inflation are needed to compensate for the limited ensemble size. This is the focus of the next subsection.

4.3.2. Experiments with SPEEDY

As for the ETKBF experiments, the nature run for our experiments starts after a one-year spin-up from state of rest and lasts two month (January and February). Both EnSRFs use an ensemble of $M=20$. The R-localization parameters are $\lambda = 500km$ in the horizontal and $\lambda_v = 0.1\ln p$ in the vertical. We use the adaptive multiplicative covariance inflation (Miyoshi, 2011). In figure 43, we compute we compute two latitude-weighted metrics – analysis[8] RMSE (left half of the figure) and sample skewness for the analysis ensemble

[8] Computing the metrics for the background ensemble lead to identical results; these are not presented.

(right half of the figure)- for the variables $\{u, v, T, q, z\}$ (one per row) at each vertical level (one per column). The mean value of the metric is indicated with a dot and the bars represent one standard deviation.

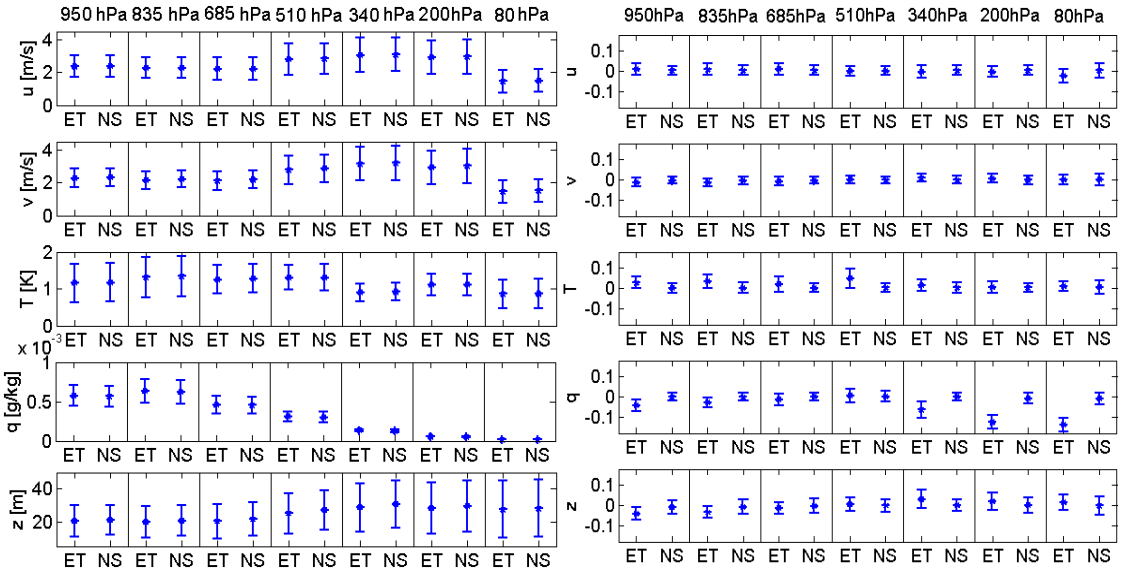

Figure 43. Latitude weighted analysis RMSE (left) and analysis skewness (right) for all variables computed globally. The bars represent one standard deviation of the metric around its mean. ET denotes LETKF and NS denotes MPNS-ETKF.

In terms of analysis RMSE, there is no perceivable difference in the performance of LETKF vs. MPNS-ETKF. In terms of skewness, we have different results for different variables. No noticeable (or very little) difference in skewness or RMSE values is observed for the variables $\{u, v, z\}$ for any vertical level. The variables $\{T, q\}$ do present differences for skewness, although the RMSE is indistinguishable. The skewness for these variables is less noticeable in the NH.

The metrics are now recomputed independently for each region of the world: NH (25N-75N), tropics (25S-25N) and SH (75S-25S). Figures 44-48 present the results for zonal

wind, meridional wind and geopotential height, i.e. those variables for which no skewed ensembles result from either method (at least globally).

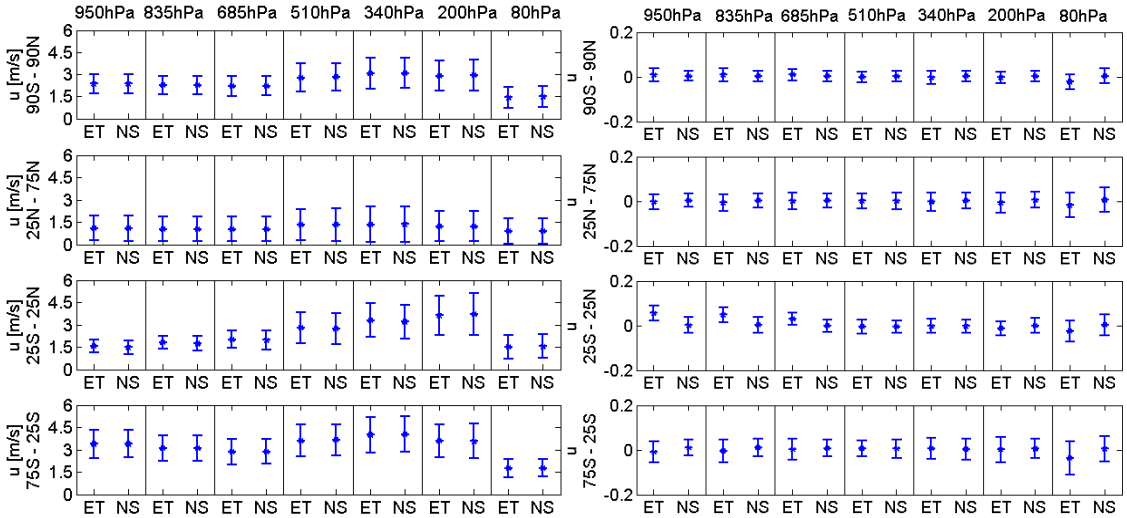

Figure 44. Latitude weighted analysis RMSE (left) and analysis skewness (right) for zonal wind computed per region (rows) for 3 vertical levels (columns) in the SPEEDY model. The bars represent one standard deviation of the metric around its mean. ET denotes LETKF and NS denotes MPNS-ETKF.

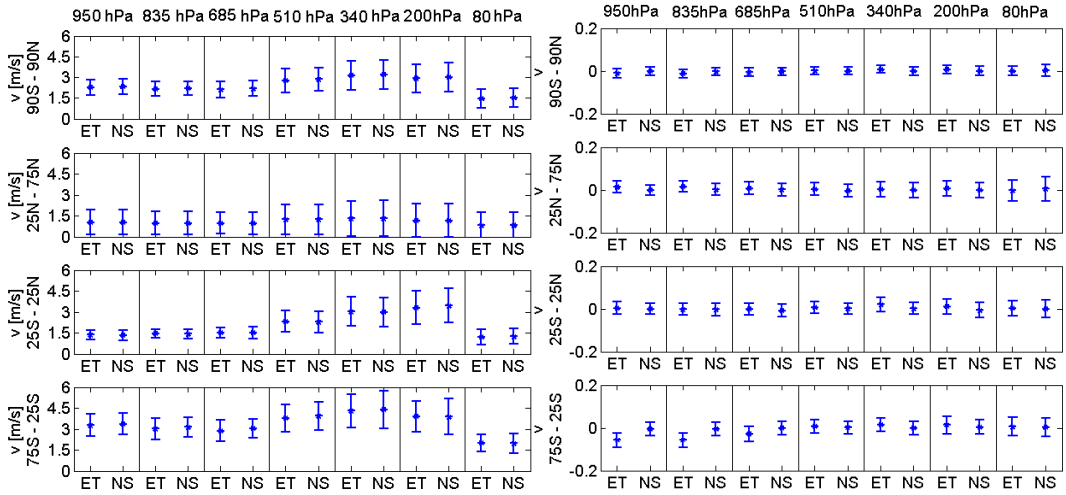

Figure 45. Latitude weighted analysis RMSE (left) and analysis skewness (right) for meridional wind computed per region (rows) for 3 vertical levels (columns) in the SPEEDY model. The bars represent one standard deviation of the metric around its mean. ET denotes LETKF and NS denotes MPNS-ETKF.

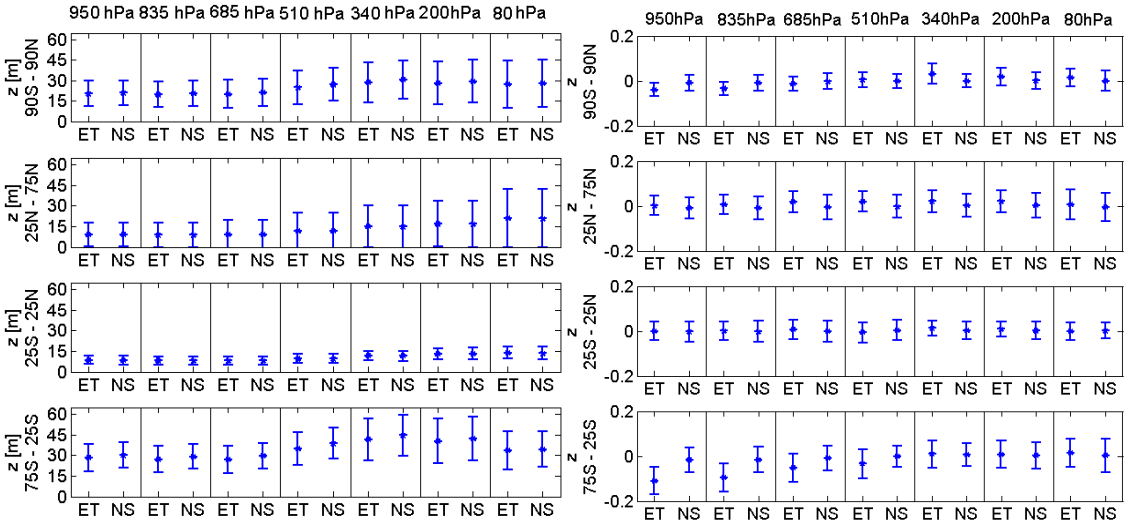

Figure 46. Latitude weighted analysis RMSE (left) and analysis skewness (right) for geopotential height computed per region (rows) for 3 vertical levels (columns) in the SPEEDY model. The bars represent one standard deviation of the metric around its mean. ET denotes LETKF and NS denotes MPNS-ETKF.

After computing the metrics per region, we observe that LETKF leads to asymetric ensembles in the tropics for *u* and in the SH for *v* and *z*. We now compute the regional metrics for *T* and *q* in figures 42 and 43. We observe that for *T*, LETKF tends to create asymetric ensembles in the tropics and in the SH. For *q*, this behavior can arise anywhere. Nonetheless, this is not reflected in the RMSE.

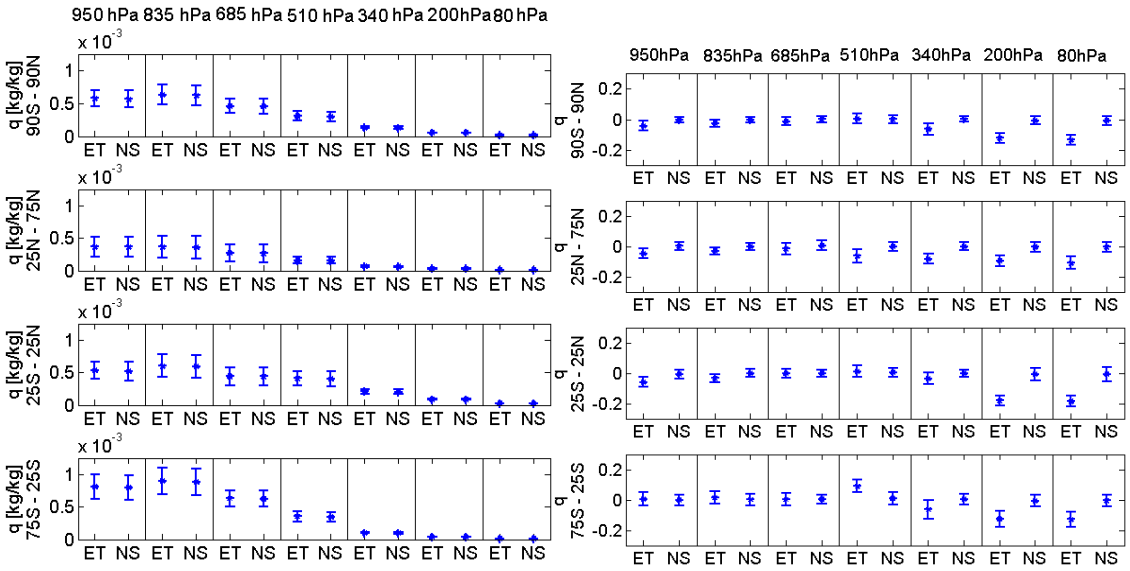

Figure 47. Latitude weighted analysis RMSE (left) and analysis skewness (right) for relative hummidity computed per region (rows) for 3 vertical levels (columns) in the SPEEDY model. The bars represent one standard deviation of the metric around its mean. ET denotes LETKF and NS denotes MPNS-ETKF.

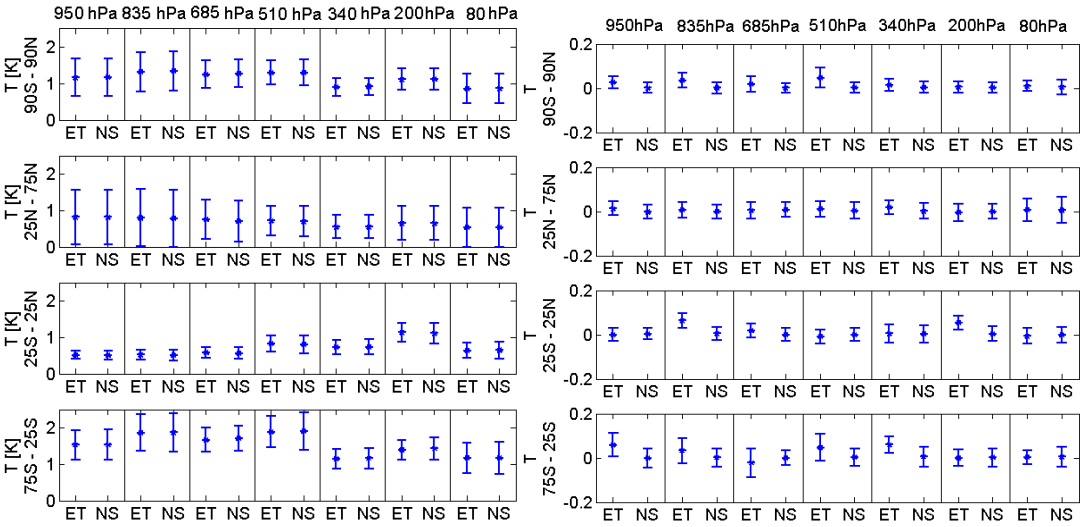

Figure 48. Latitude weighted analysis RMSE (left) and analysis skewness (right) for temperature computed per region (rows) for 3 vertical levels (columns) in the SPEEDY model. The bars represent one standard deviation of the metric around its mean. ET denotes LETKF and NS denotes MPNS-ETKF.

For most variables, LETKF tends to create asymmetric ensembles in the tropics and the SH. These are poorly observed regions in which nonlinear behavior can arise.

Nonetheless, in spite of these non-Gaussian ensembles, the analysis RMSE values show no difference between the two assimilation methods. The only variable with a different behavior is q; for this variable EC appears even in well-observed regions (NH). However, this variable is subject to nonlinear processes not represented explicitly in the model, but through parameterizations. Nonetheless, there were no specific cases in which one could observe clustering in SPEEDY.

We plot rank histograms for the verification of the truth with respect to the analysis ensemble for the variables at different pressure levels and for different regions. In particular, in the next figure we present this for temperature at 510hPa in the NH. We do not observe differences between the two methods, both lead to under-dispersive ensembles. This is a common feature for all variables.

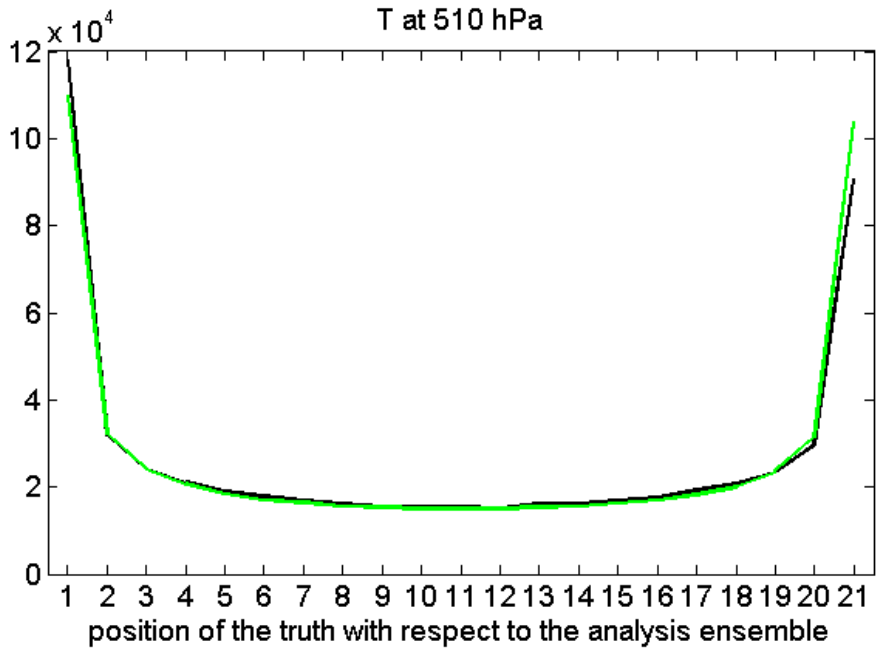

Figure 49. Verification of the truth with respect to the analysis ensemble mean for temperature at 510 hPa in the NH. The black line comes from the use of LETKF and the green line from the use of MPNS-ETKF.

5. The effects of the RAW filter on the climatology and forecast skill of the SPEEDY model

Numerical weather prediction involves the numerical time integration of prognostic equations describing the behavior of the atmosphere. A widely used option in contemporary models of the atmosphere and ocean is a centered time-stepping scheme known as the leapfrog, specifically the Robert-Asselin (RA) filtered version. This popularity is mainly due to three factors: the ease of implementation, the low computational expense (only one evaluation of the model's tendency is needed per time step), and the low run-time storage requirements. The most serious problem associated with the leapfrog scheme is the "time splitting" instability associated with the creation of a spurious computational mode. The RA filter provides a considerable amelioration of this problem. The application of this filter, however, while damping the computational mode, can also have the undesired effect of significantly damping the physical mode of the solution, hence degrading its accuracy. In recent work, Williams (2009) introduced a simple modification to the RA filter, with the objective of improving its performance while avoiding its associated problems; the modification will hereafter be referred to as the Robert-Asselin-Williams (RAW) filter.

In this chapter, the RAW filter is implemented and tested in the SPEEDY model (Molteni, 2003). Furthermore, we examine whether the use of the RAW filter changes either the climatology or the skill of weather forecasts, or both. For the first objective, we calculate the local and field significance following Livezey and Chen (1983). For the

second objective, we compute deterministic forecasts and assess the performance using base data from the NCEP reanalysis (Kalnay *et al.*, 1996).

5.1. The Robert-Asselin-Williams (RAW) filter

The centered discretization scheme known as the leapfrog is implemented as follows:

$$\frac{\partial x}{\partial t} = F(x) \qquad \Rightarrow \qquad x_{n+1} = x_{n-1} + 2\Delta t \cdot F(x_n) \tag{81}$$

The leapfrog scheme is a widely used numerical integration method, in particular for hyperbolic equations and complex models. There are two main reasons for this. First, being a centered scheme, it is reasonably accurate and has an error of order $O(\Delta t)^2$. Second, it requires only one computation of the time derivative per time step, and is therefore reasonably computationally efficient. A schematic of its design is presented in the following figure.

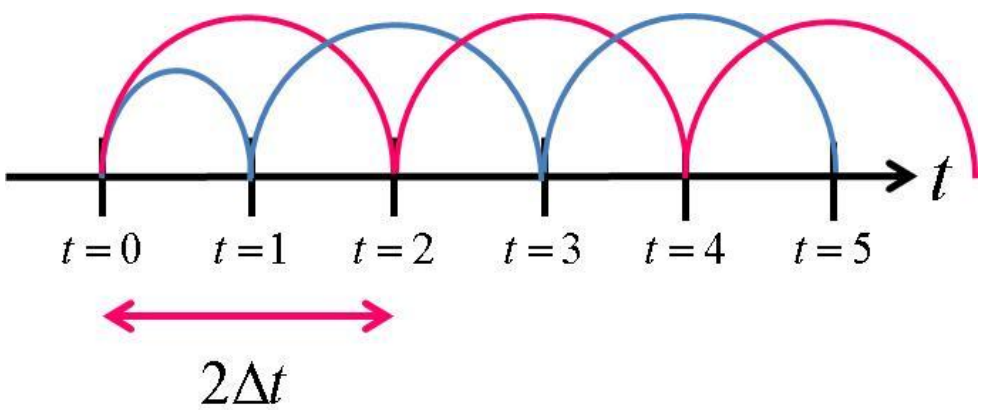

Figure 50. Schematic for the leapfrog integration method. Successive integrations are shown with an alternation of pink and blue colors. Only the first integration is an extrapolation, the rest are centered integrations.

The leapfrog scheme, however, introduces into the solution of the equation a spurious computational mode besides the actual physical mode (e.g. Kalnay 2003). This undesired mode manifests itself in nonlinear integrations as a spurious, growing oscillation between even and odd time steps. In figure 51 we present the evolution of the 510hPa geopotential height above College Park, MD, using the SPEEDY model. The black line represents the leapfrog integration without any filtering. The appearance of the computational mode is evident since early stages; the bottom panel shows the spurious oscillations after 8 days of integration. The growth of these unphysical modes leads to very rapid variations of the function after a little over a month of integration. The function loses its smoothness progressively and this leads eventually to 'computational blowup'.

Several approaches have been proposed to combat the growth of the computational mode; the most widely used is the Robert-Asselin (RA) filter. This filter was introduced by Robert (1966) and was shown by Asselin (1972) to suppress the computational mode while leaving the physical mode untouched for low frequencies with long periods compared to the time step, Δt. The RA filter is implemented in leapfrog integrations as follows:

$$\begin{aligned} x_{n+1} &= \bar{x}_{n-1} + 2\Delta t \cdot F(x_n) \\ \bar{x}_n &= x_n + \frac{\nu}{2}\left[x_{n+1} - 2x_n + \bar{x}_{n-1}\right] \end{aligned} \tag{82}$$

The smoothing parameter ν in equation is usually chosen to be $O(0.01-0.2)$. The choice of this parameter is important: if its value is too small it can hardly manage to dampen the computational mode, but if it is too large it can lead to loss of accuracy in the

solution. In his original analysis, Asselin (1972) studied values up to $\nu = 0.2$. For atmospheric models, Durran (1991) notes that values of $\nu = 0.12$ are typically used in the NCAR community (Williamson, 1983); Déqué and Cariolle (1986) consider values as high as $\nu = 0.2$ and so does the GFDL-MOM model. For oceanic models Khanta and Clayson (2000) recommend values between $\nu = 0.1$ and $\nu = 0.3$.

In figure 51, the RA-filtered leapfrog is represented with the red line; it is evident that the spurious gravity waves are damped satisfactorily. Although the RA filter is widely used in operational and research models of the atmosphere and ocean (Williams, 2009), it has two related problems. First, besides damping the computational mode, the filter also weakly damps the physical mode, especially at high frequencies. This damping may become important for long integrations. Second, the RA filter degrades the accuracy of the unadulterated leapfrog scheme, since, by being un-centered in time, the RA-filtered leapfrog is only first-order accurate.

In order to ameliorate the negative effects that the RA filter has on the physical solution of the model, Williams (2009) introduced a modification that we hereafter refer to as the Robert-Asselin-Williams (RAW) filter. The original RA filter reduces, by a factor of $(1-\nu)$, the magnitude of the temporal curvature of the state, and it is this smoothing effect that damps the computational mode. However, the filtering also changes the mean value of the state, averaged over the three time levels:

$$M = \frac{x_{n+1} + x_n + \bar{x}_{n-1}}{3} \neq \frac{x_{n+1} + \bar{x}_n + \bar{x}_{n-1}}{3} \tag{83}$$

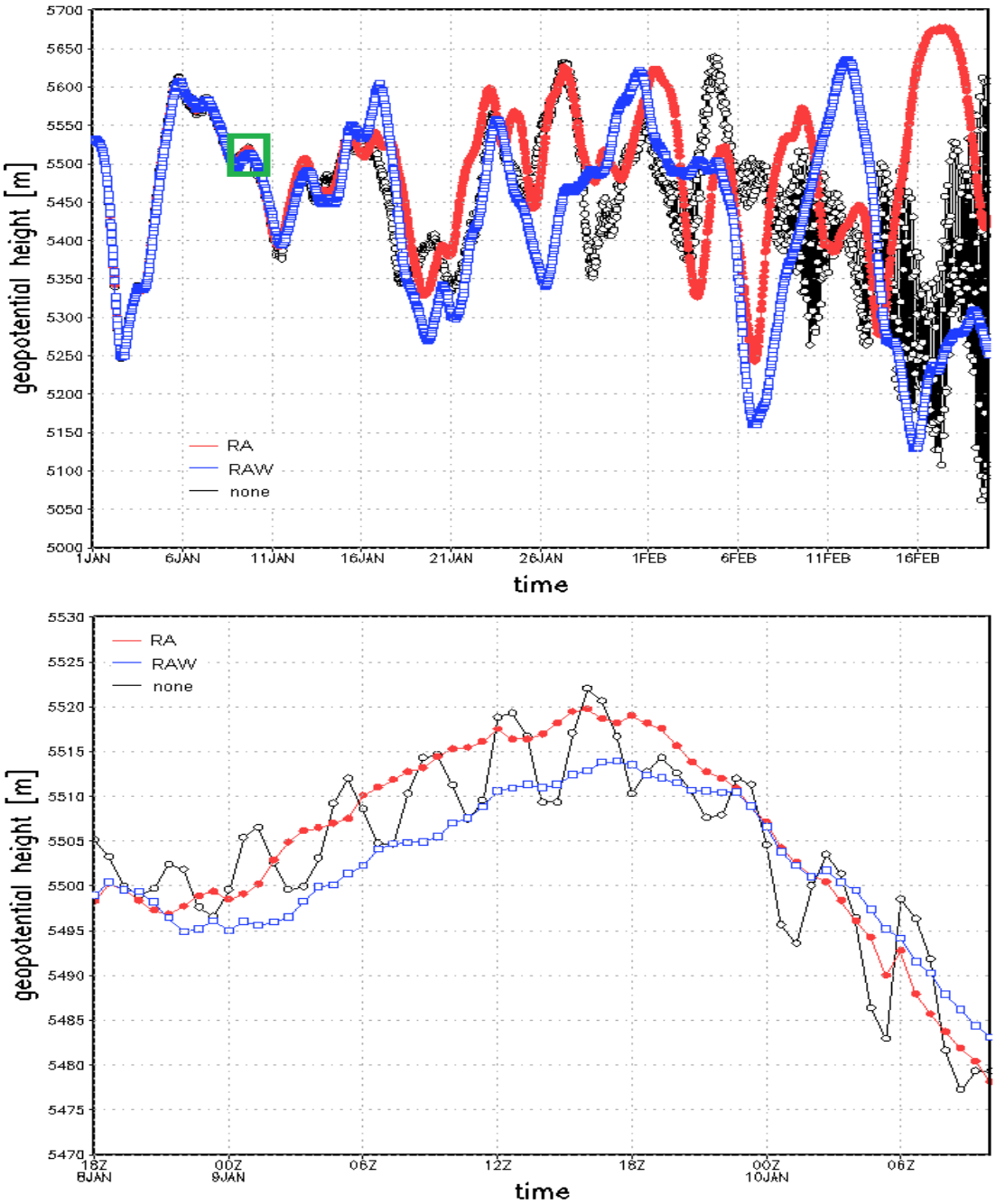

Figure 51. Time evolution of the 510hPa-geopotential height over College Park, MD using the SPEEDY model. The integration is performed using the leapfrog scheme using no filter (black line), the RA filter (red line) and the RAW filter (blue line).The appearance of spurious computational waves in the unfiltered integration occurs quickly (bottom panel) and leads to the loss of smoothness in the solution after a little over a month (top panel).

Williams (2009) showed that, when used with the leapfrog scheme, it is this non-mean-conserving feature of the filter that degrades the numerical accuracy. In the same work, the author tackled this problem by introducing an extra step in the filtering process, in order to include the possibility of conserving the mean value. The resulting RAW filter is implemented in leapfrog integrations as follows:

$$
\begin{aligned}
x_{n+1} &= \bar{\bar{x}}_{n-1} + 2\Delta t \cdot F\left(\bar{x}_n\right) \\
\bar{\bar{x}}_n &= \bar{x}_n + \frac{\nu\alpha}{2}\left[x_{n+1} - 2\bar{x}_n + \bar{\bar{x}}_{n-1}\right] \\
\bar{x}_{n+1} &= x_{n+1} - \frac{\nu(1-\alpha)}{2}\left[x_{n+1} - 2\bar{x}_n + \bar{\bar{x}}_{n-1}\right]
\end{aligned}
\tag{84}
$$

In figure 51, the RAW-filtered leapfrog integration is represented with the blue line. Like the RA filter, the computational mode is damped satisfactorily. The RAW filter introduces an extra operation which is simple and doesn't represent a considerable computational expense with respect to the RA filter. It also introduces a new parameter, $\alpha \in [0,1]$. Taking an un-damped oscillation equation $\frac{dF}{dt} = i\omega F$, Williams (2009) found the amplification relationship for the RAW filter to be:

$$
\begin{aligned}
A_{\pm}(\alpha, \upsilon, \omega\Delta t) = \frac{\nu}{2} + \left[1 - \frac{\nu(1-\alpha)}{2}\right] i\omega\Delta t \\
\pm\sqrt{\left(1-\frac{\nu}{2}\right)^2 - \left[1 - \frac{\nu(1-\alpha)}{2}\right]^2 (\omega\Delta t)^2 + \nu\left(1-\frac{\nu}{2}\right)(1-\alpha) i\omega\Delta t}
\end{aligned}
\tag{85}
$$

In this amplification relation , Δt corresponds to the time step of the numerical solution of the equation. The next figure (taken from Williams, 2009) illustrates the behavior of equation –for a fixed value of ν (taken to be 0.2)- with respect to $\omega\Delta t$.

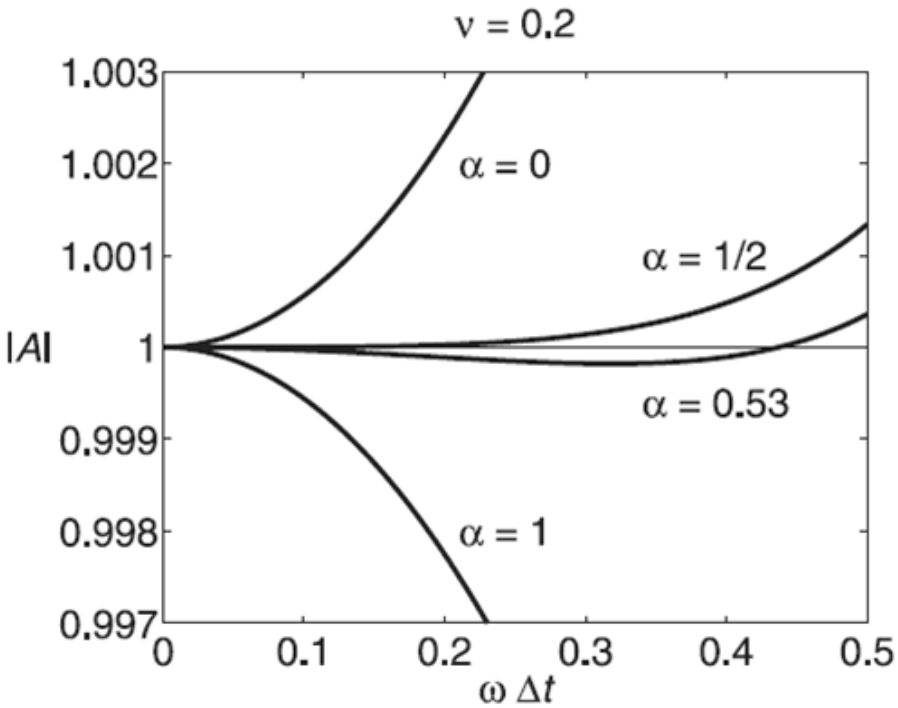

Figure 52. The impacts of different values of the parameter α of the RAW filter on the numerical amplification of an unforced, undamped wave; taken from Williams (2009). The value of $\alpha = 1$ corresponds to the original RA filter. The value of $\alpha = 0.53$ is a preferred choice, since it keeps the amplification close to its exact value (unity) over a broad frequency range.

Each curve illustrates the effect of a different value of α on the numerical amplification (or numerical dissipation) of a free wave oscillation, which is physically unforced and undamped in the time-continuous differential equation. A value of $\alpha = 1$ corresponds to the traditional RA filter. From this figure we can see that, for a value of $\alpha = 0.53$ one can minimize the spurious, numerical impacts on the physical solution and obtain the closest match to the exact solution over a broad frequency range.

In Williams (2009), the RAW filter was tested in a simple linear system representing harmonic inertial oscillations. For this model, an explicit analytical solution exists and therefore it is easy to visualize and compare the effects of both the RA filter and the

RAW filter in the numerical solution of the model. In this work we implement and test the RAW filter in a more realistic atmospheric model, the SPEEDY model described in section 2.2.3.

We have been using figure 52 to illustrate the effectiveness of the RA and RAW filter in suppressing the unphysical modes for a variable of this model. One can appreciate that the RA- and RAW-filtered integrations differ after around 13 days even when they started from the same initial conditions. This is understandable since the model is chaotic, so the chance in integration scheme will cause the divergence of trajectories eventually. So, in order to assess the true impact of upgrading the RA filter to the RAW filter, we will have to assess if there are changes in the climatology of the model, and whether forecasts coming from RAW-filtered integrations are more accurate.

5.2. Effects of the RAW filter on the climatology of the SPEEDY model

Since we are interested in possible changes to the climatology of the model, in this section we consider relatively long time averages for our variables. In order to strike a balance between retaining long averages and avoiding the effects of seasonality, we choose to focus on monthly averages. We will take the variables separately at each of the seven pressure levels For example, we will consider the mean 510hPa geopotential height for March, denoted $z510_{mar}$, and the mean 200hPa temperature for September, denoted $T200_{sep}$. Surface pressure and precipitation are two-dimensional fields without vertical dependence. Taking into consideration the previous specifications, we will have 37 variables for each month of the year, giving 444 variables in total.

For each one of the 444 variables, we will look for differences between the climatology generated by the RAW filter and the climatology generated by the RA filter. Hence, we can write our null hypothesis as $\overline{x_{month,RA}} = \overline{x_{month,RAW}}$ and our alternative hypothesis as $\overline{x_{month,RA}} \neq \overline{x_{month,RAW}}$, where the second subscript indicates the time-stepping method by which the variable was generated.

To generate our climatology, we run the model for $N_{years} = 8$ years, and for each filter scheme separately. For each year we compute the monthly means. Since the value of the temporal autocorrelation of the monthly means from one year to the next is very low, it is acceptable to neglect it when computing the statistics. If our variables were daily values instead of monthly averages, then we would surely need to consider this temporal autocorrelation and use a more suitable method, such as the moving blocks bootstrap proposed by Elmore et al. (2006).

5.2.1. Local significance

It is important to distinguish between local variations and field variations. For the former case, we test the null hypothesis for each variable at each vertical level and at each point on the 96 by 48 grid. The result for each grid point represents the *local significance* (Livezey and Chen, 1983). For the latter case, the way in which we take into consideration the set of results for all the grid points of a variable determines the *field significance* (Livezey and Chen, 1983), as described in the following subsection.

To test the null hypothesis in the local context, we perform the Satterthwaite-Welch (SW) version of the t-test. This test requires the data to come from normal distributions, allows small samples, and permits the two groups compared to have different variances. The test statistic is:

$$t_{month} = \frac{\bar{x}_{RA,month} - \bar{x}_{RAW,month}}{\sqrt{\frac{s^2_{RA,month}}{N_{years}} + \frac{s^2_{RAW,month}}{N_{years}}}} \tag{86}$$

In the previous equation, $\bar{x}$ represents the inter-annual mean and s^2 represents the inter-annual variance.. The statistic has a t distribution with *f* degrees of freedom, this number is calculated as indicated next:

$$f = \frac{\left(\frac{s^2_{RA,month}}{N_{years}} + \frac{s^2_{RAW,month}}{N_{years}}\right)^2}{\frac{\left(\frac{s^2_{RA,month}}{N_{years}}\right)^2}{N_{years}-1} + \frac{\left(\frac{s^2_{RAW,month}}{N_{years}}\right)^2}{N_{years}-1}} \tag{87}$$

This expression for the ‘effective’ number of degrees of freedom is the main difference of the SW t-test from the standard t-test.

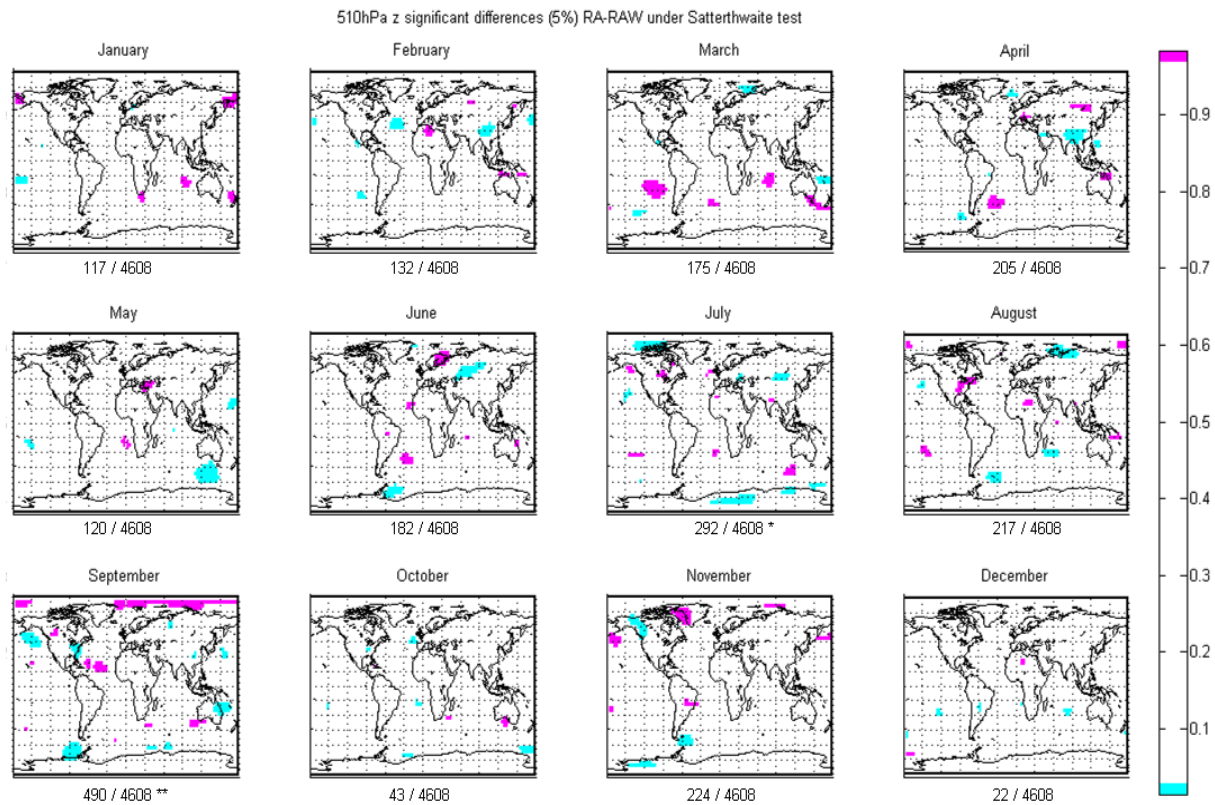

Figure 53. Results of applying the t-test for difference of means in the variables $z510$ for each month with a local significance $\alpha_{local} = 0.05$. Under each map we indicate the number of grid points that resulted locally significant out of the 96x48 grid. One asterisk denotes that the variable is field significant ($\alpha_{field} = 0.05$) considering finite sample size, and two asterisks denote that it is field significant considering both finite sample size and spatial correlation. Only the month of September is field significant.

We perform the two-tailed version of the SW t-test on all our variables, using a significance level of $\alpha_{local} = 0.05$. (Note our use of a subscript here, to distinguish this variable name from the un-subscripted α used in equation 4 for the RAW filter.) Figure 53 presents the results for the variable $z510$ (i.e. the 510hPa geopotential height) for every month of the year. For the maps shown in this figure, we color in blue the points with $p \leq 0.025$ and in pink those with $p \geq 0.975$. Hence, the pink regions are grid points

at which the climatology generated by the RAW filter has significantly smaller values than the climatology generated by the RA filter, while the blue regions are grid points at which the climatology generated by the RAW filter has significantly larger values than the climatology generated by the RA filter.

In figure 53 we see no preferred regions for the significant points, but they are instead scattered around the globe without coherency from one month to the next. This is true not only for this variable but for the others too (not shown). Moreover, since we are performing the same test in each grid point, some of the tests can be passed just by chance. This is called the "multiplicity problem" by Wilks (2005) and can lead to erroneous conclusions. One has to ask the following question (Livezey and Chen 1983): What is the minimum number of tests (out of the 96x48) that must be passed in order to achieve some desired field significance α_{field}?

5.2.2. Field significance

As indicated above, one must look at the results together in a 'field' sense. In order to obtain this field significance, two effects must be taken into consideration (Livezey and Chen 1983). The first is finite sample size. We are performing the significance test at each of the $M = 96 \times 48$ grid points of the model. Each test may be regarded as a Bernoulli trial with a probability of success equal to the significance of the local t-test, $\alpha_{local} = 0.05$. For the moment, let us assume that each of the M trials is independent from each of the others. Then we can regard the total number of tests passed as a random

variable from a binomial distribution with a total of $M = 96 \times 48$ trials and an individual probability of success of $\alpha_{local} = 0.05$.

The mass probability function and the cumulative probability density function for this discrete binomial distribution are shown in the next figure:

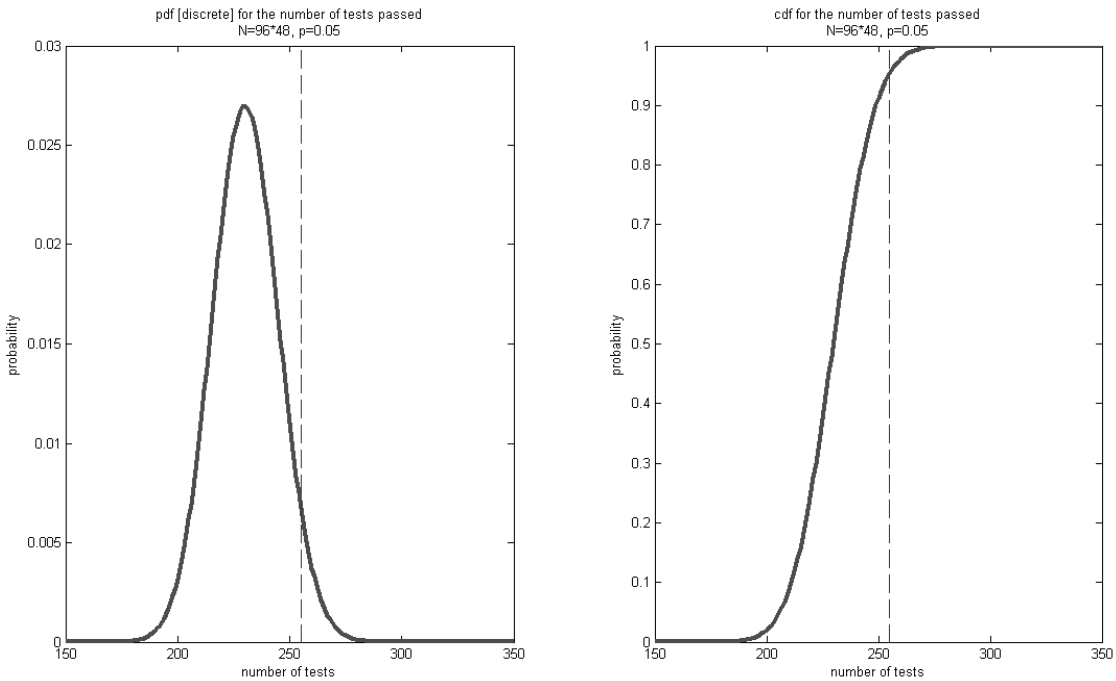

Figure 54. Probability mass function (left) and cumulative probability function (right) for the binomial distribution representing the total number of local significance tests passed (assuming independence). For a total of 96x48 tests of local significance $\alpha_{local} = 0.05$, at least 255 must be passed in order to achieve a field significance $\alpha_{field} = 0.05$.

The distribution is centered on 5% of 96x48 tests, i.e. 230.4 tests. In order to have a field significance of $\alpha_{local} = 0.05$, the minimum number of tests that must be passed corresponds to the $100 \times (1 - \alpha_{field})$'th percentile of this binomial distribution. Therefore, if we choose the field significance to be $\alpha_{field} = 0.05$, then at least $m_0 = 255$ tests must be

passed. Let us see how many variables fulfill the requirement to be field significant at the level $\alpha_{field} = 0.05$. For each of the 2+5x7=37 variables and each of the 12 months, the next table shows the number of points at which the t-test was passed, i.e. the number of points that were locally significant.

m_0		u							v							T						
255	***390***	950	835	685	510	340	200	80	950	835	685	510	340	200	80	950	835	685	510	340	200	80
Jan		96	98	112	120	190	190	**305**	138	164	198	221	**268**	**307**	**351**	138	164	198	221	**268**	**307**	**351**
Feb		140	157	203	219	245	226	198	163	173	191	186	199	**261**	**310**	163	173	191	186	199	**261**	**310**
Mar		**269**	229	243	**265**	223	186	127	239	**256**	**274**	**256**	247	213	226	239	**256**	**274**	**256**	247	213	226
Apr		**306**	**319**	**294**	**268**	231	210	198	162	188	152	203	213	228	**290**	162	188	152	203	213	228	**290**
May		210	213	217	183	164	146	113	240	239	248	**276**	**280**	241	**264**	240	239	248	**276**	**280**	241	**264**
Jun		227	230	231	**263**	**256**	**267**	232	**264**	**258**	**290**	**301**	**293**	253	242	**264**	**258**	**290**	**301**	**293**	253	242
Jul		**350**	**348**	**349**	***403***	***396***	***400***	**342**	**255**	**259**	246	245	230	146	182	**255**	**259**	246	245	230	146	182
Aug		**328**	**316**	248	**264**	251	153	116	254	**262**	245	208	176	181	214	254	**262**	245	208	176	181	214
Sep		**346**	**383**	**376**	***393***	**337**	**337**	**297**	248	**270**	**278**	**301**	**276**	243	234	248	**270**	**278**	**301**	**276**	243	234
Oct		120	103	113	91	115	116	65	161	192	180	141	108	83	71	161	192	180	141	108	83	71
Nov		**276**	247	**255**	**266**	239	196	154	**305**	**345**	**314**	**294**	216	185	180	**305**	**345**	**314**	**294**	216	185	180
Dec		122	106	106	93	119	105	61	166	174	175	143	113	74	55	166	174	175	143	113	74	55

m_0		q							z							ps	prec
255	***390***	950	835	685	510	340	200	80	950	835	685	510	340	200	80		
Jan		202	160	135	126	114	130	133	121	103	84	117	153	146	181	57	118
Feb		227	**257**	248	226	180	230	207	139	95	99	132	119	88	49	38	195
Mar		221	188	216	205	**292**	232	201	188	180	167	175	166	130	67	40	185
Apr		158	149	145	177	216	198	204	231	233	215	205	153	125	191	63	**263**
May		**300**	252	**274**	**339**	209	124	119	91	96	102	120	159	154	100	65	84
Jun		**288**	**285**	**315**	221	243	179	176	84	93	130	182	194	174	143	95	80
Jul		247	225	**277**	**255**	164	170	158	175	174	179	**292**	**308**	163	135	62	198
Aug		**327**	**289**	**318**	251	165	164	176	241	241	211	217	**380**	**348**	135	67	246
Sep		**308**	**310**	**323**	174	246	182	202	**361**	**376**	***430***	***490***	***425***	***408***	**304**	45	**349**
Oct		154	136	135	140	176	215	204	60	40	42	43	78	100	88	45	45
Nov		227	209	172	125	181	194	187	**269**	**280**	**282**	224	148	112	69	46	**261**
Dec		136	103	102	94	175	227	157	2	3	2	22	45	37	61	65	4

Table 3. For each one of the variables, this table presents the number of grid points (out of 96x48) that resulted locally significant $\alpha_{local} = 0.05$ after applying the t-test. The variables that result field significant with a value of $\alpha_{field} = 0.05$ are presented bolded if they are field significant considering only finite sample size [and independence], and they are also presented in italics (besides the bolding) if they are field significant considering both finite sample size and spatial correlation.

Considering the finite sample size effect, 119 out of the 444 variables are field significant. In the table, these variables are bolded. The month with the most field significant variables is September, with 26 out of 37 variables. There is apparently no preferred pressure level or variable for the field significance to appear.

Given only the above analysis, we would lean towards concluding that the RAW filter is indeed changing the climatology of the SPEEDY model for a considerable number of variables. However, a second effect must be taken into consideration: spatial correlation. When considering the total number of tests locally passed as a binomial distribution, we had to assume that the tests were independent from each other. That is, we considered that the result of a t-test in a given grid point would not affect the result of the test in the surrounding grid points. We now improve this analysis by replacing the binomial distribution with a null empiric distribution in which the spatial correlation is embedded. A way to construct this distribution is Monte Carlo simulation. Elmore (2006) describes how to generate the distribution by correlating random numbers with the data for each one of the variables for a number of trials. We selected this number of trials to be 1000.

Figure 55 shows the results of generating these empirical distributions for $z510_{mar}$, $T200_{sep}$, $v835_{jul}$, and $u950_{ago}$. we generated the empirical distributions only for those variables that had resulted field significant. One can immediately notice that these empirical distributions are substantially broader than the corresponding binomial distribution, having considerably heavier tails. For each variable, the shape of the distribution will be unique, since it contains the particular information of the spatial

correlation for that variable. They are all, however, expected to present a qualitative similarity, since there is a common pattern of spatial interdependence for all the variables. For our purposes (evaluating the field significance of the individual t-tests), we will be particularly interested in the upper tail of each of the distributions.

As one can see from this figure –and as previously noted by Livezey (1983) and Elmore (2006) – spatial correlation makes it more difficult to achieve the same level of field significance. The minimum number of local tests required to be passed is larger than with the binomial distribution. With the field significance level we had selected, $\alpha_{field} = 0.05$, the minimum number of tests that must be passed under independence is 255, whereas for the empirical distributions, the minimum numbers of tests are considerably larger.

Table 4 shows these numbers for the four variables under consideration. Considering more than just the four variables in the table, the new minimum number of tests required to be passed ranges from around 380 to 530.

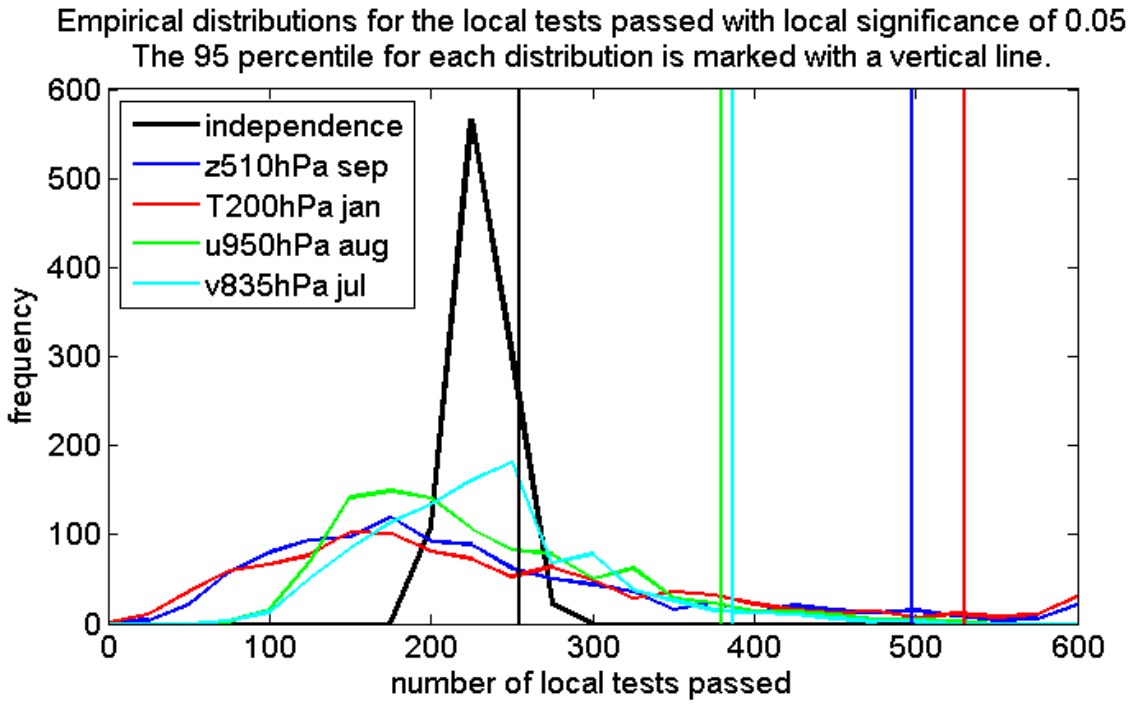

Figure 55. Distribution of the total number of local significance tests passed. The binomial distribution (black line) corresponds to the assumption of field independence. The empirical distributions (color lines), which consider the spatial correlation, are shown for four variables. These distributions were constructed via Monte Carlo simulation with 1000 iterations. The vertical lines indicate the 95th percentile for each distribution. It is noticeable that these values are substantially higher than the value of 255 (associated with the binomial distribution) appropriate for the spatially correlated variables.

Variable	**Minimum number of locally significant points**
Any variable under spatial independence	255
$z510_{mar}$	498
$T200_{sep}$	531
$v835_{jul}$	387
$u950_{aug}$	380

Table 4. Minimum number of tests (out of 96x48) to be passed with a local significance $\alpha_{local} = 0.05$ to achieve a field significance $\alpha_{field} = 0.05$.

Let us conservatively consider one of the smallest of these numbers (380) as our minimum number of local tests required to be passed in order to achieve the field

significance $\alpha_{field} = 0.05$, and let us reconsider the results of table 1. After considering the effect of spatial correlation, only 8 out of the 444 variables are field significant at $\alpha_{field} = 0.05$. That is, only 1.8% of the variables suffered a significant change. These variables are identified in table 3 with italics (in addition to the previous bolding). This is clearly a huge reduction from the 119 field significant variables we had obtained under the assumption of independence.

Hence, considering spatial correlation, we conclude that there is no evidence to support the hypothesis that the climatology of the SPEEDY model generated by integrating with the RAW filter is different from that generated by integrating with the RA filter. This is an advantageous finding, in the sense that the new scheme does not require a retuning of the parameterized physics.

5.3. Effects of the RAW filter on the skill of short term and medium term forecasts

Since the climatology of the SPEEDY model is unchanged by the introduction of the new filter, we can now proceed to answer the question of accuracy: Are solutions obtained with the RAW filter more accurate than solutions obtained with the RA filter?

In order to assess any possible change in accuracy, we use the Anomaly Correlation Coefficient (ACC) for h-hour forecasts. This is computated for the month of January 1982. For the analysis data, we use the NCEP Reanalysis dataset interpolated onto the

SPEEDY grid[9]. Every 6 hours we take the reanalysis values an initial conditions to generate *h*-hour forecasts - $h = \{24,48\ldots144\}$-, which are later verified with respect to the reanalysis values. This is depicted schematically in the following figure:

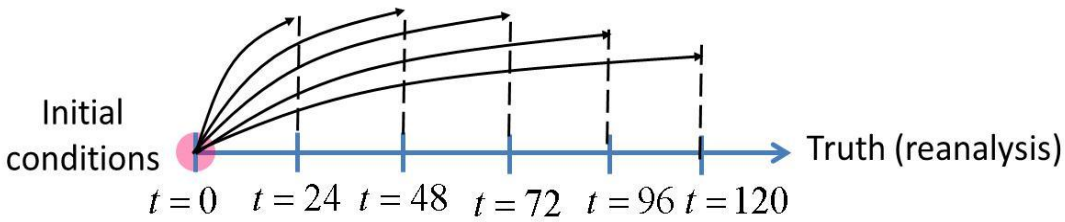

Figure 56. Schematic depicting the experiment to assess the impact of the RAW filter in the accuracy forecasts. Starting from an initial condition coming from the NCEP reanalysis, *h*-hour forecasts are generated which later are verified using the ACC metric.

The ACC is a measure of the agreement between the spatial variations in the forecast and the analysis, each with respect to the climatology. The ACC is calculated using

$$ACC = \frac{\sum_{i=1}^{N}\left[(f_i - cs_i)(a_i - cr_i)\cos\varphi_i\right]}{\sqrt{\sum_{i=1}^{N}\left[(f_i - cs_i)^2\cos\varphi_i\right]\sum_{i=1}^{N}\left[(a_i - cr_i)^2\cos\varphi_i\right]}}, \tag{88}$$

where f_i is the forecast, a_i is the analysis, cr_i is the climatology of the analysis, cs_i is the climatology of the SPEEDY model, φ_i is the latitude and N is the total number of grid points for the variable. Note that we use the SPEEDY model's own climatology rather than the reanalysis climatology to define forecast anomalies, because the SPEEDY model has resolution much lower than operational forecast models, and hence larger climatological errors. The subscript i labels the points on the grid. The climatology of

[9] Dr. Hong Li is gratefully acknowledged for providing the NCEP reanalysis data already interpolated onto the grid of the SPEEDY model

SPEEDY is computed from the eight-year runs for the RA filter and the RAW filter. Following the conclusion from section 3, we compute the climatology as follows:

$$\overline{x_{JAN}} = \left(\overline{x_{JAN,RA}} + \overline{x_{JAN,RAW}}\right)/2$$

We select 3 of the 7 vertical levels of the model, representing roughly the upper atmosphere (200 hPa), the middle atmosphere (510 hPa), and the lower atmosphere (835 hPa). The ACC analysis is performed for the model variables (u, v, T, q, z) in each of the above levels, and it is also computed for the surface variable ps.

The ACC analysis is first performed globally. The results for the five variables (excluding ps) are presented in the next figure, which displays the differences $\overline{ACC_{RAW}} - \overline{ACC_{RA}}$. There is a clear, general improvement due to the use of the RAW filter, and the improvements are around $O\left(10^{-3}\right)$ in magnitude. The improvement increases with lead time and is more important for medium-term forecasts with lead times of 96, 120, and 144 hours. The variables that benefit most from the RAW filter are z and v, while q is the only variable that has no apparent improvement. There are almost no cases where the difference $\overline{ACC_{RAW}} - \overline{ACC_{RA}}$ is negative.

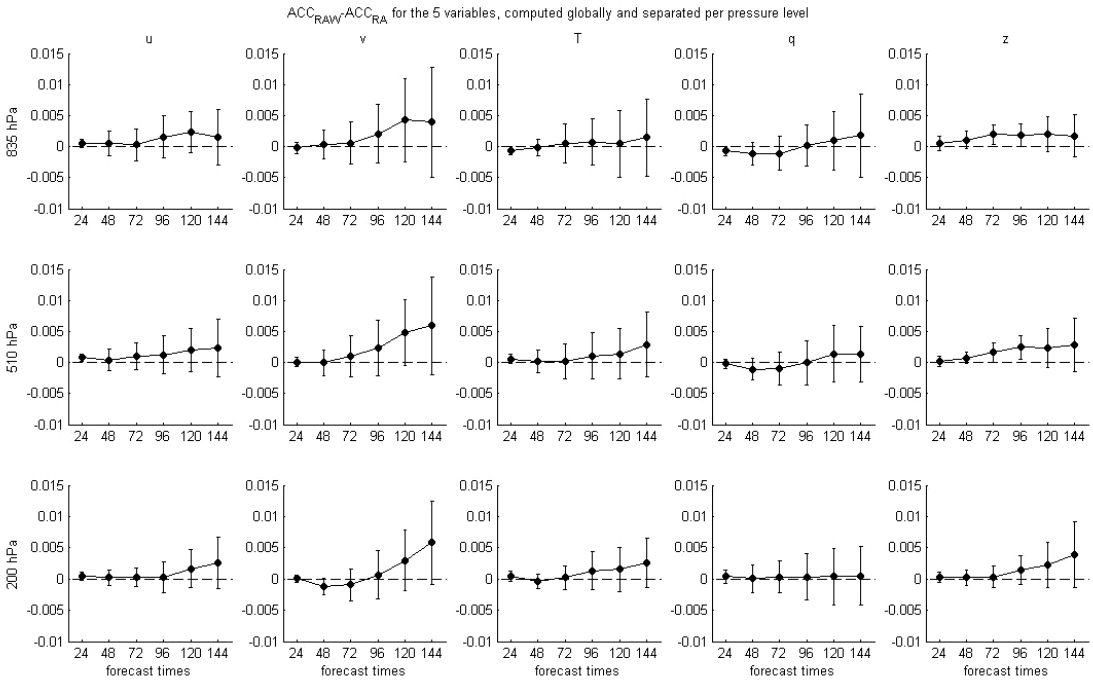

Figure 57. Increase in anomaly correlation coefficient ($\overline{ACC_{RAW}} - \overline{ACC_{RA}}$) for six different forecast times. The values were computed globally, for three different pressure levels, and for each of the five variables. The most benefited variables are the meridional wind and the geopotential height. The bars denote one standard deviation of the difference.

To examine regional differences, we finally perform the ACC analysis for three latitudinal bands: the tropics, defined by 25°S to 25°N, the northern hemisphere mid-latitudes, defined by 25°N to 75°N, and the southern hemisphere mid-latitudes, defined by 75°S to 25°S. The next figure shows the results for the two variables that were globally most benefited by the RAW filter: the geopotential height and meridional wind.

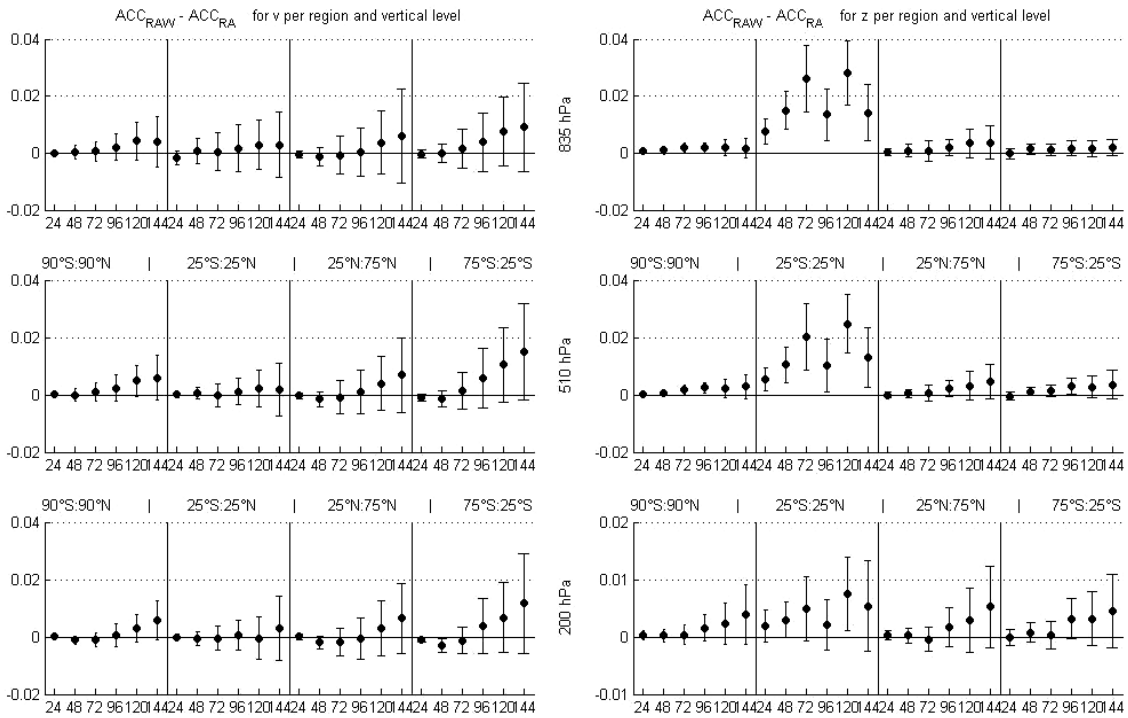

Figure 58. Increase in anomaly correlation coefficient ($\overline{ACC_{RAW}} - \overline{ACC_{RA}}$) for six different forecast times for two variables (geopotential height and meridional wind) at three pressure levels and four different latitudinal bands. The bars denote one standard deviation of the difference.

For the geopotential height, z, the largest improvements in the ACC occur in the tropics. Moreover, the improvements start to be noticeable in the 72-hour forecast, which is earlier than for the other variables. The difference, $\overline{ACC_{RAW}} - \overline{ACC_{RA}}$, which is of the order of $+0.02$ for medium-range forecasts, is larger for this variable and region than for any other. Results are similar for the surface pressure, ps (not shown). These improvements in the skill of medium-range forecasts, which arise directly from the upgrade to the RAW filter, increase the anomaly correlation coefficient for surface pressure (and 500hPa geopotential height) in the tropics by 10-20%, as seen in the next figure. As a consequence, five-day forecasts made using the RAW filter have approximately the same skill as four-day forecasts made using the RA filter, and four-day

forecasts made using the RAW filter have approximately the same skill as three-day forecasts made using the RA filter.

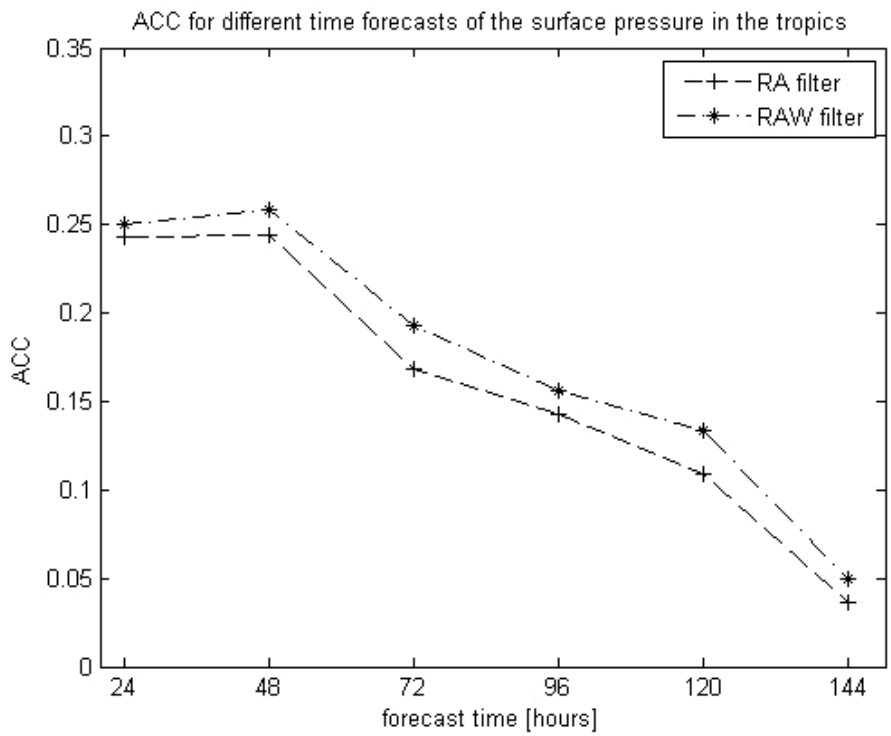

Figure 59. Anomaly Correlation Coefficient for forecasts of surface pressure in the tropics. Notice that 96-hour forecasts using the RAW filter have approximately the same skill as 72-hour forecasts using the RA filter. Also, 120 hour forecasts using the RAW filter have approximately the same skill as 96-hour forecasts using the RA filter.

For the meridional wind, v, the largest improvements in the ACC occur outside the tropics, in the three levels of the atmosphere, and they are more noticeable as the forecast time increases. The improvements in the temperature, T (not shown), are very similar to those for v, with the largest values occurring in the northern hemisphere and especially in the middle atmosphere. For the zonal wind, u (not shown), there is a moderate improvement for the medium term forecasts, but it is not as striking as for the previously

listed variables, and the improvement never exceeds 0.005. For the relative humidity, q (not shown), we consistently get an improvement close to zero.

In order to complement the ACC analysis, an additional Root Mean Square Error (RMSE) analysis is performed. This statistic doesn't involve the climatology; instead it compares directly the forecast (generated by integrating with any of the two filters) with the reanalysis data. We calculated a latitude-weighted RMSE as expressed in section 2.2.3.

This experiment yielded results similar to the ACC analysis; the figures generated are not shown. For the majority of the variables we observed a reduction in the RMSE, particularly for medium term forecasts. In the RMSE, however, it is more difficult to assess the relative impact of the filter among the different variables, since for each of the variables we have different units, while the ACC is non-dimensional.

6. Summary and conclusions

The focus of this work has been to advance forward ideas of sequential data assimilation and numerical weather forecasting. Theoretical analyses have been performed as well as implementation of techniques in models of diverse complexity. This work has dealt with the three following aspects:

Ensemble Transform Kalman-Bucy filters

In the first part, we analyzed two recently proposed ensemble formulations based on the Kalman-Bucy filter which use an ODE formulation in pseudotime. It has been shown that the ODEs involved in these formulations stiffen under certain conditions and cause the failure of the Euler forward integration used in these works. Namely, this occurs in the case of infrequent observations (long forecast windows) or for regions with sparse observational networks. As an alternative, a Diagonal Semi-Implicit integration method with variable step size was introduced; this method ensures stability and is computationally affordable.

Transform-based versions of BGR09 and BR10 were developed; we call them ensemble transform Kalman-Bucy filters. For these alternatives, the variables integrated in pseudo-time are weights, with dimension equal to the ensemble size rather than the much larger model dimension. The transform formulations have the additional advantage that the availability of the weights allows the application of methods such as QOL and RIP that improve the accuracy of ensemble Kalman filtering under nonlinear, non-Gaussian

perturbation growth (Kalnay and Yang, 2010, Yang and Kalnay, 2009a). Moreover, an R-localization scheme was designed to complement the ETKBFs. Adaptive multiplicative covariance inflation (Miyoshi 2011) is a very powerful tool that can be applied with R-localized assimilation schemes, so the ETKBFs can benefit from it too.

Three models were used to test our transform-based Kalman-Bucy filters and to illustrate the value of the Diagonal Semi-Implicit integration method. First, the highly nonlinear L63 model allowed us to perform experiments with frequent and infrequent observations. In the L96 model we applied the ETKBFs using R-localization and adaptive multiplicative covariance inflation. The advantages of using the DSI integration when initializing the background ensemble without prior information were demonstrated with an example. Finally, we implemented our schemes in an AGCM known as the SPEEDY model with a realistic radiosonde observational network. The equivalence in their performance with respect to the LETKF was shown, even for data sparse regions (e.g. over the oceans) in which the ODEs are bound to stiffen.

An essential implementation issue for the Bucy-type formulations is the choice of the number of steps for the integration. We have shown that in the 'frequent observations' case (corresponding to $\Delta t = 0.08$ in L63, $\Delta t = 0.05$ in L96, and $\Delta t = 6\,hr$ in an AGCM), an adequate performance starts at 3-6 steps. For infrequent observations ($\Delta t = 0.25$ in L63) this number doesn't surpass 8 (as a result of using the DSI method with non-uniform steps). For any dynamical system, it will be necessary to first estimate β) for the given assimilation window length. A possible improvement of the R-localization

implementation would to compute β locally and let every gridpoint use a different number of steps depending on the local degree of stiffness.

The computational implementation of the Bucy-type approaches and their transform versions are straightforward and amenable to parallel computing. Finally, the continuous formulation of the ensemble Kalman filter allows for a seamless implementation of the incremental analysis update (IAU, Bloom et al, 1996) as demonstrated in the mollified ensemble Kalman-Bucy filter (Bergemann and Reich, 2010a). The purpose of this implementation is to avoid the imbalance introduced by the jumps from background to analysis that are present in sequential data assimilation by spreading the observation over a larger portion of the forecast window as presented in figure. Now that we have shown that the EnKBF/ETKBF can be used in an atmospheric model, the next step in this line of research should be to implement the mollified EnKF in the SPEEDY model and look for reduction in balance disturbance.

Ensemble clustering in deterministic EnSRFs

In the second part of this work we have studied ensemble clustering (EC), a phenomenon that arises when performing data assimilation in nonlinear forecast models using deterministic EnSRFs. In this phenomenon, an *M*-member ensemble is split into an outlier and a tight cluster of *M-1* members. It results from the interaction of the nonlinear expansion of the ensemble spread in the forecast step and the linear contraction in the analysis step. We started by introducing a metric, clustering degree (CD), to quantify and follow the behavior of this phenomenon through time.

The main goal of this study was to dispel the notion that clustering is an irreversible phenomenon that severely handicaps EnSRFs. We have shown that generally it is a transient phenomenon and that the same nonlinear features of the forecast model that lead to it can also revert it. In particular, the variation on both the magnitude and 'direction' of nonlinear growth of perturbations for different regions of the phase space prevent clustering from becoming a permanent feature, and its persistence seems to diminish as the dimensionality of the model grows.

Unbiased rotated versions of (deterministic) EnSRFs (Sakov and Oke 2008; Livings et al, 2008) can be considered a middle point between the stochastic and deterministic alternatives, performing an effective resampling of the ensemble at every analysis step. This resampling removes any deformation in the background ensemble caused by nonlinear perturbation growth during the forecast window, and helps to maintain the statistical properties of the ensemble closer to Gaussian. Both unbiased randomly rotated EnSRFs and stochastic EnKFs avoid ensemble clustering, however only the former fulfill the KF covariance equation exactly.

We have compared the behavior of the LETKF and the MPNS-ETKF, a modification of the LETKF by an unbiased randomly rotated modification that we have introduced and which is rather simple to construct. Using the L63 and the SPEEDY models, we have assessed the performance of both filters in the following aspects: (a) the accuracy of the ensemble mean as best estimator of the truth in terms of background and analysis RMSE,

(b) the behavior of higher order moments of the ensemble, in particular sample skewness, and (c) the statistical reliability of the ensemble with respect to the truth as measured by rank histograms. In the linear regimes, the two filters have indistinguishable performances. It is in the nonlinear regimes, differences arise as expected; the remaining of the text refers to this case. We do not intend to assert that one filter is better than the other; as a matter of fact the conclusion would be different depending on the particular aspect we focus on.

In terms of RMSE, the results of experiments with the L63 show that differences are noticeable only when the ensemble size becomes much larger than the number of variables. The MPNS-ETKF has a lower mean RMSE because a smaller number of cycles with very large RMSE appear, but the general distribution of the RMSE is not very different from that of LETKF as shown by boxplots. For the SPEEDY model, the RMSE values obtained by the two methods are indistinguishable for all variables even in the poorly observed regions of the globe. LETKF tends to create ensembles with values different from the Gaussian in nonlinear regimes. For the SPEEDY model, we clearly observe this behavior for the variables $\{T, q\}$ in the tropics and the SH, where the sample skewness values are clearly different from zero. This, however, does not lead to higher RMSE values with respect to MPNS-ETKF.

When verifying the truth against the analysis ensemble in L63 when $M > N$, the rank histograms obtained from MPNS-ETKF tend to be flat, while those obtained from LETKF are not. The truth tends to be statistically indistinguishable from the MPNS-

ETKF-generated ensemble, while this assertion cannot be stated in the LETKF case. This is not the case when $M = N$, in this case we get over-dispersive ensembles for both filters. For SPEEDY, using $M << N$ with localization and adaptive multiplicative inflation the rank histograms obtained by both filters have the same behavior, viz. they show an under-dispersive ensemble. Nonetheless, a desirable feature of the LETKF is that it allows us to follow the evolution of individual ensemble trajectories through time, while for the MPNS-ETKF any information about individual trajectories is lost every time assimilation is performed due to the resampling on the ensemble.

Finally, we have emphasized that R-localization requires a locally symmetric analysis in every gridpoint. If one wishes to use random rotations these have to be performed only after the global analysis has been constructed. This signifies an extra step, but there may be applications in which it is worth it. We end this work echoing a conclusion from Lawson and Hansen 2004, namely, that the key to handle different filters is to understand their mechanisms, implications and limitations.

Effects of the RAW filter in the SPEEDY model

In this last part we have addressed two questions. The first question is: Are there any statistically significant changes in the monthly climatology of the SPEEDY model caused by the upgrade in the numerical integration scheme from Robert-Asselin (RA) filter to Robert-Asselin-Williams (RAW) filter? To answer this question, we performed a Satterthwaite-Welch t-test for the difference of means for each variable, in order to assess local significance at the 5% level. At some grid points the tests were passed, but these

points appeared to be scattered around the globe and showed no particular preference for location. In field significance tests, after considering the effects of both finite sample size and spatial correlation, we found that there is no significant evidence to reject the null hypothesis of identical climatologies. In other words, for each month, the climatology generated by integrating with the RA filter is the same as the one obtained with the RAW filter. Hence, the RAW filter is suitable for use in the SPEEDY model.

The second question asked is: Is there a statistically significant improvement in the skill of short to medium term (24-144 hour) forecasts caused by the upgrade from RA filter to RAW filter? To answer this question, an ACC analysis was performed for 24, 48, 72, 96, 120 and 144-hour forecasts for the month of January 1982. As analysis data we used the NCEP Reanalysis dataset interpolated onto the SPEEDY grid. The model climatology was generated by 8 year integrations of SPEEDY. The ACC analysis was performed on three pressure levels (835, 510 and 200 hPa), both globally and by latitude. A complementary RMSE analysis was performed following the same scheme, and yielding the same conclusions as the ACC analysis.

In general, an improvement of order $O(10^{-3})$ in the ACC can be attributed to the use of the RAW filter, and the improvement is larger for medium term forecasts with lead times of 72, 120 and 144 hours. The geopotential height was strongly benefited in the tropics, with ACC increases as large as 0.02 for a 72-hour forecast and 0.025 for a 120-hour forecast. As a consequence, five-day forecasts made using the RAW filter have approximately the same skill as four-day forecasts made using the RA filter, and four-day

forecasts made using the RAW filter have approximately the same skill as three-day forecasts made using the RA filter. The meridional wind was strongly benefited in the extra-tropics. The improvements in surface pressure mimicked those in geopotential height, and the impacts on temperature were very similar to those on meridional velocity. The improvements for the zonal velocity were less noticeable and there were no significant improvements in the relative humidity.

The results of this work are encouraging for the use of the RAW filter in the numerical solution of models based on the widely used RA filter. More generally, we have found that the skill of medium-range weather forecasts is sensitive to the time-stepping method, about as much as could be expected from the use of different physics parameterizations to improve forecast skill. We suggest that, in future work, numerical time schemes be revisited as a potentially important component of model error.

Appendix A. Derivation of the Kalman-Bucy filter and the equivalence of the KBF and KF equations in pseudo-time

The derivation of the KBF relies on discretizing a continuous-time system, applying the KF equations, and then letting $\Delta t \to 0$. The derivation in this appendix follows the steps outlined in Simon (2006). Consider the following ODE system describing the evolution of a continuous-time system $\mathbf{x}(t)$ and observations $\mathbf{y}(t)$ of this system:

$$\frac{d}{dt}\mathbf{x}(t) = \mathbf{F}(t)\mathbf{x}(t) + \mathbf{w}(t) \tag{A1}$$

$$\mathbf{y}(t) = \mathbf{H}(t)\mathbf{x}(t) + \mathbf{v}(t) \tag{A2}$$

where $\mathbf{w}(t) \sim N(\mathbf{0}, \mathbf{Q}_c)$ and $\mathbf{v}(t) \sim N(\mathbf{0}, \mathbf{R}_c)$ represent continuous-time white noise. If $\mathbf{F}(t) = \mathbf{F}$ is constant with respect to time, then the solution to this system is fairly simple:

$$\mathbf{x}(t) = \mathbf{x}(t_0)e^{(t-t_0)\mathbf{F}} + \int_{t_0}^{t} e^{(t-\tau)\mathbf{F}}\mathbf{w}(\tau)d\tau \tag{A3}$$

The expression $e^{\mathbf{F}t}$ is a matrix exponential. There are several ways to compute it, the simplest (yet not the most efficient) is to use the McLaurin series expansion:

$$e^{\mathbf{F}t} = \sum_{j=0}^{\infty} \frac{(\mathbf{F}t)^j}{j!} \tag{A4}$$

Discretizing the system

One can use the previous idea to discretize continuous-time systems over a "small" time step, denoted $\Delta t = t_k - t_{k-1}$. If Δt is sufficiently small, one can consider: $\mathbf{F}(t) \approx \mathbf{F}(t_{k-1})$ and $\mathbf{w}(t) \approx \mathbf{w}(t_{k-1})$ as constants through the time step. Then, the solution for $\mathbf{x}(t_k)$ becomes:

$$\mathbf{x}(t_k) = e^{\Delta t \mathbf{F}} \mathbf{x}(t_{k-1}) + \left[\int_0^{\Delta t} e^{(t_k - \tau)\mathbf{F}} d\tau \right] \mathbf{w}(t_{k-1}) \tag{A5}$$

Letting: $\alpha = \tau - t_{k-1}$, (A3) can be written as:

$$\mathbf{x}(t_k) = e^{\mathbf{F}\Delta t} \mathbf{x}(t_{k-1}) + e^{\mathbf{F}\Delta t} \left[\int_0^{\Delta t} e^{-\mathbf{F}\alpha} d\alpha \right] \mathbf{w}(t_{k-1}) \tag{A6}$$

The integral in the last expression can be solved explicitly (for any invertible $\mathbf{F}$) as:

$$\int_0^{\Delta t} e^{-\mathbf{F}\alpha} d\alpha = \left(\mathbf{I} - e^{-\mathbf{F}\Delta t} \right) \mathbf{F}^{-1}. \tag{A7}$$

This gives rise to the following explicit solution for $\mathbf{x}(t_k)$:

$$\mathbf{x}(t_k) = e^{\mathbf{F}\Delta t} \mathbf{x}(t_{k-1}) + \left(e^{\mathbf{F}\Delta t} - \mathbf{I} \right) \mathbf{F}^{-1} \mathbf{w}(t_{k-1}) \tag{A8}$$

We can identify this equation with the difference equation used in the KF:

$$\mathbf{x}_k = \mathbf{A}_{k-1} \mathbf{x}_{k-1} + \mathbf{\Lambda}_{k-1} \mathbf{w}_{k-1} \tag{A9}$$

with $\mathbf{A} = e^{\mathbf{F}\Delta t}$ and $\mathbf{\Lambda} = \left(e^{\mathbf{F}\Delta t} - \mathbf{I}\right)\mathbf{F}^{-1}$. If the time step Δt is sufficiently small, then the exponential matrix can be approximated with the first two terms of its McLaurin series expansion $e^{\mathbf{F}\Delta t} \approx \mathbf{I} + \mathbf{F}\Delta t$. This allows simplifying:

$$\mathbf{A} = \mathbf{I} + \mathbf{F}\Delta t \tag{A10}$$

$$\mathbf{\Lambda} = \mathbf{I}\Delta t \tag{A11}$$

The continuous-time Kalman gain

The discretized equivalent for the white noises behave $\mathbf{w}_k \sim N\left(\mathbf{0}, \mathbf{Q}_c \Delta t\right)$ and $v_k \sim N\left(\mathbf{0}, \mathbf{R}_c / \Delta t\right)$ (for a further explanation see Simon, 2006). With this in mind, one computes the Kalman gain:

$$\mathbf{K}_k = \mathbf{P}_k^b \mathbf{H}^{\mathbf{T}} \left(\mathbf{H}\mathbf{P}_k^b \mathbf{H}^{\mathbf{T}} + \frac{\mathbf{R}_c}{\Delta t} \right)^{-1} = \mathbf{P}_k^b \mathbf{H}^T \Delta t \left(\mathbf{H}\mathbf{P}_k^b \mathbf{H}^{\mathbf{T}} \Delta t + \mathbf{R}_c \right)^{-1} \tag{A12}$$

From this expression, one can learn two limits:

$$\lim_{\Delta t \to 0} \frac{\mathbf{K}_k}{\Delta t} = \mathbf{P}_k^b \mathbf{H}^T \mathbf{R}_c^{-1} \tag{A13}$$

$$\lim_{\Delta t \to 0} \mathbf{K}_k = \mathbf{0} \tag{A14}$$

The Ricatti equation for the covariance

One can use the KF equation for covariance to get:

$$\mathbf{P}_k^b = \left(\mathbf{I} + \mathbf{F}\Delta t\right)\mathbf{P}_{k-1}^a \left(\mathbf{I} + \mathbf{F}\Delta t\right)^T + \mathbf{Q}_c \Delta t = \left(\mathbf{P}_{k-1}^a + \Delta t \mathbf{F}\mathbf{P}_{k-1}^a\right)\left(\mathbf{I} + \mathbf{F}\Delta t\right)^T + \mathbf{Q}_c \Delta t$$

Expanding the product, the expression can be simplified to:

$$\mathbf{P}_k^b = \mathbf{P}_{k-1}^a + \Delta t\left(\mathbf{F}\mathbf{P}_{k-1}^a + \mathbf{P}_{k-1}^a\mathbf{F}^T + \mathbf{Q}_c\right) + \Delta t^2\mathbf{F}\mathbf{P}_{k-1}^a\mathbf{F}^T \tag{A15}$$

One can insert $\mathbf{P}_{k-1}^a = (\mathbf{I} - \mathbf{K}_{k-1}\mathbf{H})\mathbf{P}_{k-1}^b$ in the last equation to get:

$$\begin{aligned}\mathbf{P}_k^b = (\mathbf{I} - \mathbf{K}_{k-1}\mathbf{H})\mathbf{P}_{k-1}^b + \Delta\mathrm{t}\left(\mathbf{F}(\mathbf{I} - \mathbf{K}_{k-1}\mathbf{H})\mathbf{P}_{k-1}^b + (\mathbf{I} - \mathbf{K}_{k-1}\mathbf{H})\mathbf{P}_{k-1}^b\mathbf{F}^T + \mathbf{Q}_c\right) \\ + \Delta\mathrm{t}^2\mathbf{F}(\mathbf{I} - \mathbf{K}_{k-1}\mathbf{H})\mathbf{P}_{k-1}^b\mathbf{F}^T\end{aligned} \tag{A16}$$

Pass $\mathbf{P}_{k-1}^b$ to the left hand side and divide by Δt:

$$\begin{aligned}\frac{\mathbf{P}_k^b - \mathbf{P}_{k-1}^b}{\Delta t} = -\frac{\mathbf{K}_{k-1}}{\Delta t}\mathbf{H}\mathbf{P}_{k-1}^b + \mathbf{F}(\mathbf{I} - \mathbf{K}_{k-1}\mathbf{H})\mathbf{P}_{k-1}^b + (\mathbf{I} - \mathbf{K}_{k-1}\mathbf{H})\mathbf{P}_{k-1}^b\mathbf{F}^T \\ + \mathbf{Q}_c + \Delta t\mathbf{F}(\mathbf{I} - \mathbf{K}_{k-1}\mathbf{H})\mathbf{P}_{k-1}^b\mathbf{F}^T\end{aligned} \tag{A17}$$

Taking the limit $\Delta t \to 0$ of the last expression is equivalent to finding the time derivative of $\mathbf{P}$. We use the limits we had previously computed.

$$\begin{aligned}\lim_{\Delta t \to 0}\frac{\mathbf{P}_k^b - \mathbf{P}_{k-1}^b}{\Delta t} = -\underbrace{\frac{\mathbf{K}_{k-1}}{\Delta t}}_{\mathbf{P}\mathbf{H}^{\mathbf{T}}\mathbf{R}_c^{-1}}\mathbf{H}\mathbf{P}_{k-1}^b + \mathbf{F}\left(\mathbf{I} - \underbrace{\mathbf{K}_{k-1}}_{0}\mathbf{H}\right)\mathbf{P}_{k-1}^b \\ + \left(\mathbf{I} - \underbrace{\mathbf{K}_{k-1}}_{0}\mathbf{H}\right)\mathbf{P}_{k-1}^b\mathbf{F}^T + \mathbf{Q}_c + \underbrace{\Delta t}_{0}\mathbf{F}\left(\mathbf{I} - \underbrace{\mathbf{K}_{k-1}}_{0}\mathbf{H}\right)\mathbf{P}_{k-1}^b\mathbf{F}^T\end{aligned}$$

Which after simplifying reduces to the following:

$$\lim_{\Delta t \to 0}\frac{\mathbf{P}_k^b - \mathbf{P}_{k-1}^b}{\Delta t} = -\mathbf{P}_{k-1}^b\mathbf{H}^{\mathbf{T}}\mathbf{R}_c^{-1}\mathbf{H}\mathbf{P}_{k-1}^b + \mathbf{F}\mathbf{P}_{k-1}^b + \mathbf{P}_{k-1}^b\mathbf{F}^T + \mathbf{Q}_c \tag{A18}$$

We can now drop both the subindex denoting time and the superindex denoting background or analysis, since this equation describes both propagation and analysis steps. Hence, we get the ODE:

$$\boxed{\frac{d\mathbf{P}}{dt} = -\mathbf{P}\mathbf{H}^T\mathbf{R}_c^{-1}\mathbf{H}\mathbf{P} + \mathbf{F}\mathbf{P} + \mathbf{F}\mathbf{A}^T + \mathbf{Q}_c} \tag{A19}$$

The equation for the mean

The KF equations for the evolution $\hat{\mathbf{x}}_k^b = \mathbf{A}_{k-1}\hat{\mathbf{x}}_{k-1}^a$ and analysis $\hat{\mathbf{x}}_k^a = \hat{\mathbf{x}}_k^b - \mathbf{K}_k\left(\mathbf{H}\hat{\mathbf{x}}_k^b - \mathbf{y}_k\right)$ for the estimator of the mean can be combined to get:

$$\hat{\mathbf{x}}_k^a = \mathbf{A}_{k-1}\hat{\mathbf{x}}_{k-1}^a - \mathbf{K}_k\left(\mathbf{H}\mathbf{A}_{k-1}\hat{\mathbf{x}}_{k-1}^a - \mathbf{y}_k\right) \tag{A20}$$

Substituting the expressions we have for $\mathbf{A}_{k-1}$ and $\mathbf{K}_k$:

$$\hat{\mathbf{x}}_k^a = \left(\mathbf{I} + \mathbf{F}\Delta t\right)\hat{\mathbf{x}}_{k-1}^a - \mathbf{P}\mathbf{H}^{\mathbf{T}}\mathbf{R}_c^{-1}\Delta t\left(\mathbf{H}\left(\mathbf{I} + \mathbf{F}\Delta t\right)\hat{\mathbf{x}}_{k-1}^a - \mathbf{y}_k\right) \tag{A21}$$

If we pass $\hat{\mathbf{x}}_{k-1}^a$ to the left hand side and divide by Δt:

$$\frac{\hat{\mathbf{x}}_k^a - \hat{\mathbf{x}}_{k-1}^a}{\Delta t} = F\hat{\mathbf{x}}_{k-1}^a - \mathbf{P}\mathbf{H}^{\mathbf{T}}\mathbf{R}_c^{-1}\left(\mathbf{H}\left(\mathbf{I} + \mathbf{F}\Delta t\right)\hat{\mathbf{x}}_{k-1}^a - \mathbf{y}_k\right) \tag{A22}$$

Taking the limit $\Delta t \to 0$ of the last expression is equivalent to finding the time derivative of $\hat{\mathbf{x}}$.

$$\lim_{\Delta t \to 0}\frac{\hat{\mathbf{x}}_k^a - \hat{\mathbf{x}}_{k-1}^a}{\Delta t} = \mathbf{F}\hat{\mathbf{x}}_{k-1}^a - \mathbf{P}\mathbf{H}^{\mathbf{T}}\mathbf{R}_c^{-1}\left(\mathbf{H}\left(\mathbf{I} + \mathbf{F}\underbrace{\Delta t}_{0}\right)\hat{\mathbf{x}}_{k-1}^a - \mathbf{y}_k\right)$$

After simplifying one gets:

$$\lim_{\Delta t \to 0} \frac{\hat{\mathbf{x}}_k^a - \hat{\mathbf{x}}_{k-1}^a}{\Delta t} = \mathbf{F}\hat{\mathbf{x}}_{k-1}^a - \mathbf{P}\mathbf{H}^{\mathbf{T}}\mathbf{R}_c^{-1}\left(\mathbf{H}\hat{\mathbf{x}}_{k-1}^a - \mathbf{y}_k\right) \tag{A23}$$

Again, we can drop both the subindex denoting time and the superindex denoting background or analysis and write the following ODE.

$$\boxed{\frac{d\hat{\mathbf{x}}}{dt} = \mathbf{F}\hat{\mathbf{x}} - \mathbf{P}\mathbf{H}^{\mathbf{T}}\mathbf{R}_c^{-1}\left(\mathbf{H}\hat{\mathbf{x}} - \mathbf{y}\right)} \tag{A24}$$

Equivalence of the solution of the KBF in pseudotime and the KF equations

The Kalman-Bucy filter can be used to perform an instantaneous analysis step by using a pseudo-time $0 \le s \le 1$ formulation with the following equations:

$$\frac{d\mathbf{P}}{ds} = -\mathbf{P}\mathbf{H}^{\mathbf{T}}\mathbf{R}^{-1}\mathbf{H}\mathbf{P} \tag{A25}$$

$$\frac{d\hat{\mathbf{x}}}{ds} = -\mathbf{P}\mathbf{H}\mathbf{R}^{-1}\left(\mathbf{H}\hat{\mathbf{x}} - \mathbf{y}\right) \tag{A26}$$

Now we show that the Ricatti equation for covariance in pseudo-time can be integrated analytically and reduces to:

$$\mathbf{P}^a = \left(\mathbf{I} - \mathbf{P}^b\mathbf{H}^T\left(\mathbf{H}\mathbf{P}^b\mathbf{H}^T + \mathbf{R}\right)^{-1}\mathbf{H}^T\right)\mathbf{P}^b \tag{A27}$$

For the ease of notation, let us define $\mathbf{\Gamma} \equiv \mathbf{H}^{\mathbf{T}}\mathbf{R}^{-1}\mathbf{H}$ and denote the pseudo-time derivative with a dot over the variable. Then, use a factorization for the covariance matrix as:

$$\mathbf{P} = \mathbf{L}\mathbf{Y}^{-1}. \tag{A28}$$

The pseudo-time derivative of this expression is:

$$\dot{\mathbf{P}} = \dot{\mathbf{L}}\mathbf{Y}^{-1} + \mathbf{L}\left[\dot{\mathbf{Y}^{-1}}\right] = \dot{\mathbf{L}}\mathbf{Y}^{-1} - \mathbf{L}\mathbf{Y}^{-1}\dot{\mathbf{Y}}\mathbf{Y}^{-1} = \left[\dot{\mathbf{L}} - \mathbf{L}\mathbf{Y}^{-1}\dot{\mathbf{Y}}\right]\mathbf{Y}^{-1} \tag{A29}$$

Also, substitute the same factorization in the Ricatti equation:

$$\dot{\mathbf{P}} = -\mathbf{L}\mathbf{Y}^{-1}\boldsymbol{\Gamma}\mathbf{L}\mathbf{Y}^{-1} \tag{A30}$$

Equate the last two equations for $\dot{\mathbf{P}}$ and solve for $\dot{\mathbf{L}}$:

$$\dot{\mathbf{L}} - \mathbf{L}\mathbf{Y}^{-1}\dot{\mathbf{Y}} = -\mathbf{L}\mathbf{Y}^{-1}\boldsymbol{\Gamma}\mathbf{L}$$

$$\dot{\mathbf{L}} = -\mathbf{L}\mathbf{Y}^{-1}\boldsymbol{\Gamma}\mathbf{L} + \mathbf{L}\mathbf{Y}^{-1}\dot{\mathbf{Y}} = \mathbf{L}\mathbf{Y}^{-1}\left[-\boldsymbol{\Gamma}\mathbf{L} + \dot{\mathbf{Y}}\right] \tag{A31}$$

The last expression implies that, in order for our factorization to be valid, the following system of equations must be satisfied:

$$\begin{bmatrix} \dot{\mathbf{L}} \\ \dot{\mathbf{Y}} \end{bmatrix} = \mathbf{J}\begin{bmatrix} \mathbf{L} \\ \mathbf{Y} \end{bmatrix}, \text{ with } \mathbf{J} = \begin{bmatrix} \mathbf{0} & \mathbf{0} \\ \boldsymbol{\Gamma} & \mathbf{0} \end{bmatrix} \tag{A32}$$

This system has an analytical solution of the form:

$$\begin{bmatrix} \mathbf{L}(s_o + \Delta s) \\ \mathbf{Y}(s_o + \Delta s) \end{bmatrix} = e^{\mathbf{J}\Delta s}\begin{bmatrix} \mathbf{L}(s_0) \\ \mathbf{Y}(s_0) \end{bmatrix} \tag{A33}$$

$\mathbf{J}\Delta s = \begin{bmatrix} \mathbf{0} & \mathbf{0} \\ \mathbf{\Gamma}\Delta s & \mathbf{0} \end{bmatrix}$ and $e^{\mathbf{J}\Delta s}$ is a matrix exponential. Notice that $\mathbf{J}\Delta s$ is a 2-nilpotent matrix, i.e. $(\mathbf{J}\Delta s)^r = 0 \ \forall \ r \geq 2$. This fact helps the matrix exponential to be simple to compute.

$$e^{\mathbf{J}} = \sum_{i=0}^{\infty} \frac{(\mathbf{J}\Delta s)^i}{i!} = \sum_{i=0}^{1} \frac{(\mathbf{J}\Delta s)^i}{i!} = \begin{bmatrix} \mathbf{I} & \mathbf{0} \\ \mathbf{0} & \mathbf{I} \end{bmatrix} + \begin{bmatrix} \mathbf{0} & \mathbf{0} \\ \mathbf{\Gamma}\Delta s & \mathbf{0} \end{bmatrix} = \begin{bmatrix} \mathbf{I} & \mathbf{0} \\ \mathbf{\Gamma}\Delta s & \mathbf{I} \end{bmatrix} \tag{A34}$$

Substituting the matrix exponential into the solution and recalling that $\mathbf{L} = \mathbf{PY}$:

$$\begin{bmatrix} \mathbf{P}(s_o + \Delta s)\mathbf{Y}(s_o + \Delta s) \\ \mathbf{Y}(s_o + \Delta s) \end{bmatrix} = \begin{bmatrix} \mathbf{I} & 0 \\ \mathbf{\Gamma}\Delta s & \mathbf{I} \end{bmatrix} \begin{bmatrix} \mathbf{P}(s_0)\mathbf{Y}(s_0) \\ \mathbf{Y}(s_0) \end{bmatrix} \tag{A35}$$

Perform the matrix multiplication in the right hand side of this equation, and performing a straightforward substitution of the resulting equations leads to:

$$\mathbf{P}(s_o + \Delta s)[\mathbf{\Gamma}\mathbf{P}(s_0)\Delta s + \mathbf{I}] = \mathbf{P}(s_0)$$

Hence, we can get an explicit solution for $\mathbf{P}(s_o + \Delta s)$:

$$\mathbf{P}(s_o + \Delta s) = \mathbf{P}(s_0)\left(\mathbf{H}^{\mathbf{T}}\mathbf{R}^{-1}\mathbf{H}\mathbf{P}(s_0)\Delta s + \mathbf{I}\right)^{-1} \tag{A36}$$

For the analysis, we have $\mathbf{P}(s=1) = \mathbf{P}(s=0)\left(\mathbf{H}^{\mathbf{T}}\mathbf{R}^{-1}\mathbf{H}\mathbf{P}(s_0)\Delta s + \mathbf{I}\right)^{-1}$, or more clearly:

$$\mathbf{P}^{\mathbf{a}} = \mathbf{P}^{\mathbf{b}}\left(\mathbf{H}^{\mathbf{T}}\mathbf{R}^{-1}\mathbf{H}\mathbf{P}(s_0)\Delta s + \mathbf{I}\right)^{-1} \tag{A37}$$

One can use the Sherman-Morrison-Woodbury lemma to show the equivalence with (27).

Appendix B. Abbreviations and symbols

ACC: Anomaly correlation coefficient

AGCM: Atmospheric general circulation model

BGR09: Bergemann *et al.*, 2009.

BR10: Bergemann and Reich, 2010

DA: Data assimilation

DETKBF: Direct ensemble transform Kalman-Bucy filter

EC: Ensemble clustering

EnKBF: Ensemble Kalman-Bucy filter

EnKF: Ensemble Kalman filter (stochastic)

EnSRF Ensemble square root filter

ETKBF: Ensemble transform Kalman-Bucy filter

ETKF: Ensemble transform Kalman filter

KF: Kalman filter

L63: 3-variable Lorenz 1963 model

L96: 40-variable Lorenz 1996 model

LETKF: Local ensemble transform Kalman filter

MPNS-ETKF: Mean-preserving non-symmetric ensemble transform Kalman filter

NWP: Numerical weather prediction

ODE: Ordinary differential equation

RAW: Robert-Asselin-Williams filter

RMSE: Root mean squared error

SPEEDY: Simple parametrizations primitive equations dynamics model

$t, \Delta t$	Time, time step
$s, \Delta s$	Pseudotime, pseudotime step
$\mathbf{x} \in \Re^N$	Vector of state variables
$\mathbf{y} \in \Re^L$	Vector of observations
$\mathbf{H} \in \Re^{L \times N}$	Observation matrix
$\mathbf{R} \in \Re^{L \times L}$	Observational error covariance
$\mathbf{P} \in \Re^{N \times N}$	State error covariance
$\mathbf{K} \in \Re^{N \times L}$	Kalman gain matrix
$\overline{\overline{\mathbf{X}}} \in \Re^{N \times M}$	Ensemble of state variables
$\overline{\mathbf{x}} \in \Re^N$	Sample mean
$\mathbf{X} \in \Re^{N \times M}$	Ensemble of perturbations
u, v, T, q, z	Zonal wind, meridional wind, temperature, relative humidity, geopotential height
ps	Surface pressure

References

- Amezcua J., Ide K., Kalnay E. and Reich S., 2012. Ensemble transform Kalman-Bucy filters. *Q. J. R. Meteorol. Soc.*, submitted August 2011, revised January 2012.
- Amezcua J., Ide K., Bishop C. and Kalnay E., 2012a. Ensemble clustering in square root filters. *Tellus A*, submitted March 2012.
- Amezcua J., Kalnay E. and Williams P., 2011. Effects of the RAW filter in the climatology and forecast skill of the SPEEDY model. *Mon. Wea. Rev.*, **119**, 608-619.
- Anderson J., 2001. An ensemble adjustment filter for data assimilation. *Mon. Weather Rev.*, **129**, 2884–2903.
- Anderson J., 2010. A non-Gaussian ensemble filter update for data assimilation. *Mon. Wea. Rev.*, **138**, 4186-4198.
- Anderson J. and Anderson S., 1999. A Monte Carlo implementation of the nonlinear filtering problem to produce ensemble assimilations and forecasts. *Mon. Wea. Rev.*, **127**, 2741–2758.
- Asselin R., 1972. Frequency filter for time integrations. *Mon. Wea.Rev.*, **100**, 487–490.
- Bergemann K., Gottwald G. and Reich S., 2009. Ensemble propagation and continuous matrix factorization algorithms. *Q. J. R. Meteorol. Soc.*, **135**, 1560-1572.
- Bergemann K. and Reich S., 2010. A localization technique for ensemble Kalman filters. *Q. J. R. Meteorol. Soc.*, **136**, 701-707.
- Bergemann K. and Reich S., 2010a. A mollified ensemble Kalman filter. *Q. J. R. Meteorol. Soc.*, **136**, 1636-1643.

- Bishop C., Etherton B. and Majumdar S., 2001. Adaptive sampling with the ensemble transform Kalman filter. Part I: Theoretical aspects. *Mon. Wea. Rev.* **129**: 420–436.
- Bloom S., Takacs L., da Silva A. and Ledvina D., 1996. Data assimilation using incremental analysis updates. *Q. J. R. Meteorol. Soc.*, **124**, 1256–1271.
- Bourke W., 1974. A multilevel spectral model. I. Formulation and hemispheric integrations. *Mon Wea. Rev*, **102**, 687–701.
- Burgers G., van Leeuwen P. and Evensen G., 1998. Analysis scheme in the ensemble Kalman filter. *Mon. Wea. Rev.*, **126**, 1719-1724.
- Daley R., 1991. Atmospheric Data Analysis. *Cambridge University Press*, 457 pp.
- Déqué M. and D. Cariolle, 1986. Some destabilizing properties of the Asselin time filter. *Mon. Wea. Rev.*, **114**, 880–884.
- Desroziers G., Berre L., Chapnik B., and Poli P., 2005. Diagnosis of observation, background and analysis-error statistics in observation space. *Quart. J. Roy. Meteor. Soc.*, **131**, 3385–3396.
- Durran D., 1991. The third-order Adams-Bashforth method: an attractive alternative to leapfrog time differencing. *Mon. Wea. Rev.*, **119**, 702-720.
- Elmore K., Baldwin M. and Schultz D., 2006. Field Significance Revisited: Spatial Bias Errors in Forecasts as Applied to the Eta Model. *Mon. Wea. Rev*., **134**, 519-531.
- Evans E., Bhatti N., Kinney J., Pann L., Peña M., Yang S., Kalnay E. and Hansen J., 2004. RISE undergraduates find that regime changes in Lorenz's model are predictable. *Bull. Amer. Meteor. Soc.*, **85**, 520–524.

- Evensen G., 1994. Sequential data assimilation with a nonlinear quasigeostrophic model using Monte Carlo methods to forecast error statistics. *J. Geophys. Res.*, **99**, 10143–10162.
- Evensen G., 1997. Advanced data assimilation for strongly nonlinear dynamics. *Mon. Wea. Rev.*, **125**, 1342–1354.
- Evensen G., 2003. The ensemble Kalman filter: theoretical formulation and practical implementation. *Ocean Dyn.*, **53**, 343–367.
- Evensen G., 2006. Data assimilation: the ensemble Kalman filter. *Springler*, 280 pp.
- Gaspari G. and Cohn S., 1999. Construction of correlation functions in two and three dimensions. *Q. J. R. Meteorol. Soc.*, **125**, 723–757.
- Ghil M., 1989. Meteorological data assimilation for oceanographers. Part I: description and theoretical framework. *Dyn. Atmos. Oceans*, **13**, 171-218.
- Greybush S., Kalnay E., Miyoshi T., Ide K. and Hunt B., 2011. Balance and ensemble Kalman filter localization techniques. *Mon. Wea. Rev.*, **139**, 511-522.
- Hairer E. and Wanner G., 1996. Solving Ordinary Differential Equations II: Stiff and Differential-Algebraic Problems. *Springer Series in Comput. Mathematics*, Vol. 14, *Springer-Verlag*, second revised edition.
- Hamill T., Whitaker J. and Snyder C., 2001. Distance-dependent filtering of the background error covariance estimates in an ensemble Kalman filter. *Mon. Wea. Rev.*, **129,** 2776–2790.
- Horn R. and Johnson C., 1985. Matrix Analysis. *Cambridge University Press*, 561 pp.
- Houtekamer P. and Mitchell H., 1998. Data assimilation using an ensemble Kalman filter technique. *Mon. Wea. Rev.*, **126,** 796–811.

- Hunt B., Kostelich E. and Szunyogh I., 2007. Efficient data assimilation for spatiotemporal chaos: a local ensemble transform Kalman filter. *Physica D*, **230**, 112-126.
- Ide K., Courtier P., Ghil M. and Lorenc A., 1997. Unified notation for data assimilation: operational, sequential and variational. *J. Meteo. Soc. Japan*, **75**, 181-189.
- Ikeda K., 1979. Multiple-valued stationary state and its instability of the transmitted light by a ring cavity system. *Opt. Commun*, **30**, 257-261.
- Kalman R., 1960. A new approach to linear filtering and prediction problems. *Trans. of the ASME, Jour. of Bas. Engin. D*, **82**, 35-45.
- Kalman R. and Bucy R., 1961. New results in linear filtering and prediction problems. *Trans. of the ASME, Jour. of Bas. Engin. D*, **83**, 95-108.
- Kalnay E., 2003. Atmospheric modeling, data assimilation and predictability. *Cambridge University Press*. 364 pages.
- Kalnay E., Kanamitsu M., Kistler R., Collins W., Deaven D., Gandin L., Iredell M., Saha S., White G., Woollen J., Zhu Y., Leetmaa A., Reynolds R., Chelliah M., Ebisuzaki W., Higgins W., Janowiak J.,Mo K., Ropelewski C., Wang J., Jenne R. and Joseph D., 1996. The NCEP-NCAR 40-Year Reanalysis Project. *B. Am. Meteorol Soc.*, **77**, 437-471.
- Kalnay E., Li H., Miyoshi T., Yang S. and Ballabrera-Poy J., 2007. 4D-Var or ensemble Kalman filter? *Tellus*, **59A**, 758-773.
- Kalnay E. and Yang S., 2010. Accelerating the spin-up of ensemble Kalman filtering. *Q. J. R. Meteorol. Soc.*, **136B**, 1644–1651.

- Kantha L. and Clayson C., 2000. Numerical Models of Oceans and Oceanic Processes, International Geophysics Volume 66. *Academic Press*. 750 pp.
- Lawson W. and Hansen J., 2004. Implications of stochastic and deterministic filters as ensemble-based data assimilation methods in varying regimes of error growth. *Mon. Wea. Rev.*, **132**, 1966-1981.
- Leeuwenburgh O., Evensen G. and Bertino L., 2005. The impact of ensemble filter definition on the assimilation of temperature profiles in the tropical Pacific. *Q. J. R. Meteorol. Soc.*, **131**, 3291-3300.
- Li H., Kalnay E. and Miyoshi T., 2009, Simultaneous estimation of covariance inflation and observation errors within an ensemble Kalman filter. *Q. J. R. Meteorol. Soc.*, 135, 523–533.
- Livezey R. and Chen W., 1983. Statistical Field Significance and its Determination by Monte Carlo Techniques. *Mon. Wea. Rev*., **111**, 46-59.
- Liu J. and Kalnay E., 2008. Estimating observation impact without adjoint model in an ensemble Kalman filter. *Q. J. R. Meteorol. Soc.*, 134, 1327-1335.
- Livings D., Dance S. and Nichols N., 2008. Unbiased ensemble square root filters. *Phys. D*, **237**, 1021-1028.
- Lorenz E., 1963. Deterministic non-periodic flow. *J. Atmos. Sci.*, **20**, 130–141.
- Lorenz E., 1996. Predictability: a problem partly solved. In *Predictability. Proc 1995. ECMWF Seminar*, 1-18.
- Lorenz E. and Emanuel K., 1998. Optimal sites for supplementary weather observations: Simulations with a small model. *J. Atmos. Sci.*, **55**, 399–414.
- Lorenz E., 2005. Designing chaotic models. *J. Atmos. Sci.*, **62**, 1574–1587.

- Miller R., Ghil M. and Gauthiez F., 1994. Advanced data assimilation in strongly nonlinear dynamical systems. *J. Atmos. Sci.*, **51**, 1037-1056.
- Miyoshi, T., 2005. Ensemble Kalman filter experiments with a primitive-equation global model. Ph.D. thesis, University of Maryland, College Park, 226 pp.
- Molteni F., 2003. Atmospheric simulations using a GCM with simplified physical parametrizations. I: Model climatology and variability in multi-decadal experiments. *Climate Dyn.*, **20**, 175–191.
- Ott E., 2002. Chaos in dynamical systems. *Cambridge University Press*, 2nd edition. 492 pp.
- Ott E., Hunt B., Szunyogh I., Zimin A., Kostelich E., Corazza M., Kalnay E., Patil D. and Yorke J.,2004. A local ensemble Kalman filter for atmospheric data assimilation. *Tellus A*, **56**, 415-428.
- Pfeffer R., Navon I. and Zou X., 1992. A comparison of the impact of two time-differencing schemes on the NASA GLAS climate model. *Mon. Wea. Rev.*, **120**, 1381-1393.
- Reich S., 2011. A Gaussian mixture ensemble transform filter. *Q. J. R. Meteorol. Soc.* In press.
- Robert A., 1966. The integration of a low order spectral form of the primitive meteorological equations. *J. Meteor. Soc. Japan*, **44**, 237–245.
- Sakov P. and Oke P., 2008. A deterministic formulation of the ensemble Kalman filter: an alternative to ensemble square root filters. *Tellus A*, **60**, 361–371.
- Sakov P. and Oke P., 2008a. Implications of the form of the ensemble transformation in the ensemble square root filter. *Mon. Wea. Rev.*, **136**, 1042-1053.

- Simon D., 2006. Optimal State Estimation. *John Wiley & Sons*. New York. 552 pages.
- Spiller E., Budhiraja A., Ide K. and Jones C., 2008. Modified particle filter methods for assimilating Lagrangian data into a point-vortex model. *Phys. D*, **237**, 1498-1506.
- Tippett M., Anderson J., Bishop C., Hamill T. and Whitaker J., 2003. Ensemble square root filters. *Mon. Weather Rev.*, **131**, 1485–1490.
- Wilks D., 2005: Statistical Methods in the Atmospheric Sciences. *Academic Press*, 2nd Edition. 648 pages.
- Williams P., 2009. A Proposed Modification to the Robert-Asselin Time Filter. *Mon. Wea. Rev*., **137**, 2538-2546.
- Williams P., 2011. The RAW Filter: An Improvement to the Robert-Asselin filter in Semi-Implicit Integrations. *Monthly Weather Review*, **139**(6), pp 1996-2007.
- Yang S. and Kalnay E., 2009. Handling nonlinearity and non-Gaussianity in the ensemble Kalman filter: experiments with the three-variable Lorenz model. *Mon. Wea. Rev.,* submitted.
- Yang S., Kalnay E., Hunt B. and Bowler N., 2009a. Weight interpolation for efficient data assimilation with the local ensemble transform Kalman filter. *Q. J. R. Meteorol. Soc.*, **135**, 251-262.
- Toth Z. and Kalnay E., 1997. Ensemble forecasting at NCEP: The breeding method. *Mon. Wea. Rev.*, **125**, 3297–3318.
- Wang X., Bishop C. and Julier S., 2004. Which is better, and ensemble of positive-negative pairs or a centered spherical ensemble? *Mon. Wea. Rev.*, **132**, 1590-1605.

- Whitaker J. and Hamill T., 2002. Ensemble data assimilation without perturbed observations. *Mon. Weather Rev.*, **130**, 1913–1924.
- Williamson D., 1983. Description of NCAR Community Climate Model (CCMOB). *NCAR Technical Note*. NCAR/TN-210+STR. 88 pages.
- Williamson D. and Olson J., 2003. Dependence of aqua-planet simulations on time step. *Quart. J. of the Royal Met. Soc.*, **129**, 2049-2064.
- Yang S., Kalnay E., Hunt B. and Bowler N., 2009. Weight interpolation for efficient data assimilation with the local ensemble transform Kalman filter. *Q. J. R. Meteorol. Soc.*, **135**, 251-262.
- Yang S., Kalnay E. and Hunt B., 2012. Handling nonlinearity in Ensemble Kalman Filter: Experiments with the three-variable Lorenz model. *Mon. Wea. Rev.*, in press.
- Zhang Y., Ide K. and Kalnay E., 2012. *In preparation*.
- Zhao, B. and Q. Zhong, 2009: The dynamical and climate tests of an atmospheric general circulation model using the second-order Adams-Bashforth method. *Acta Meteorologica Sinica*, **23**, 738-749.